FEASIBILITY STUDY OF A METEOROID COMPOSITION ANALYZER SPECTROGRAPHIC SYSTEM

Final Report

Prepared by

AVCO CORPORATION
AVCO SPACE SYSTEMS DIVISION
RESEARCH AND TECHNOLOGY LABORATORIES
Wilmington, Massachusetts

AVSSD-0219-66-RR
Contract No. NAS-9-5267

3 November 1966

Prepared for

NASA MANNED SPACECRAFT CENTER
Houston, Texas

FEASIBILITY STUDY OF A METEOROID COMPOSITION ANALYZER SPECTROGRAPHIC SYSTEM
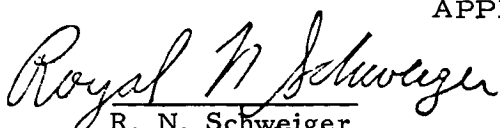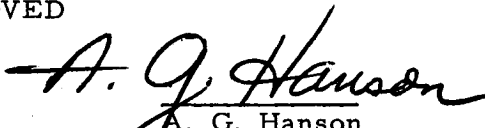
Final Report

Prepared by

AVCO CORPORATION
AVCO SPACE SYSTEMS DIVISION
RESEARCH AND TECHNOLOGY LABORATORIES
Wilmington, Massachusetts

AVSSD-0219-66-RR
Contract No. NAS-9-5267

3 November 1966

APPROVED

R. N. Schweiger
Project Manager

A. G. Hanson
Project Engineer

Prepared for

NASA MANNED SPACECRAFT CENTER
Houston, Texas

ABSTRACT

This report describes the results of the feasibility study performed on Contract NAS-9-5267. It is shown that spectrographic determination of the composition of micrometeoroids is feasible through analysis of emission spectra resulting from heating of the particle as it passes through a captive inert atmosphere. Spectra obtained from ablation of actual meteoritic materials during laboratory simulation experiments are shown.

Experimental studies were carried out in a ballistics range using a light gas gun to launch simulated and actual meteoritic particles into captive atmospheres of xenon and argon. A miniature spectrographic system was fabricated to provide maximum optical speed to obtain spectra from these ballistics range tests.

Feasibility of the above described concept was demonstrated by analysis of these spectral data. Analysis included comparison with other emission spectra obtained by carbon arc excitation of samples of the same meteorites. Correlation was excellent. Preliminary discussions of extensions of this concept to a spaceborne experiment are presented.

CONTENTS

ILLUSTRATIONS

SYMBOLS

F/No.   Optical speed or focal ratio of lens or lens system

θ Emergent angle from grating

d   Ruling separation of grating in Angstroms (A)

λ Wavelength of light in Angstroms

n   Spectral order

l   Linear dispersion at film plane

f   Focal length of lens

ϕ Acceptance angle of optical system or components

M   Magnification ratio

N   Refractive Index

ACKNOWLEDGMENT

1.0 INTRODUCTION

The composition of meteoroids has been previously studied[1] by spectrographic observation of meteor trails with ground-based instrumentation. Also, spectrographic and chemical analyses[2] have been made on meteorites which have survived the entry of the earth's atmosphere and have been recovered. Recently, several attempts have been made to recover meteoroid particles from space. These include sounding rocket tests[3,4] and an impacted panel carried on Agena 8 and recovered by Gemini 10 astronauts. The ground observation of meteor spectra is difficult because of the unpredictable time and location of atmospheric entry and because of the very larg distances between the event and the recording instrumentation. Radiation from particles in the micrometeoroid range is too faint to be recorded by earth based systems. The capture of meteoroids in a space environment requires that the kinetic energy of the particle be absorbed in the capturing material without destroying the particle. Also, present technology precludes the recovery of large areas or volumes of material from space so that the number of collected particles must necessarily be small or a very long exposure time is required.

The objective of the present program has been to establish the feasibility of a system which can be deployed in space to obtain data which can be used to deduce the composition of micrometeoroid particles without involving the necessity of recovering the experimental apparatus. The system utilizes the kinetic energy of the particles to cause the penetration of a thin wall balloon and the subsequent vaporization of the particle in a captive atmosphere inside the balloon. The interaction of the vaporized mass of the meteoroid with the captive atmosphere results in the excitation of the atomic species contained in the vapor and, subsequently, characteristic spectral radiation occurs which can be analyzed to determine the chemical composition. If the composition of the captive atmosphere is chosen properly, it will provide an environment for the ablative decomposition of the meteoroid particle and will not introduce additional background radiation signatures.

This feasibility study has been directed toward the following goals:

    a. The design, fabrication, and evaluation of a miniature laboratory breadboard spectrograph having as fast an optical speed as is consistent with spectral resolution of 10 A or better;

    b. The feasibility of containing the captive atmosphere and means of transmitting the optical radiation from the meteor trail to the spectrograph;

    c. The study of sensors required to record the spectra;

d. The demonstration, using a ballistics range, of the performance of the spectrograph in producing spectrographic signatures which can be used to determine the composition of meteoritic particles; and

e. A preliminary study of the adaptability of the experiment to a space meteoroid environment.

The following report describes the results of these studies and presents the data obtained from the ballistics range tests compared with analytical spectral analyses of artificial and actual meteoritic materials.

Finally, a conceptual design of a spaceborne experiment is presented together with the specifications and performance requirements of the major components of the system.

2.0 LABORATORY EXPERIMENTS

The problem of measuring the composition of meteoroids in the space environment involves the development of a system which is sensitive to micrometeoroids in the mass range of about 10^{-7} grams and greater. This results from the relatively high flux density of small particles compared with those meteoroids which produce meteor trails which are observable in the earth's atmosphere. The alternative to this high sensitivity is to provide a very large cross-sectional area of the detector which can be exposed for long periods of time.

The spectral analysis of the optical radiation produced in the flow field around and behind an entry body has received much attention during recent developments of ballistic missiles. Laboratory simulation of these reentry characteristics has been very difficult because of the chemical kinetics associated with the decomposition of ablation products in the presence of air. An important characteristic,then,of a captive atmosphere for determining the composition of meteoroids is that no chemical reaction should occur between the atmosphere and the products produced by the decomposition of the meteoroid particle. A second requirement of this atmosphere is that of producing a maximum interaction with the passage of the small particles in order that the kinetic energy of the meteoroid be used to decompose the surface and excite the molecular species in such a way that they will radiate to define the chemical composition. This requirement dictates a gas having high molecular weight. In order to minimize the gas radiation which will produce background interference on the spectral recording system, an inert gas with a high ionization potential is desired. Argon and xenon have been investigated in the laboratory experiments as part of this study. Finally, the captive atmosphere should produce the meteor signature in a relatively short trail with a minimum pressure or mass of gas. The feasibility of a spaceborne experiment then involves the study of several parameters which must be optimized for the expected meteoriod flux levels and optical radiation intensities to be observed.

In order to establish a reference level of optical radiation to be expected and to investigate the relative performance of the two inert gases chosen, a series of experiments was carried out in a ballistics range. A .22 caliber light gas gun of conventional design was used for these tests (see Figures la and lb). All particles were saboted. Sabots were either zelux or polyethylene of four-piece design. Velocities were measured by means of two Kerr cell-equipped shadowgraph stations immediately uprange of the test cell position.

A standard range section was employed as the test section (see Figure 2). This four-port unit was modified by turning down the ends to reduce its length to provide a trajectory length of about 20 cm and a gas volume of about 4 liters. Marmon clamps were then welded to each end to permit insertion of Mylar membranes to isolate the rest of the evacuated range system. One-mil Mylar was used uprange and 5-mil Mylar downrange to serve as a witness
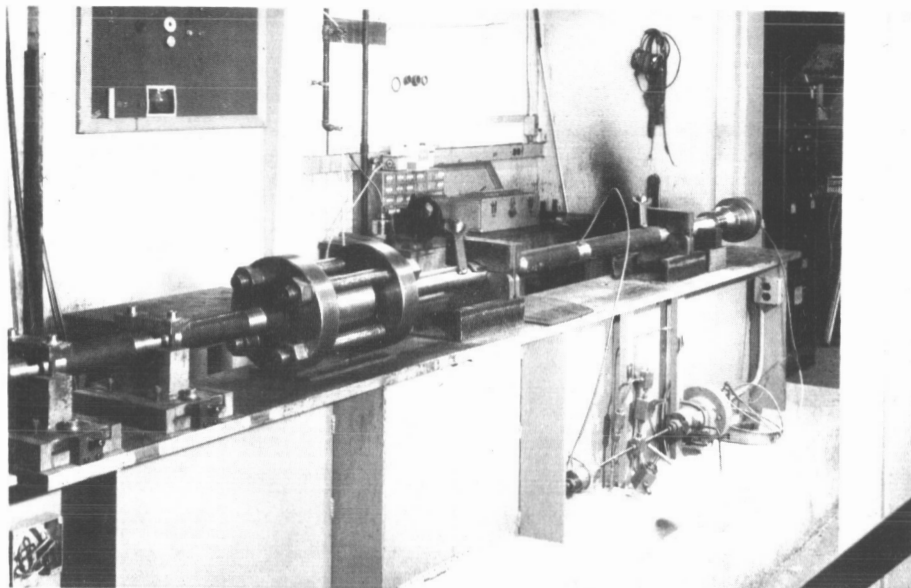
Figure 1a PHOTOGRAPH OF THE .22 CALIBER LIGHT GAS GUN
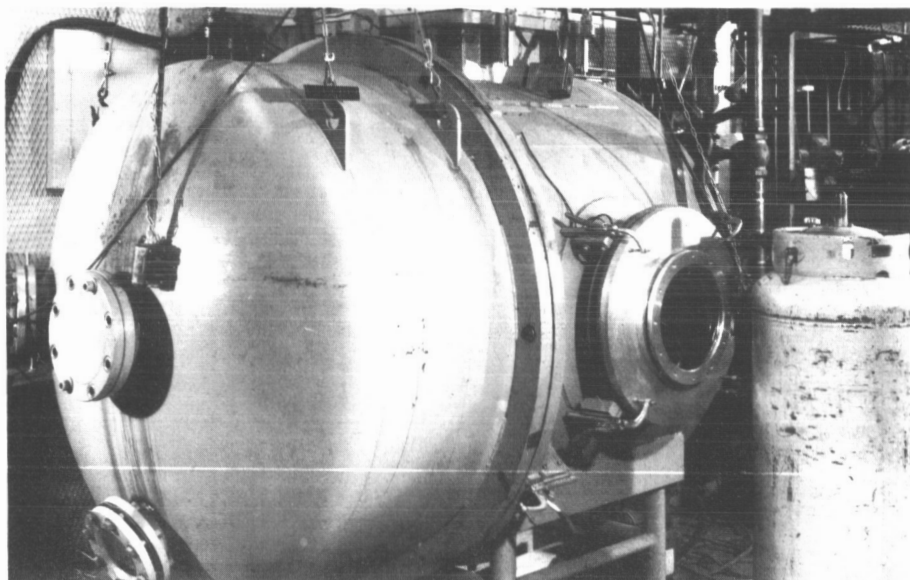
Figure 1b PHOTOGRAPH OF BALLISTICS VACUUM TANK USED TO ENCLOSE
BALLOON TEST CELL
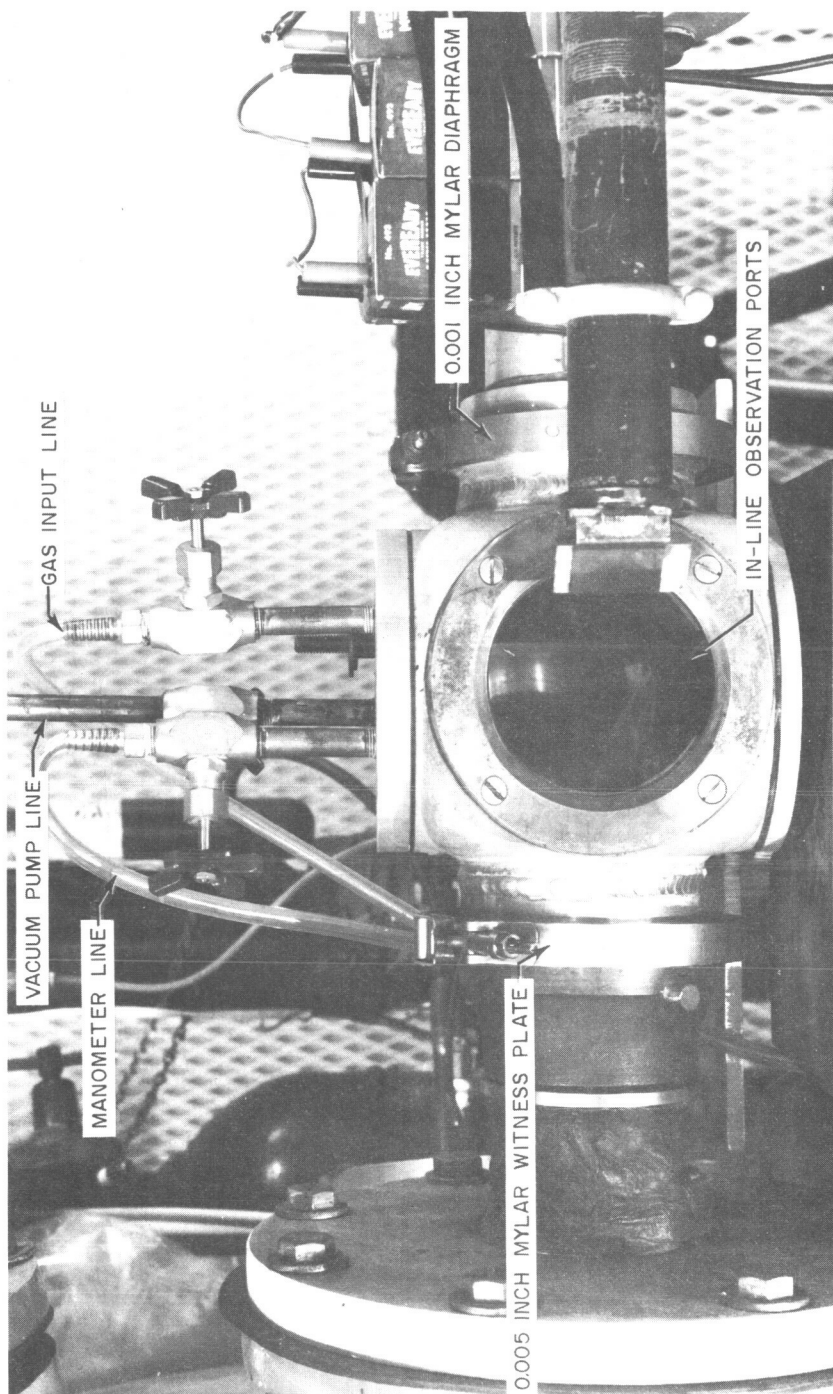
Figure 2 PHOTOGRAPH OF MODIFIED BALLISTICS RANGE TEST CELL

86-8234

-5-

plate. The top port was replaced by an aluminum plate provided with plumbing for a separate vacuum pump, argon and xenon bottles, and a mercury manometer. Side ports were used for spectrograph and monochromator recordings

A series of tests was designed to compare the measurements of particle radiation levels, resulting from spherical projectiles fired at velocities up to the maximum attainable with the gun, to the predictions of aerodynamic theory and to the results of other ballistic experimentation oriented toward the problems of vehicle reentry. Projectile velocity and test cell pressures were independently varied with other parameters held constant. All projectiles were 1/16-inch diameter Pyrex (borosilicate glass) spheres from a common lot.

Relative radiation amplitude was measured using an Ebert-Fastie type 0.25 meter Jarrell-Ash monochromator, monitoring a 14.5 A bandpass centered on 4226.7 A. The output of the monochromator was monitored by means of a photomultiplier type 931-A. This relatively narrow bandpass was chosen in order to avoid the several potential inaccuracies inherent in integration over a wide spectral range. Calcium is a conspicous radiator in the stony type meteoroids, and the 4226.7 A line is by far the most intense line (from neutral calcium) since it results from a high probability transition between one of the lowest (and hence appreciably populated) states and the ground state.

Three oscilloscope channels were used to record the monochromator's photomultiplier output, thereby increasing dynamic latitude and permitting maximum recording sensitivity in the case of deviation from the predicted velocity and particle flux. A tungsten standard lamp was employed to check against long-term drift of the photomultiplier characteristics. In addition, a mechanical jig was used to position a hollow cathode calcium calibration lamp at a fixed point within the test cell and along the projected optical axis of the monochromator.

The results of these monochromator measurements are shown in Figure 3. These results indicate that the radiation produced varies approximately as the 1.6th power of the pressure and on the order of the 10th power of the velocity. Simple aerodynamic theory would indicate that the radiation would be proportional to the 4th power of temperature and the temperature is proportional to the energy input or proportional to velocity squared. Therefore, the radiation should be proportional to the 8th power of velocity. Related experimental results at Avco[5] and CARDE[6] show a variation between 8th and 12th power dependence.

The data spread is disappointing but is less than that predicted by several experimental aerodynamicists for this number of experiments. Other than the latitude of experimental error, the following variables are expected to cause major variations of luminous output from both simulated and actual micrometeoroids:
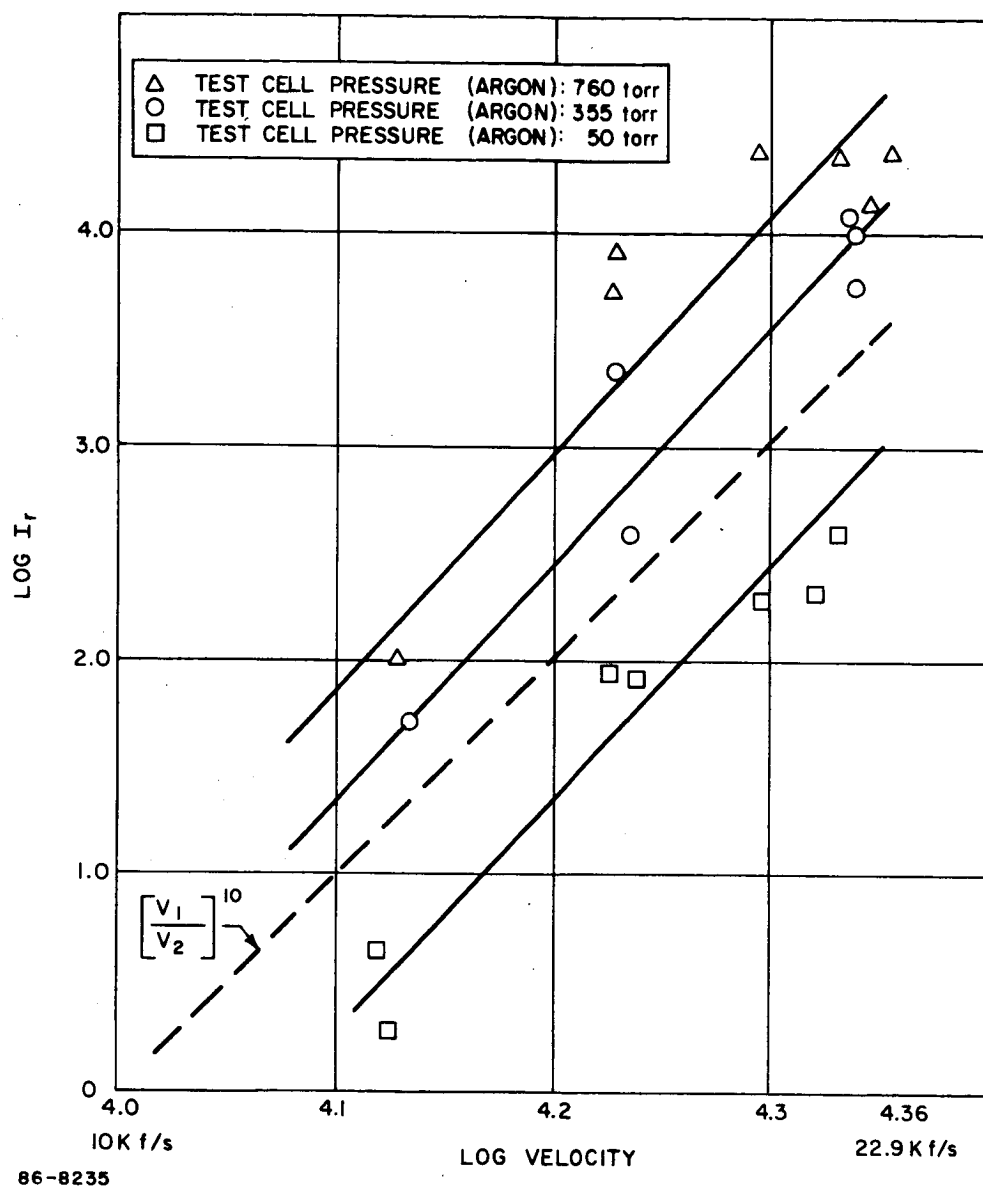
Figure 3 PLOT OF PROJECTILE RADIATION LEVEL AS A FUNCTION OF VELOCITY AND TEST CELL PRESSURE

a.   Tumbling: Assuming an aerodynamically unstable particle and a fixed viewing aspect, the recorded brightness level will fluctuate with particle attitude and the resultant stagnation point orientation to the collection optical axis.

b.   Ablation: Any particle which ablates rather than sublimes exhibits a cyclic rather than steady-state radiation as surface temperature varies with sloughing off of molten material and consequent exposure of cooler area.

c.   Particle Disintegration During or Prior to Time of Recording: This is a first-order variable in measurement of radiation amplitude. Since total radiation level is highly sensitive to both velocity and exposed surface area, the precise particle trajectory position (relative to the observation field) is highly critical in the case of in-flight fragmentation. If fragmentation takes place early enough to allow appreciable deceleration before entering the optical field, a considerable decrease from predicted luminosity will occur. Conversely, if fragmentation occurs at a position allowing temperature rise to take place within the optical field and before effective deceleration, an increase in total flux may be expected.

The results of these experiments indicate no major disagreement with predicted relationships. Acquisition of a much larger number of data points would undoubtedly permit a better curve fit. The data spread, however, appears to be inherent in such experimental measurements. It is therefore expected that similar variations in flux levels will occur in tests involving the breadboard instrumentation system and that an equal number of these experiments would be required in order to obtain a better curve fit. Such a large test series is beyond the scope of this program and is furthermore not necessary since precise quantitative flux amplitude measurement is not a requirement of this concept. Further discussion of the results of these tests is included in the section of this report dealing with experimental results.

Figure 22 of Section 7.0 is a photograph showing the ablation of a 1/16-inch spherical Pyrex projectile during one of the monochromator tests. The field of view is approximately 5 inches. The particle has already fragmented during penetration of the 1-mil Mylar which is just out of the optical field and represents the apex of the radiant cone. The particle velocity was 22,900 ft/sec; the range test section was pressurized with argon to 1 atmosphere. The camera was filtered to the same bandpass as the monochromator. An open shutter technique was employed. Similar photographs of tests involving different gases, pressures, and velocities showed variation of the fragmentation cone angle and apparent particle size as estimated by streak diameter. Correlation of these results with the varied test parameters was inconclusive.

3.0 SPECTROGRAPH DEVELOPMENT

3.1 OPTICAL DESIGN APPROACH

The experimental data obtained with the monochromator in the measurements described above indicated that a major requirement on the meteoroid analyzer is the development of a suitable miniature spectrograph whose design is capable of extension to a flight experiment. Proof of the high radiation dependence upon velocity makes clear the requirement for a fast, efficient optical system in order to extend the threshold limit of weak signal reception. Such an optical system must be compatible with the minimum dispersion required for data analysis. It is to be borne in mind that this design is for a laboratory breadboard instrument system. Design constraints of flight hardware are considered throughout, however. The following goals were set for design of the spectrograph:

a. Minimum size and weight;

b. High optical speed and efficiency;

c. Spectral dispersion and resolution resultant in a display of the first-order visible spectrum in a minimum sensor area and yet provide a resolution of approximately 10 A;

d. Limitation of optical aberrations by optimum design;

e. No order overlap;

f. Use of either silver halide film or electronic sensor;

g. Use of a fiber optics input slit; and

h. Optimum off-axis optical performance when using a wide (or matrix type) input slit.

To make this experiment feasible for space application, the spectrograph must employ an optical system of both small size and high total efficiency. In addition, it must use a sensor format also of minimal size (especially in the case of photographic film, in order to avoid long, weighty supply rolls) and yield a spectral record with adequate dispersion, resolution and overall image quality to satisfy analytical requirements of the experiment. Reduction in size of the optical system inherently means reduction of the optical path length and consequently of the "lever arm" available for dispersion. Regardless of the grating mounting or optical system used, this inevitably means the use of the shortest focal length optical components compatible with desired dispersion

and resolution. Unfortunately, optical performance of all classical spectrographic optical systems is degraded by both decrease of focal length and by increase of relative aperture, especially beyond F/4.

An effort was made to analytically determine the lower dispersion and resolution limits which would yield data of a quality high enough to provide usable "finger prints" of meteoroidal composition. This included analysis of both standard wavelength tables and of plates recorded from vaporization of meteoritic samples in a 3.4-meter laboratory spectrograph. The goal was to determine a minimum usable resolution. Final estimates from several spectroscopists and physicists ranged from an ideal resolution of 5 A to a marginal 30 A. It was decided that a more precise determination could be made only by empirical testing of a prototype instrument.

A review of classical grating mountings[7] revealed that only the symmetrical Ebert-Fastie system showed any promise of adaptation to a both fast and short focal-length system. Investigation, however, indicated that aberrations, especially astigmatism, drastically degrade line imaging when used with mirrors of aperture exceeding F/4. This was confirmed by Dr. William Fastie* of John Hopkins University, rediscoverer of the Ebert mounting, who also volunteered that the increased theoretical optical efficiency of a very wide aperture Ebert-Fastie instrument would never be realized in a film spectrograph due to excessive image scattering created by astigmatism.

When informed of the basic requirement of this task, Dr. Fastie suggested the consideration of a design employing commercially available camera lenses rather than conventional reflective optics. He referenced a recent investigation of this approach by Dr. Arnold Bass of the National Bureau of Standards and suggested consultation with him. Conversation with Dr. Bass** revealed that, in collaboration with Dr. Karl Kessler of N.B.S., he had designed and constructed a small, high aperture spectrograph for use in recording very weak light sources.[8] Dr. Bass discussed the design and forwarded a copy of his descriptive paper plus a Grumman report[9] detailing fabrication of an instrument employing this Bass-Kessler design. (The Grumman report primarily consists of detailed fabrication prints and was not utilized due to the mechanical changes resulting from employing a transmission rather than reflection grating, as described later in this section.) The Bass-Kessler concept takes advantage of the wide selection of wide-aperture lenses commercially developed over the past several years for use on 35-mm cameras. (For the further instrument miniaturization described in the following sections of this report, it is to be noted that a similar variety of even faster lenses has been developed in shorter focal lengths to cover the smaller formats of 16-mm cameras, vidicons, and image orthicons.) The best of such lenses are quite highly corrected, available as shelf hardware in a wide variety of focal lengths and F/Numbers, and are reasonable in price due to modern mass-production efficiency.

*Private Communication
**Private Communication 2/1/66 and 2/3/66.

Dr. Bass' design was thoroughly analyzed in terms of application to this experiment, and it was concluded that it would fulfill all of the basic requirements of the breadboard spectrograph. Use of the transmission grating results in a totally different mechanical configuration, but the resultant instrument does represent a modification of the basic Bass-Kessler design.

Dr. Gordan Milne of the Institute of Optics, University of Rochester and optical designer for Tropel, Inc., was employed as consultant on optical design for this system. Dr. Milne was called upon at this time to evaluate the approach and make recommendations prior to component purchase and fabrication. He concurred with use of the Bass-Kessler design and suggested the use of the transmission grating rather than the more commonly used reflection type in order to increase collection efficiency of the objective lens. In the reflection system, the objective or camera lens must be mounted far enough away from the grating surface to avoid mechanical interference with the incident collimated beam. This results in peripheral light loss in collection of the dispersed beam, notably at the extreme wavelengths. Use of a transmission grating avoids this difficulty, since the objective lens can be placed in virtual contact with the grating surface in order to collect divergent rays.

The spectrograph was subsequently constructed using this approach. The instrument employs a transmission grating in conjunction with a 300-mm F/4 collimator lens, a 75-mm F/1.5 objective lens, and a conventional single-lens reflex 35-mm camera. The resultant configuration is schematically shown below and is illustrated in the photographs of Figures 4 and 5.

BALLOON
TEST
CELL

FIBER
OPTICS
RELAY
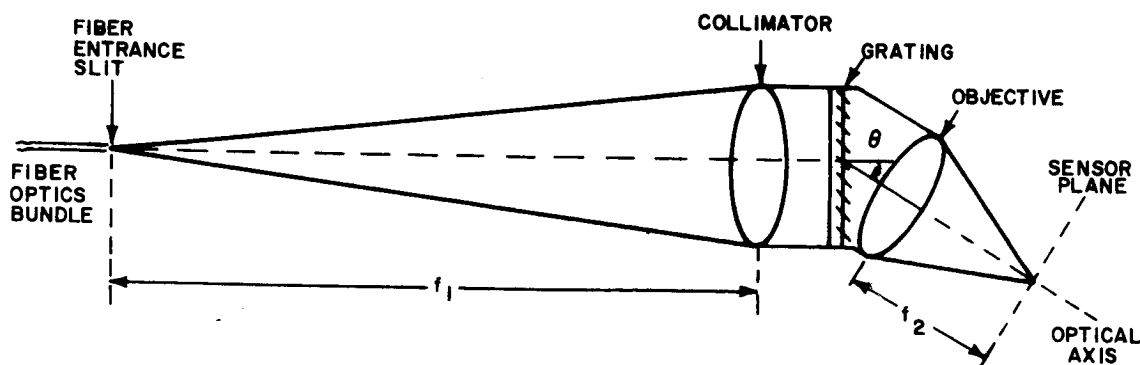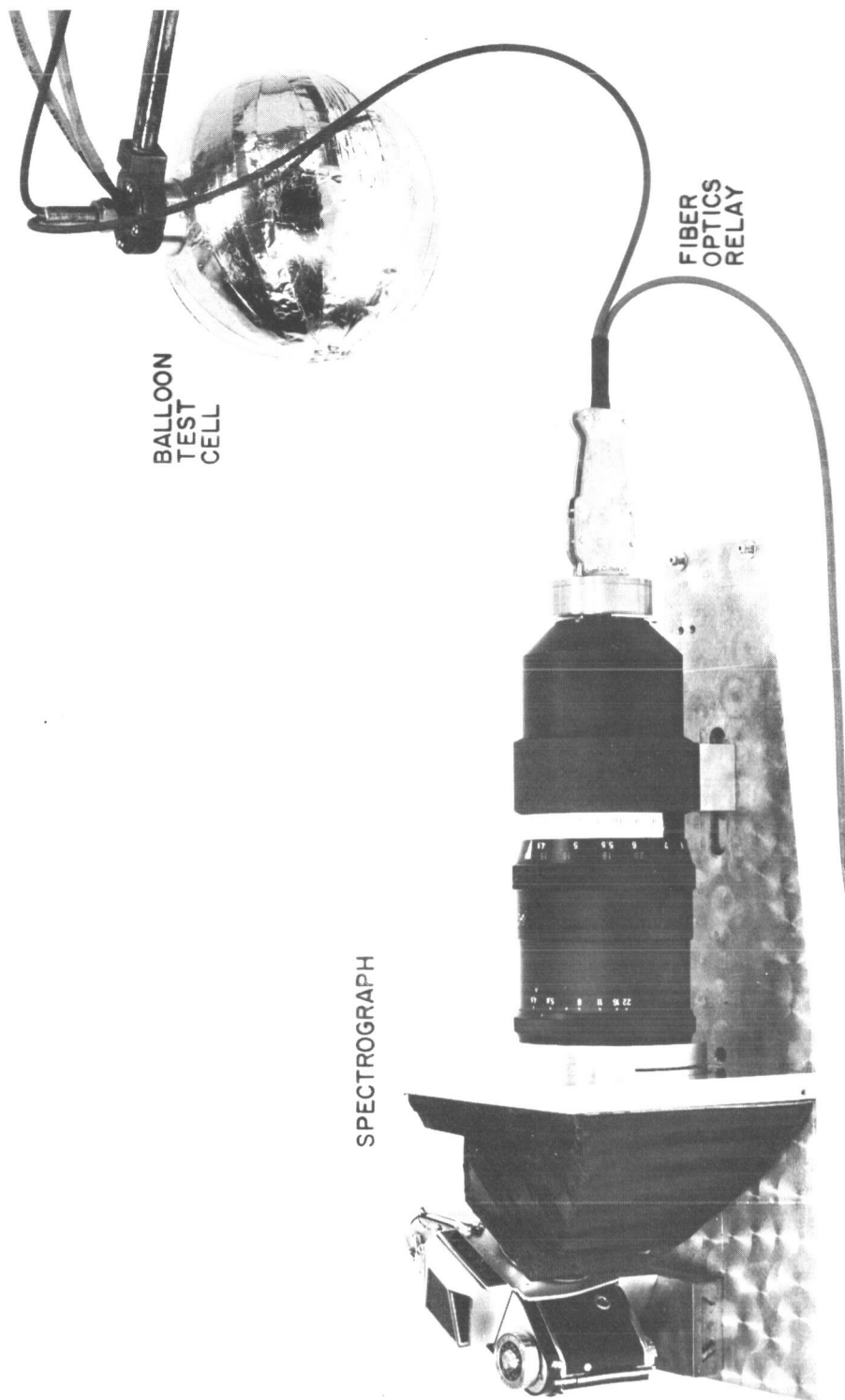
SPECTROGRAPH

86-8236

Figure 4 PHOTOGRAPH OF BREADBOARD SPECTROGRAPH SYSTEM

BALLOON TEST CELL

FIBER OPTICS ENTRANCE SLIT HOLDER

FOCUS ADJUSTMENT

OBJECTIVE LENS

GRATING MOUNTING AND COLLIMATOR LENS HOLDER

COLLIMATOR LENS

CAMERA

GRATING ROTATIONAL ADJUSTMENT

CAL. LAMP INPUT
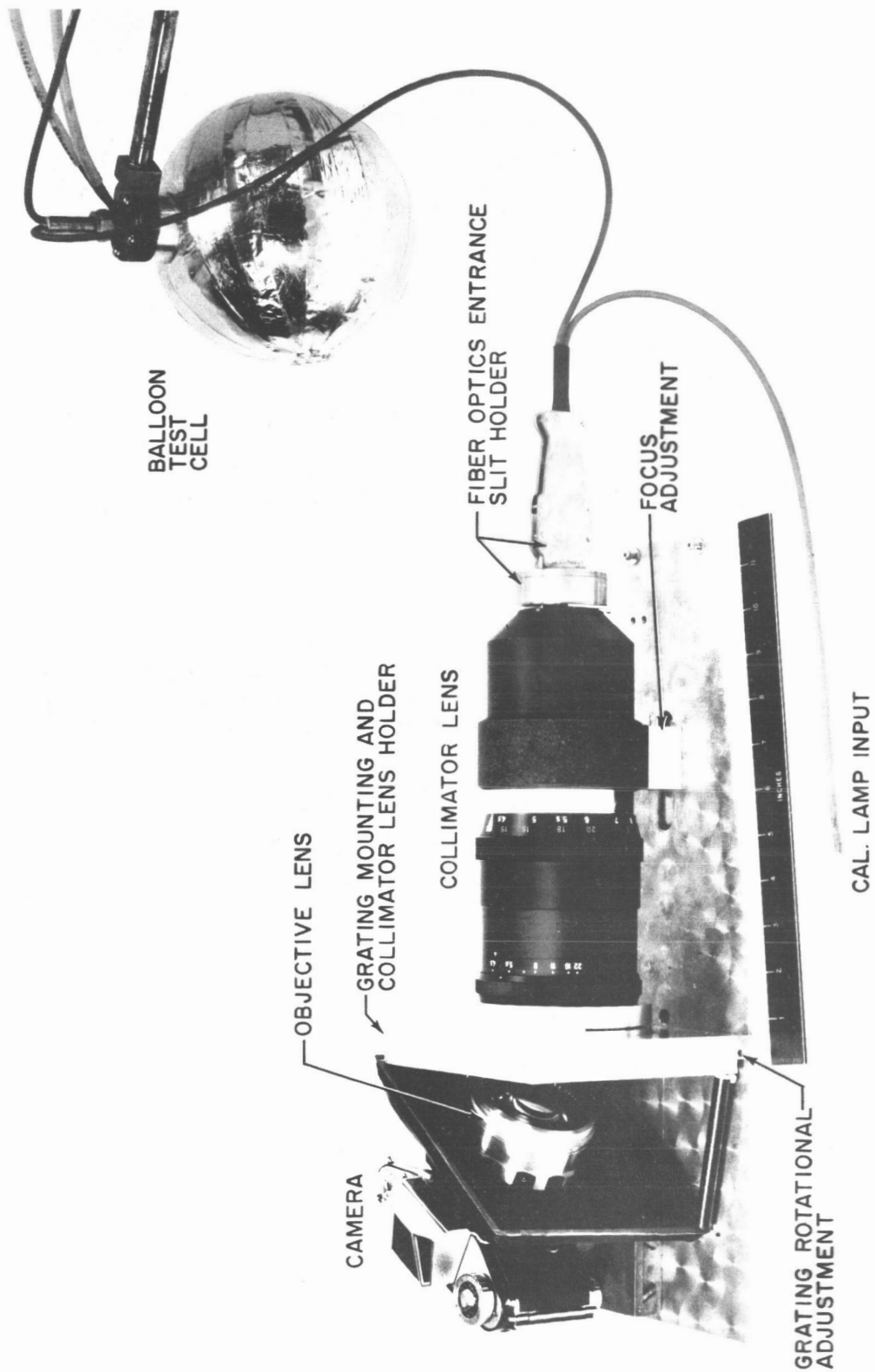
86-8237

Figure 5 PHOTOGRAPH OF BREADBOARD SPECTROGRAPH WITH COMPONENT IDENTIFICATION

-13-

This breadboard instrument is of a reasonably small size when compared to commercially available spectrographs. Both choice of components and fabrication of hardware were influenced by the intended function as a laboratory feasibility instrument. As discussed later, the design is capable of being scaled down to the miniaturization levels desirable for the flight experiment.

The following discussion treats functions of the individual components and the overall system performance in terms of this experiment's requirements.

3.2   FILM FORMAT

The 35-mm format (24 x 36 mm) is large enough to display either first- or second-order spectra. The film is commercially available in all spectrographic emulsions and required no adaptation of the camera transport mechanism. Neither this large frame size nor the complexity of the camera will be required for flight hardware even with the present optics.

3.3   OPTICS AND DISPERSION

A 75-mm focal length, F/1.5 chromatically corrected lens is used for the objective or camera lens. A Bausch and Lomb 600-line/mm transmission replica grating was chosen of size adequate to overfill the objective lens. The emergent angle θ at the blaze wavelength of 5461 A is 14 degrees 22 minutes for this grating.

The resultant angular dispersion[10] is given by: $\dfrac{d\theta}{d\lambda} = \dfrac{n}{d \cos \theta}$

where:

    d = ruling separation in A

    λ = blaze wavelength in A

    n = spectral order

and θ = emergent angle from grating at λ; substituting for the values above,

$$\frac{d\theta}{d\lambda} = \frac{1}{1.66 \times 10^4 \, (0.8773)}$$

$$= 6.87 \times 10^{-5} \ \text{rad/A}$$

and the linear dispersion at the film plane in the first order is given by:

$$\frac{dl}{d\lambda} = \frac{d\theta}{d\lambda} \ (f_1)$$

-14-

where

f_1 = focal length of objective lens.

then $\dfrac{dl}{d\lambda}$ = 6. 87 x 10^{-5} (75)

$\phantom{then \dfrac{dl}{d\lambda}}$ = 5. 15 x 10^{-3} mm/A

or, stated as the more commonly used reciprocal,

$\dfrac{d\lambda}{dl}$ = 194.08 A/mm

This compares with the actual measured dispersion of the completed instrument of 207. 7A/mm at the blaze wavelength of 5461A. The discrepancy is primarily due to a slight variation in focal length of the objective form the nominal 75 mm.

This dispersion results in first-order display of the entire 4000-7000 A bandpass in 15.5 mm or the second order in 31 mm. For testing purposes, mechanical alignment permitted the recording of the entire first order and half of the second-order dispersion proved to be adequate, and the second order record was an excellent comparison in data reduction. It will also be noted that, at the maximum aperture of F/1. 5, test data lack the same degree of overall sharpness shown by those exposed with the objective at F/4, and also that at F/1. 5 the shorter wave length line images are somewhat degraded in the first order but not in the second. This is due to some residual chromatic aberration in the objective, resulting, at maximum aperture, in poorer imaging, and in a focus of the first order violet and blue wavelengths approximately 0. 9 mm behind the flat film plane. The former is a tradeoff against speed in this lens, but the latter can be corrected by the use of a curved film plane contoured to match the focal curvature. In the present instrument, a compromise was reached by tilting the objective and film plane until the optimum focus was obtained in the long wave length first order and short wave length region of the second order. It is to be noted that at F/4, due to increased depth of focus, the condition is appreciably bettered. A comparison of the system resolution at F/1. 5 and at F/4 is illustrated in Figure 15 in Section 7. 0.

The input portion of the instrument consists of a 300 mm, F/4 telephoto collimator lens with a fiber optics slit positioned at its rear focal plane. Mechanical adjustments are provided for focusing of the slit, for grating rotation, and for camera and objective positioning.

3.4 SYSTEM EFFICIENCY AND RESOLUTION

Having chosen a first-order dispersion of approximately 200 A/mm, the prime design problem is that of achieving the most efficient optical system to yield acceptable final resolution at this low dispersion. Perhaps the most important

fact to bear in mind in these considerations is that the prime sensor under consideration is photographic film. Time integrated unit area flux (or power density) at the film plane is the only meaningful measure of efficiency, and any criteria of total flux collection or imaging is deceptive unless it can be related to unit area film exposure. This is also true of the vidicon considered as an alternate sensor for the same optical system.

Discussion of overall efficiency begins with the film, which here will be considered as a constant. In all laboratory experiments, the highest speed Kodak spectroscopic emulsion, type I-F (see Figure 6) was used. In a flight experiment, the choice of film will be dictated by mission requirements which influence the relative merits of tradeoffs of sensor sensitivity, resolution, dynamic latitude and susceptibility to environmental hazards such as thermal and hard radiation backgrounds. The grating-objective lens combination consists of the most efficient commercially available components which will jointly yield the desired dispersion. The replica grating was produced from a master selected by the late Dr. David Richardson of Bausch and Lomb for maximum transmission efficiency in the visible (61 percent at 5461 A). At an appreciable increase in costs and perhaps in experimental development at this time, the same dispersion and an improved efficiency may be achieved with considerable reduction in volume and weight. Such an approach would employ a transmission grating of 1200 rather than 600 lines/mm and an objective of one-half the focal length, or optical leverage. Such shorter focal length lenses are readily available in faster speeds than the F/1.5 used here. The disadvantage and added cost lie in the required grating manufacture. The practical limit in ruling of transmission gratings is 600 lines/mm; 900-line rulings have been produced, but with considerable loss in transmission efficiency due to internal reflection within the blank. At 1200 line/mm, the internal reflection becomes total. Dr. Richardson's solution to this problem was to produce 600 line rulings on both sides of an optical flat, thereby effectively doubling the dispersion. Bausch and Lomb produced one such grating, but the transmission efficiency was quite poor, again due to internal reflection.

Dr. Richardson then tried another approach, and applied 600-line/mm rulings to both sides of a prism whose angle matches that of the dispersion by the first grating surface. This first prototype "grism" was made for consideration by Avco for use in another NASA program. Evaluation of its performance is not complete, but initial reports from Bausch and Lomb are quite encouraging.

The collimator lens completes the internal optics of the instrument. The lens diameter must be large enough to permit the emergent collimated bundle to fill the grating, or, more precisely, to fill the projected area of the objective lens. This fixes the minimum lens diameter; focal length requirements must be determined by considering tradeoffs involved in incident collection angle and slit to slit-image magnification ratio, since this ratio affects resolution, particularly in such a system of such low dispersion. Let us examine the parameters involved.

-16-
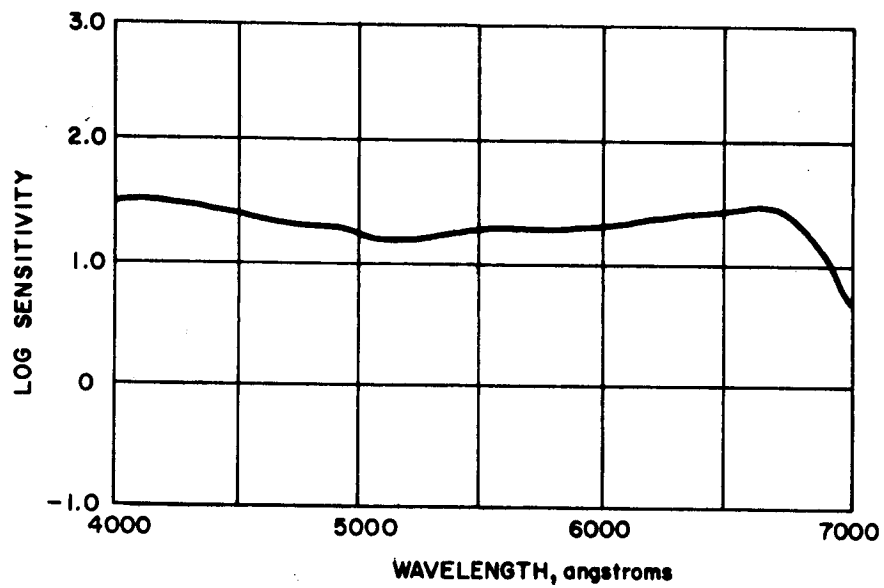
86-8238

Figure 6 SENSITIVITY OF KODAK CLASS I-F FILM AS A FUNCTION OF WAVELENGTH

The input slit is formed by a fiber optics bundle whose exit cone angle is identical to its large input acceptance angle (70 degrees in the breadboard case). In order to utilize this wide angle, it is necessary for the acceptance angle of the collimator lens to match that of the fiber bundle. This is desirable in order to "see" a maximum area within the balloon test cell. It will be shown, however, that this can be achieved by other means if necessary and that this maximum collection angle is not of first order importance to optical collection efficiency when using fiber optics, and that in the simulation case it is of vitually no concern.

First, take the symmetrical case where the included acceptance angle ϕ of the fibers and that, ϕ' of the collimator, C, are matched, and where the focal length of f_1 is identical to that of the objective lens, f_2, as shown in the following sketch (a):
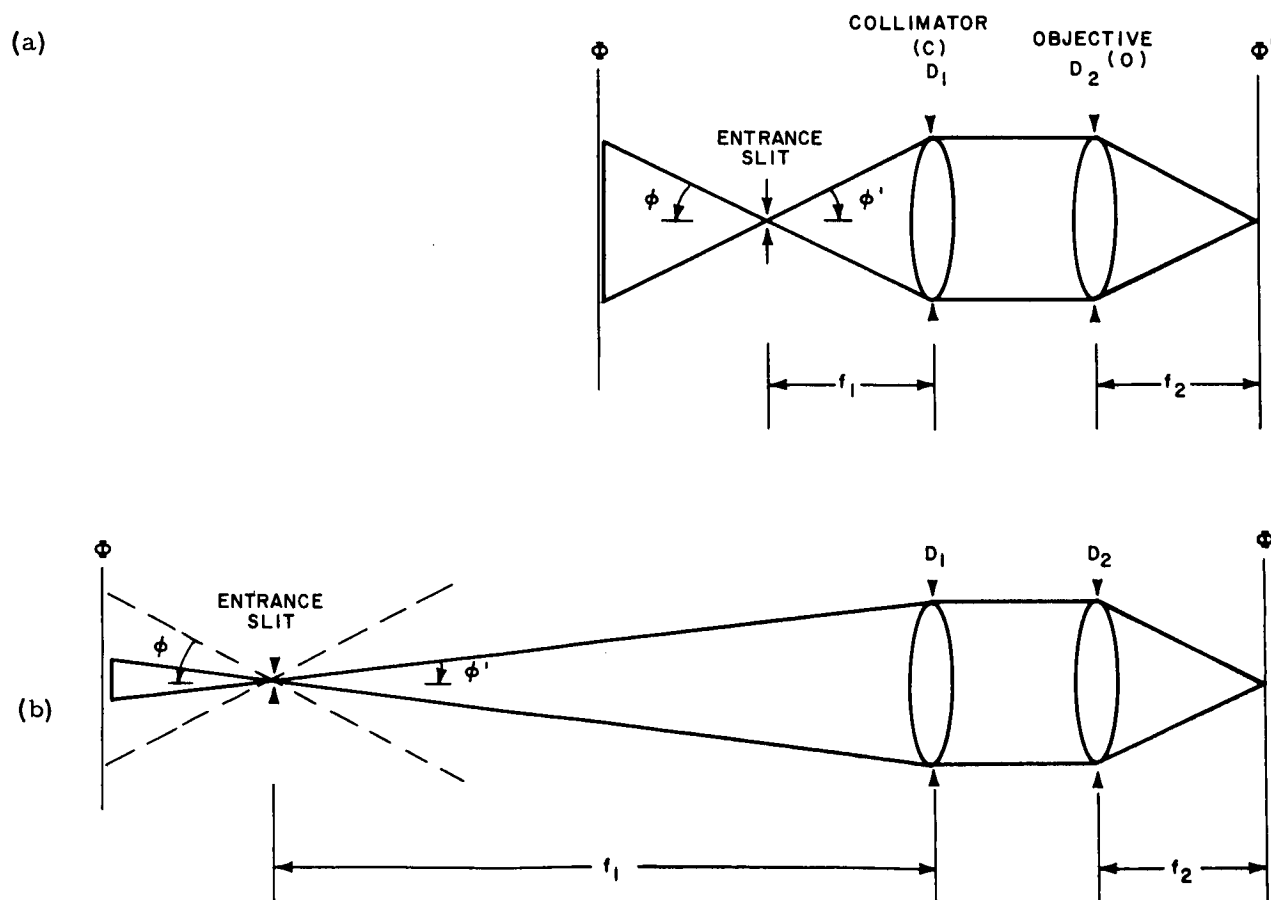
The grating is omitted, since dispersion is not a factor here. For simplicity, assume that the plane Φ is a broad source filling the angle ϕ and emitting a constant Lambertian flux i. The lens diameters D_1 and D_2 are fixed at 50 mm and let f_1 and f_2 be 75 mm. This then represents an F/1.5 overall system with M, the magnification ratio of slit to slit-image, being 1:1. Ignoring transmission loss, let us call the slit image brightness i' at the film plane Φ'.

Now let us consider the case (sketch b) where f_1 is increased from 75 mm to 300 mm, but all other parameters are maintained constant, including D_1. The collimator f_1 now no longer accepts the full cone angle emergent from the slit, and the total flux collection by f_1 is reduced by the ratio $\left(\frac{300}{75}\right)^2$ or a factor of 16. The collimater C is now an F/6 lens.

However, M is no longer unity, but 4:1 as reflected by f_1:f_2, and the total transmitted flux is focused into an area $(4)^2$ smaller than in the previous case. This results in the same power density at Φ' in both cases, and therefore the same film density. It is thus seen that optical efficiency is independent of the focal length, and henceforth F/No., of the collimater, and that an F/6 lens as collimator will produce the same film exposure as an F/1.5. (An F/4 collimater is more commonly available and was used in the actual instrument).

It is furthermore seen that, with all other parameters (including D_1) as a constant, decreasing f_1 has two and only two effects:

a. It narrows the seeing angle ϕ and

b. It reduces the size of the slit image.

The seeing angle is discussed later in this section. The factor of slit image magnification is rarely considered in spectrograph optical design since most classical systems necessitate a fixed M. The symmetrical Ebert-Fastie mounting, for example, must always result in a 1:1 ratio. The Bass-Kessler system however, permits flexibility in the f_1:f_2 ratio.

It may not be apparent why this geometry affects final resolution. Let us review the influencing parameters. Theoretical grating-limited resolution is orders-of-magnitude better than can be achieved by such a low dispersion, high aperture optical system. In practice, the limitations are a combination of three major factors:

1) Lens corrections

2) Threshold film resolution

3) Slit image width (with a fixed dispersion).

Assuming a possibly pessimistic lens-film threshold resolution of 50 line pairs/mm, two images could be just distinguised at a minimum separation of 20μ on the film. With a 200 A/mm first-order dispersion, this amounts to a theoretical slit image separation representing a 4 A bandpass, or 2 A in the second order. Ideally, the slit image width should be a maximum of half this width, but the 300-mm collimator provides a workable compromise in the $f_1:f_2$ ratio of 4: 1 and the resultant demagnification of $75 - \mu$ diameter fibers to a slit image of 19μ. It is seen that at a $f_1:f_2$ ratio of unity, the $75-\mu$ slit image width would severely limit resolution. In practice, the above resolution has been just achieved in actual ballistics tests using the very coarse-grained 1-F emulsion. The employment of slower and finer-grained films, if practical from an efficiency standpoint, will permit better resolution.

The above logic applies not only to the ideal Lambertian model, but also to consideration of the ablating particle as a line source of constant brightness or of the balloon interior as an integrating sphere. It may not apply to the more likely in situ case of the primary radiation from the spatially random fragmentation of a particle where the point of maximum emission cannot be predicted and probably will not be of a constant brightness during passage through the balloon. This must be taken into consideration; it is seen, however, that the further miniaturization discussed above results in the projection of a much wider optical field into the balloon. This, of course, also increases the seeing angle which must include the entire interior surface in order to record any near-tangential penetrations at highest efficiency.

Even with the widest field optics, there will remain some "dead" area within a spherical container. The use of conical test cells whose geometry matches the optical collection angle has been considered, but the sphere still appears to represent the optimum configuration, especially in terms of presenting the maximum possible internal particle path length to random incidence. Each individual fiber effectively contributes its illumination to a discrete point on a non area-integrating sensor such as photographic film. Therefore, such otherwise "dead" area in a sphere may be viewed by maintaining the parallel geometry of the fiber bundle's terminal end, but by arranging the input ends as shown in sketch (c) to provide overlapping fields encompassing the entire interior of the balloon. The sketch is simplified by illustrating the acceptance angles of only three individual fibers.

3. 5 DYNAMIC RECORDING RANGE

The potential dynamic brightness range encountered in this experimental concept is very broad. The primary factors are: (1) the inherent range in relative brightness emitted by different species at a given excitation level, and (2) the strong temperature and exitation dependence upon such variables as particle mass and velocity, especially in the in situ case. One approach to solution of the resultant dynamic latitude problem in recording has been to place a neutral
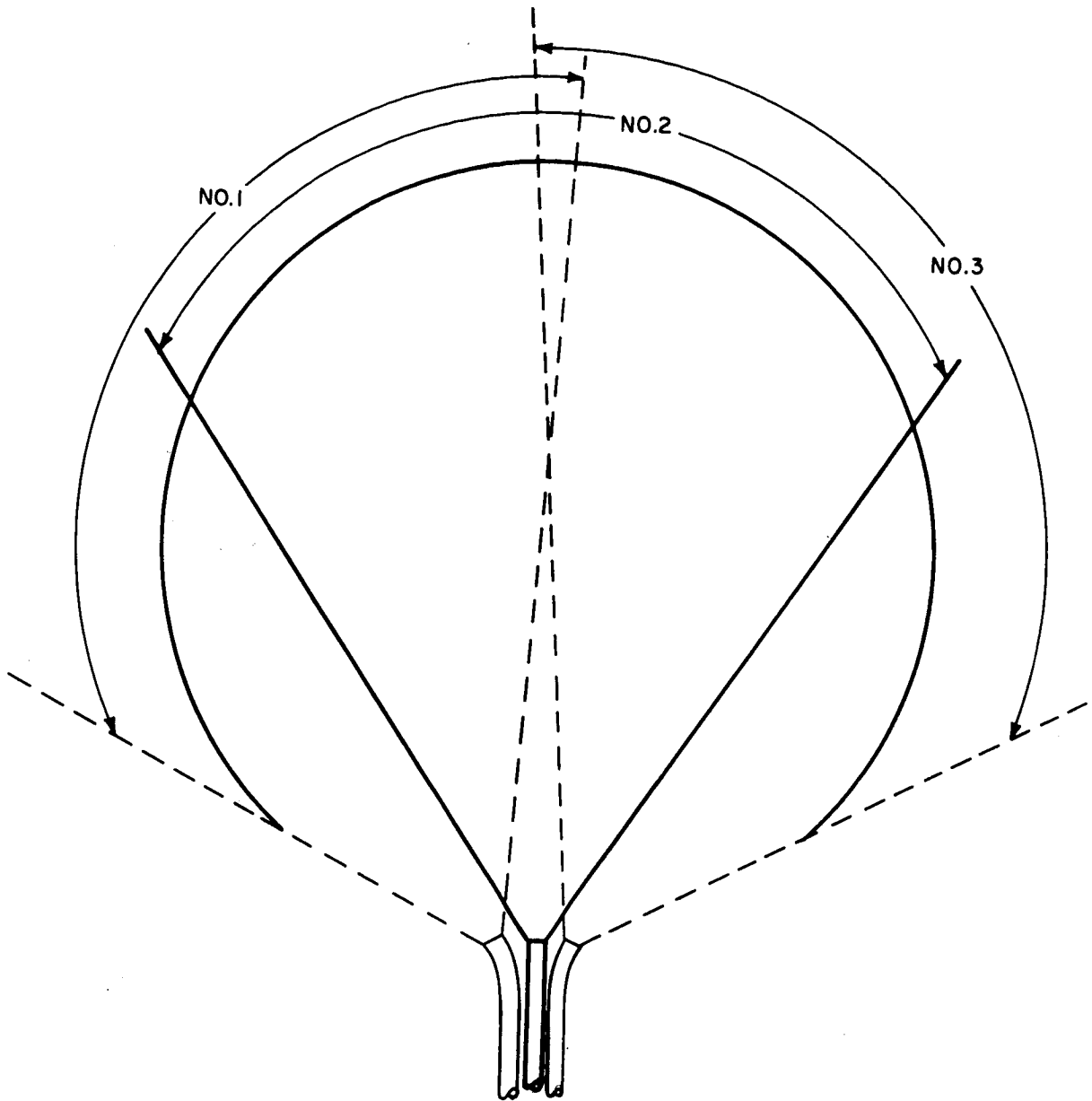
Sketch (c)

density attenuator wedge in contact with the terminal slit end of the fiber bundle. The present wedge covers a density range of 0 - 1.5 and results in a continuous attenuation along the height of the slit, allowing maximum transmission at the top as seen in Figures 13 through 21 (with the exception of Figures 13d and 14, exposed with an earlier fiber bundle attenuated by a step rather than continuous wedge. These step increments were too large for this experiment, resulting in some loss of information).

The gradient chosen was extremely helpful in data analysis of the spectral records resulting from this program. The faint lines may be accurately measured at the point of no attenuation, while the lines which would otherwise be saturated and quite broadened may be measured with comparable accuracy at the other extreme end of the attenuated slit image. The mercury calibration spectra represent the use of a wedge gradient not adequate for its brightness range. This results from sensitometric difficulties encountered in photo-miniaturization of the wedge.

A minimal effort was spent on further optimization of this technique by conventional photographic means, since the maximum wedge densities required in a flight instrument may exceed the D_{max} obtainable with silver halide emulsions. Other techniques, such as metallic vapor deposition, are being investigated.

Further extension of dynamic latitude is discussed in the portion of this report dealing with sensors (Section 4).

3.6 OPTICAL BANDPASS

The natural tendency in design of a spectrograph system is to try to attain a maximum spectral bandwidth. This is expecially so when dealing with analysis of unknowns. The realistic tradeoff is arrived at by considering two questions:

a. What are the practical restraints imposed by sensor and optical system characteristics?

b. Are these limitations acceptable in terms of producing sufficient data to meet the task requirements?

The bandpass of the present system is limited to an effective spectral range between 4000 and 6910 A. This is best shown by reference to the mercury calibration on any of the spectral records (Figures 13 through 20). The short wavelength cutoff is due to the attenuation of the fiber optics (see Figure 7) and the long wavelength cutoff represents the efficient response limit of the Kodak Class F Spectroscopic film (see Figure 6). This emulsion responds further into the red than most panchromatically sensitized films and exhibits
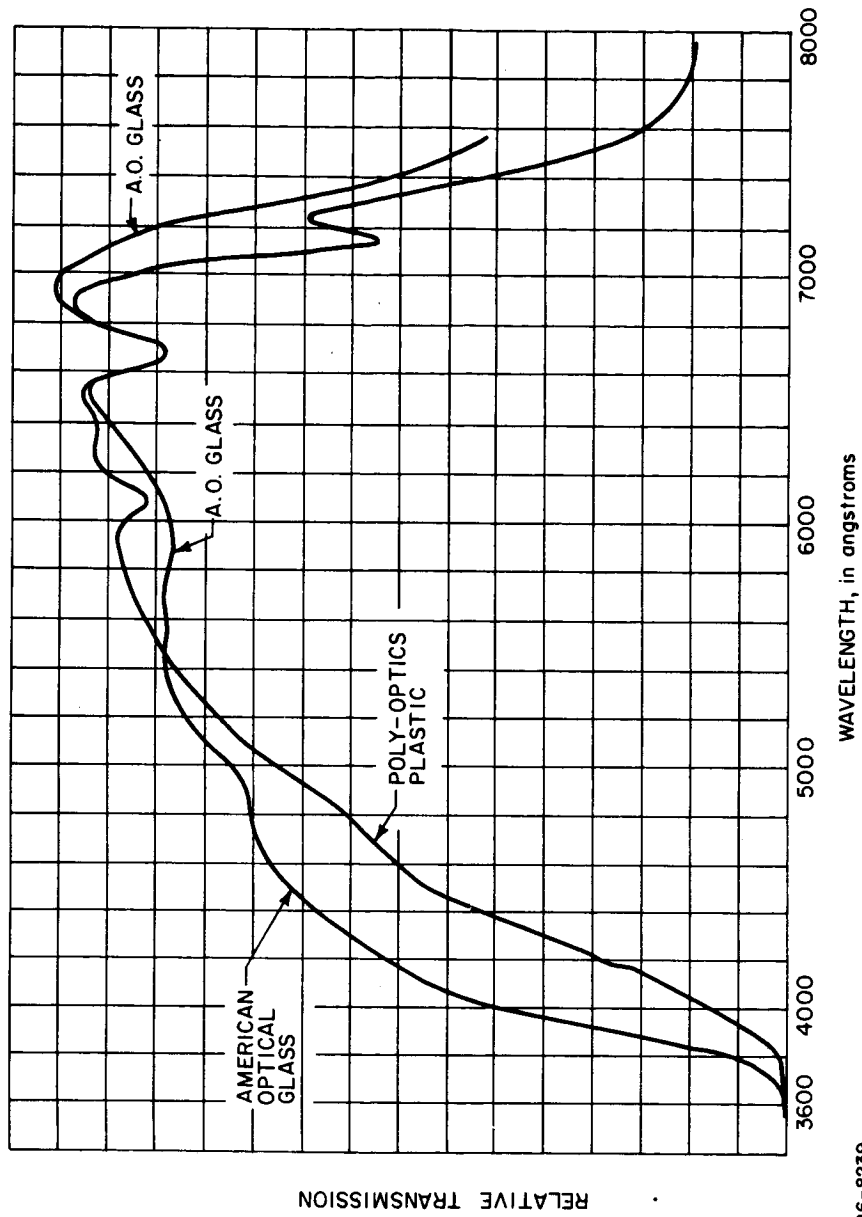
Figure 7 RELATIVE TRANSMISSION VERSUS WAVELENGTH FOR A 1-FOOT LENGTH OF PLASTIC FIBER OPTICS BUNDLE

86-8239

a very uniform sensitivity over the entire visible spectrum. Kodak Class I-F film was used in all experiments in this program. (The prefix "I" is a Kodak designation for "speed" or amplitude sensitivity, while the suffix "F" refers to spectral bandpass sensitivity. The I-F film is a Type I emulsion, representing the spectroscopic film of maximum overall sensitivity, with Class F dye sensitization, which gives the broadest bandpass response in the visible.) An appreciable extension of bandpass beyond this upper limit is possible only by use of infrared sensitized emulsions such as Kodak Spectroscopic Film Class N.[11] Such infrared films could be employed, but their sensitization makes them much more vulnerable to degradation by fog or noise background when exposed to high thermal environments.

The violet cutoff of the plastic fibers is slightly worse than that of optical glass fibers, but the gain in favorable mechanical properties outweighs this loss. The use of quartz as a fiber material is very inviting from an ultraviolet transmission viewpoint, even though mechanical problems might be worsened. To date however, the production of a cladding material or technique which would both provide reasonable transmission efficiency and survive even nominal environmental exposure, has not been achieved.

To summarize, we are presently limited to the visible spectrum or possibly the visible plus the near infrared. A great deal of earth-based meteor spectroscopy has dealt only with the visible. All of the experimental portion of this program has been limited to the visible and the resultant spectral data permit constituent identification which show excellent correlation with published analyses of meteor spectra (see subsection 7.3 of this report on evaluation of the experimental results).

Appendix A presents an analytical approach for semi-quantitative determination of meteoroid composition from spectral data limited to this optical bandpass.

One favorable result of this limited bandpass is avoidance of the problem of overlap of orders common to all broad bandpass spectrographs. It is apparent that with the slightly less than 3000 A range available, no overlap is possible. For example, a line appearing at a spatial position corresponding to 6000 A in the first order cannot represent second order 3000 A radiation, since this wavelength is not transmitted by the optics. By the same token, in looking at the second order, a 4100 A line cannot be confused with the first order 8200 A emission as the film cutoff is below the higher wavelength.

4.0 SENSOR STUDY

4.1 PHOTOGRAPHIC FILM

As discussed in the preceding section, Kodak type I-F emulsion was chosen to cover the 4000-7000 A bandpass. Consultation* with the Special Applications Department of Eastman Kodak Company has ensured that no major new product or application was overlooked. Relying upon such state-of-the-art information, a minimum effort has been expended in the quantitative evaluation of various emulsion characteristics.

The prime goal of this study has been to concentrate effort upon proof of feasibility of the experimental concept and, in so doing, to utilize existing instrumentation materials and techniques wherever compatible. One apparent exception to this policy was the construction of the breadboard Kodak Bimat film processor (See Figure 8) during the early part of this program. When this processing technique was first recommended in anticipation of requirement for on-board film development, it was concluded to be the most feasible method available, but only prototype hardware had been constructed and none was commercially available. The Bimat process still appears to be the best technique for such a requirement, and during the interval of this program has been employed in such in-flight applications as on-board development of aerial reconnaisance photographs and of Lunar Orbiter photographs of the moon's surface.

The process is seen to be out of the first development stages, and has been at least initially proven in both aircraft and satellite programs. It has been felt, therefore, that considerable emphasis upon laboratory experimentation with the process was not required and would detract from concentration upon the breadboard development and simulation experiments. The Bimat processor was constructed in accordance with Kodak's recommendations, and functions well, producing results similar to those obtained by conventional processing.

The Bimat process, [12, 13, 14] developed by Eastman Kodak Company, is a diffusion-transfer process employing no free liquids. The Bimat or "processing" film consists of a conventional photographic film base coated with a binder and then a silver halide solvent which develops the photographic negative when pressed into intimate contact. This is accomplished by "lamination" of the exposed negative and Bimat films by means of a pressure roller (See Figure 8). Development of the exposed film takes place while the films are in contact. When separated, a positive image is also presented by the Bimat film.

In addition to the prime capability of on board processing, this chemistry offers the possibility** of improved film sensitometric responses (such as increased dynamic latitude) so vitally necessary to this experiment. Exploration in this area will be quite important in future consideration of film as the sensor. Analysis of results from such programs as Lunar Orbiter should be helpful

*Private Communication
**Private communication, Kodak Research Laboratory.   -25-

NEGATIVE FILM
SUPPLY CASSETTE

NEGATIVE FILM
GUIDE ROLLER

COMMON TAKEUP SPOOL
FOR NEGATIVE AND
BIMAT FILMS

BIMAT FILM
GUIDE ROLLER

LAMINATION PRESSURE
ROLLERS

BIMAT FILM
SUPPLY

ALTERNATE BIMAT FILM
TAKE-UP FOR RAPID
PROCESSING

SPACER FOR 70 mm
BIMAT FILM
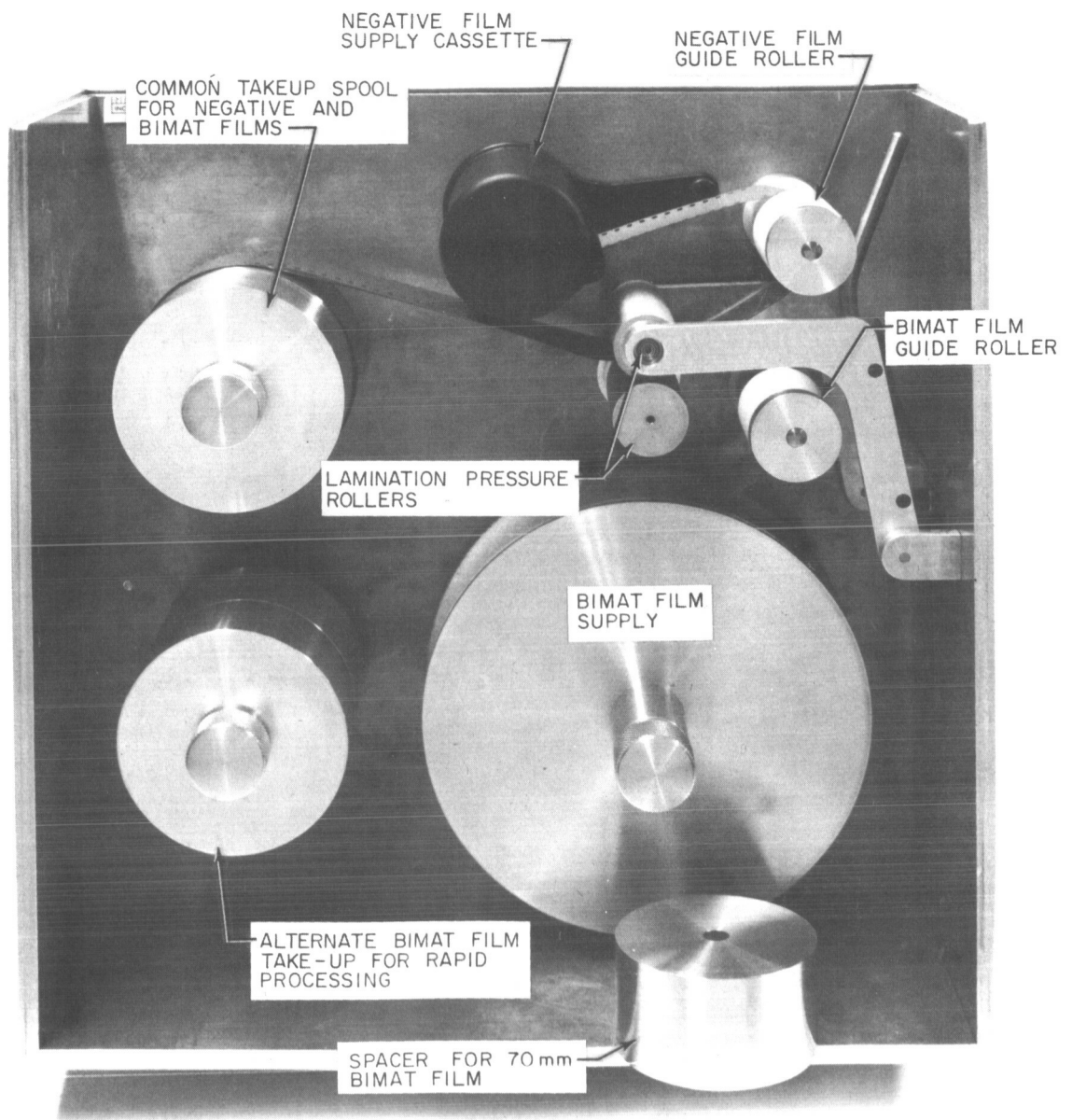
86-8240

Figure 8 PHOTOGRAPH OF BIMAT FILM PROCESSOR

in considering application to an experiment in a space environment.

It is to be borne in mind that this on-board processing technique is obviously not required in either the case of a manned mission or that of a satellite serviced by periodic rendezvous. It is also in competition with a vidicon camera system which must be considered in terms of the trade-offs involved in an unattended deployment.

4.2 VIDICON CAMERA TUBE

A majority of all ballistics tests utilized photographic film as the sensor. The experiments described in Section 2 employed a photomultiplier as a practical instrumentation expedient. In contrast, another series of experiments used vidicons with the intent of proving their practicality as an alternate sensor. This is in the anticipation of an in-situ condition where the mission requirements may preclude the use of a silver halide film as a sensor. Such requirements might include an unmanned mission of extended duration resulting in vehicle exposure to a hard background radiation level high enough to saturate a photographic emulsion. Electronic circuitry has a considerably higher resistance to radiation levels than most films and does not time-integrate in the same sense as does film. Use of a vidicon may necessitate a higher degree of systems sophistication. It is therefore considered solely as an alternate sensor and tests employing vidicons have been limited to those experiments considered necessary in order to prove compatibility to the proposed instrumental concept.

Vidicon camera systems with high resolution and sensitivity have been developed for use in the space environment by such programs as TIROS, Ranger, Apollo, and the Advanced Vidicon Camera System (AVCS) of the Nimbus meteorological Satellite [15]. Section 8.3 of this report illustrates application of the Apollo camera system to a flight version of this experiment.

Only one vidicon parameter essential to proof of feasible application to this project has not been previously demonstrated. This is the ability of the vidicon tube to respond with sufficient efficiency to an input flux of microsecond-order duration. It has been established [16] that both the standard and special slow-scan tubes do function at exposure ranges down to 1 millisecond and that neither exhibits reciprocity failure within the exposure range from 1 second to 1 millisecond. No data are available, however, for exposures below 1 millisecond. It was therefore concluded that experiments must be conducted to prove extended response capability to the short times involved in particle ablation at high velocity. Vidicon equipment available in this laboratory was used for these tests. Resolution of this equipment is quite poor, but adequate to resolve enough line structure to prove response to short duration exposures. It was felt unnecessary to procure a costly state-of-the-art, high-resolution system for this task. Two series of experiments were conducted: the first using a slow-scan system which was constructed in the laboratory, and the second using a commercial closed circuit TV system employing the conventional

-27-

525-line, 30-frame per second scan. In both cases, the main purpose of the experiments was to obtain exposures from event durations in the order of 1 microsecond and to form a basis of comparison between the sensitivities of the vidicon and photographic film at the exposure levels and durations encountered with the spectrograph.

The slow-scan system was designed around an RCA type 7735A vidicon and employed a scan rate of 3 frames per second. Although the 7735A was not designed for slow-scan applications, it was felt that it would be satisfactory for this experiment. However, the maximum resolution obtainable in the experiment was only about 30 TV lines, presumably due to lateral charge leakage along the photoconductor layer during the long framing time. Tests made with this system successfully demonstrated that the vidicon would store and read out an image that was exposed to the photoconductor for only 2 microseconds. To perform this experiment, an Angenieux 1-inch F/0.95 lens was used to image a bar chart on the photoconductor surface. A Compur shutter set at 1/200 second was placed in front of the lens to serve as a capping shutter. Its synchronizing contacts were used to trigger a General Radio Microflash unit which front illuminated the bar chart. The sync contacts also initiated the horizontal sweep generator that scanned a single 600-line frame and displayed the image on an oscilloscope.

The final feasibility test was to record spectral data from a ballistics range shot which would require considerably higher resolution than was obtainable with this system. Rather than expend the time necessary to redesign the slow-scan system, it was decided to use a conventional closed circuit TV system available in-house. This unit was a Sylvania Direct-Wire TV camera, Model 101. A commercial 21-inch portable TV receiver was used as a monitor. The resolution of this combination was about 150 TV lines, quite poor by modern standards, but adequate for recording the presence of spectral lines. Preliminary qualitative measurements of the camera sensitivity were made by observing the xenon spectrum produced by the G. R. Microflash unit. To perform this experiment the Microflash unit, which was pointed at the end of the fiber optics bundle, was triggered by the sync contacts of a Linhoff camera used to photograph the TV monitor. The Linhoff was set for a 1/25- second exposure so as to photograph only one complete frame on the monitor. Ideally, the vidicon photo-conductor should be placed in the film plane of the spectrograph. This could not be done with the existing mechanical arrangement and the use of relay optics was required to focus the real image at the film plane of the spectrograph onto the photoconductor. (See Figures 9a and 9b).

This requirement reduced the effective sensitivity of the system by a factor of approximately 10. The photograph in Figure 9c shows the exposure obtained by a single, 2-microsecond xenon flash. The resolution of this photograph is obviously too poor to obtain spectral information, but it does indicate that with a higher resolution system, information could indeed be obtained. The vidicon camera was then removed and type I-F spectroscopic film was loaded into the spectrograph. A series of single, 2-microsecond exposures was made with
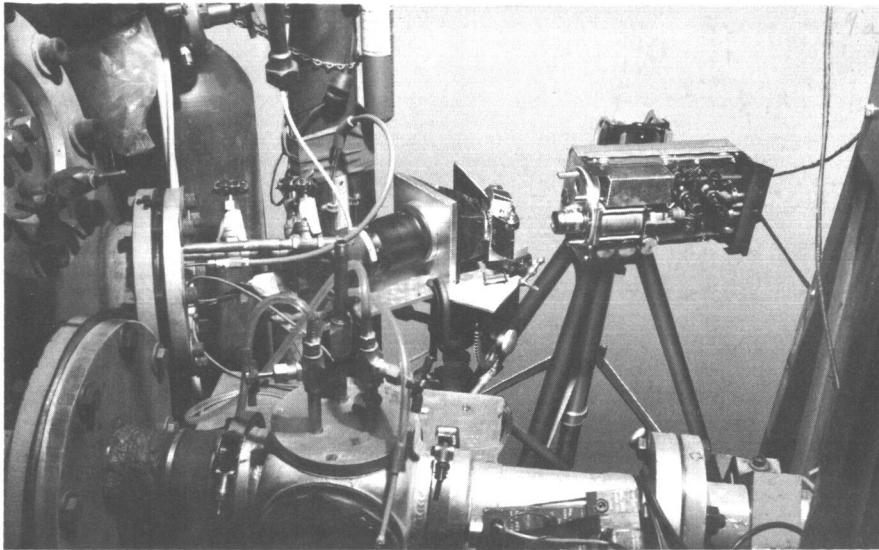
Figure 9a PHOTOGRAPH OF CLOSED CIRCUIT VIDICON CAMERA--SPECTROGRAPH
SETUP ON BALLISTICS RANGE
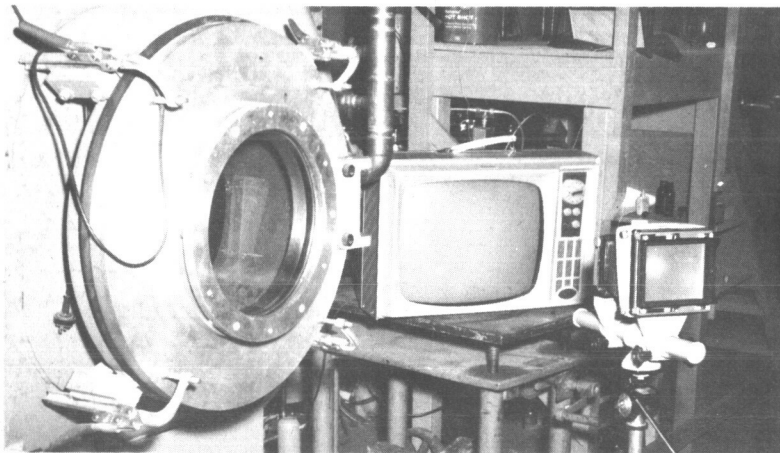
Figure 9b PHOTOGRAPH OF VIDICON MONITOR SETUP ON BALLISTIC RANGE
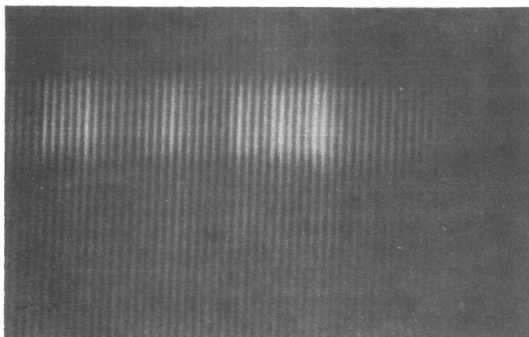
86-8241

Figure 9c SPECTRA FROM VIDI-
CON SYSTEM EXPOSED TO 2-
MICROSECOND PULSED XENON
FLASHLAMP
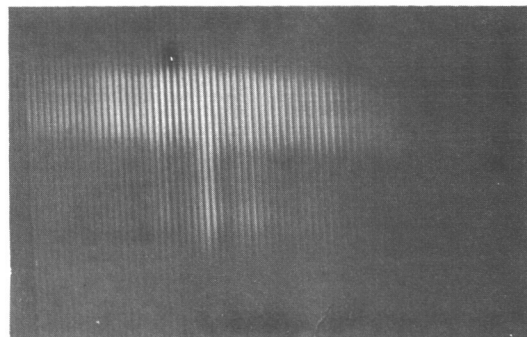
Figure 9d SPECTRA FROM VIDI-
SYSTEM OF IN-FLIGHT ABLATION
OF SODA LIME GLASS SPHERE

-29-

different neutral density filters in front of the fiber optics bundle. The best exposure was obtained with an ND 1.0 filter which coincidentally just compensated for the factor of 10 loss in sensitivity due to the relay optics in the vidicon camera.

The final and most conclusive tests consisted of actual ballistics range shots using the vidicon camera as the sensor. The optical arrangement was the same as that used with the Microflash unit. The results of such a shot are shown in Figure 9d.

As previously mentioned, these tests employed a system very inferior in comparison to modern instruments and were not intended to provide a quantitative measure of either reciprocity failure or of sensitivity, but rather to prove response to exposures in the microsecond range and to give a "ballpark" comparison between the sensitivities of photographic film and a vidicon under identical conditions. It can be concluded from these tests that such exposures are compatible with vidicon characteristics and that the relative sensitivities of Kodak type 1F spectroscopic film and the Sylvania vidicon system used in these tests are quite similar in this microsecond exposure range.

5.0 SPHERICAL TEST CELL

5.1 PROTOTYPE DESIGN

The final phase of the experimental program employed breadboard versions of the proposed 6-inch diameter spherical test cells. These balloons were fabricated from bilaminated 0.0005-inch aluminized Mylar. The vapor-deposited aluminum layer was 2500 A thick, meeting NASA specifications of the Pageos program. Fabrication was by the G. T. Schjeldahl Co., using a multiple gore technique. Edges of the total of eight gores were butt-joined and heat-sealed with a tape of the same bilaminated Mylar. The parent polyester from which Mylar film was produced served as the adhesive. A simple vacuum-tight fitting was attached to permit an "O"-ring seal to a mating fitting which housed the fiber optics bundle as well as supply lines to vacuum pump, gas supply, and manometer. The aluminum coating served to both shield the optical path from ambient external light and to enhance the optical signal by internal reflection.

These balloons met the experimental requirements of this feasibility program. They withstood the required maximum 300-torr pressure differential with minimum leakage and provided a satisfacotrily opaque envelope enclosing the open optical system. An appreciable reflectance gain was realized as compared to a non-reflecting test cell. Analysis of the spectral records reveal no contribution from either the Mylar membrane or the aluminized coating.

The gore method of fabrication was selected for the breadboard model solely as a cost expedient. Other techniques such as drape forming or casting offer a number of technical advantages, but require considerable tooling costs. These costs are negligible when prorated over production of the many balloons required for prototype or flight hardware, but are disproportionately high for the 20 units involved in this breadboard feasibility program. This gore-type fabrication is essentially a scaling down of the construction approach employed in assembly of the Echo satellite. It is basically a hand assembly involving virtually no tooling costs. The results were quite adequate for the laboratory-experiments, but this approach is not recommended for advanced design consideration.

The prime disadvantage of the gore design is the high percentage of projected surface area consisting of multiple side wall thickness. In the equatorial region, every seam presents an area of double thickness due to the tape plus adhesive. The polar regions apparently represent the worst case, where a sealing tape overlaps eacn gore end junction. This defeats the goal of decreasing sidewall thickness in order to create an absolute minimum resistance to penetration by the low-mass micrometeoroids. The drape-forming technique reduces the severity of this overlap problem by using molds to thermally form hemispheres from a single section of membrane. Two hemispheres are then sealed together by a single equatorial tape joint. This is a proven production method with Schjeldahl. The employment of a casting technique avoids all joints and provides a single membrane thickness for the entire spherical surface area. This

technique is now in the experimental stage of development at Schjeldahl. Satis-
factory castings of polyurethane spheres have been made, but not with a
minimum sidewall thickness practical for this experiment.

Another undesirable feature of the gored balloons is the increased tendency to
leak due to the considerable handling required in fabrication and the manual
difficulties involved in producing perfect multiple joint seals in such a small
sphere. Such leaks in the breadboard balloons were small and in no way
hindered the ballistics feasibility program, but would constitute a major prob-
lem in long-term deployment. Extended time leakage measurements of these
balloons were planned but abandoned since this would constitute a measurement
of leakage primarily due to this fabrication method which is not proposed for
advanced design. It is not felt that this compromises feasibility, since drape-
formed Mylar balloons have been satisfactorily flown for extended missions
whose design requirements closely approximate the gas encapsulation demands
of this experiment, as indicated in the following section.

5.2 LEAKAGE PERFORMANCE

The goals of space vehicles such as Echo do not require permanent or even
long-term positive pressurization. Those of weather balloons do, however,
and the results of several "super-pressure" weather balloon flights are pre-
sented below. *

These data are not truly quantitative, since no pressure transducers were flown.
The results are nevertheless encouraging in terms of leak rate as evidenced
by the stability of ±1000 feet in reference to design altitude. This variation
of course does not of necessity represent any amount of leakage but may all
be accounted for by thermal equilibrium rise times. It is to be noted that in
no case does the mission length represent a maximum duration limited by the
performance of the experiment. All flights were terminated by ground control
for non-technical reasons. All contract numbers reference tasks performed
by G. T. Schjeldahl Co.:

    a.   Contract: AF19(628)62-2639

          Agency: ESD, Bedford, Massachusetts

          Description: A 34-foot diameter balloon of 3/4- x 3/4- mil
                                bilaminated Mylar, cut down at end of 30-day flight
                                at an altitude of 67,000 feet ±1000 feet.

    b.   Contract: AF19(628)62-4334

          Agency: ESD, Bedford, Massachusetts

          Description: Identical to a. above

_____
* Private Communication, G. T. Schjeldahl Co.

c. Contract: AF19(628)2770

    Agency: ESD, Bedford, Massachusetts

    Description: Identical to a. above

d. Contract: AF19(628)

    Agency: ESD, Bedford, Massachusetts

    Description: Identical to a. above but 80,000 foot altitude.

e. Contract: 11679-65

    Agency: NCAR, Boulder, Colorado

    Description: A 5 foot diameter balloon of 3/4- x 3/4-mil
                     bilaminated Mylar of 5-foot diameter, cut down at
                     end of 100-day flight at an altitude of 67,000 feet
                     ± 1000 feet.

These balloons were all flown pressurized so as to produce 10,000 pounds per square inch skin stress or 60 percent below the theoretical yield of the Mylar. This pressurization results in a differential of the order of 10 torr, a figure representing the absolute maximum pressure under consideration for a flight version of the micrometeoroid analyzer system. The sidewalls of the weather balloons are thicker than we propose, but the skin stress is tremendously higher than will be encountered by a smaller balloon of a diameter on the order of 20 cm with the same pressure differential. The important thing is that balloon flights under similar conditions and of a least 100-day duration have been successful. It seems probable that deployed balloon "shelf life" in a space environment will be far less affected by inherent materials and fabrication limitations than by punctures from particles below the signal threshold of the system.

The following test data (Table I) from the Schjeldahl research laboratory shows the relative permeability of various Mylar films and indicates excellent tradeoffs possible with thinner membranes than those used in the above flights. The use of a dense gas such as argon or xenon will represent a far more favorable diffusion case. Also note the relative gain produced both by aluminizing and by lamination. No sample was tested which represented a lamination of aluminized membranes. It is assumed that this combination will even further reduce diffusion through the sidewall.

TABLE I

TEST DATA OF MYLAR PERMEABILITY*

(A) In Units of cc/mil/100 in.^{2}/24 hr/atm:

$$N_2 = 1$$

$$O_2 = 8$$

$$H_2 = 100$$

$$CO_2 = 16$$

(B) Hydrogen permeability in units of liters/m^2/24 hours with a 3 cm H_2O pressure differential across a diaphragm and ambient conditions of air at 77F and 760 mm Hg:

1/4-mil Mylar =	5.0
1/4-mil metalized Mylar =	3.2
1/4- x 1/4-mil Mylar, bilaminate =	1.3
0.35-mil Mylar =	1.8
0.35-mil metalized Mylar =	0.5
1/2-mil Mylar =	2.0
1/2-mil metalized Mylar =	0.1 to 1.0
3/4- x 3/4-mil Mylar, bilaminate =	0.6
1.0-mil Mylar =	0.9
1- x 1-mil Mylar, bilaminate =	0.35

*Private Communication from G. T. Schjeldahl Co., August 25, 1966.

These test data are the most recent available for the materials tested. They are offered only as a guideline and not as a guarantee of reliability or results. It is subject to change as new test data and experience are gained. Significant comparisons include the effect of metalizing, the effect of double layers, and the effect of thickness.

5.3 UV VULNERABILITY

Mylar and all similar materials are subject to deterioration by continued exposure to UV radiation. Aluminum is generally considered the most efficient protective filter when overcoated with a virtually monomolecular covering of SiO to retard oxidation while in the earth environment. Numerous laboratories have conducted accelerated solar radiation experiments to simulate extended exposure to the space environment. There appears to be considerable disagreement as to the validity of such accelerated "multiple sun" exposures and absolute values cannot be quoted at this time. There is no present evidence that UV degradation will constitute the limiting parameter of deployment time. The following correspondence from the Schjeldahl research laboratory indicates the efficiency of vapor deposited aluminum in attenuating solar radiation. The transmission of an evaporated aluminum film (of thickness x) to light of wavelengths greater than or equal to 0.2 is less than the upper bound given in Table II.

TABLE II

UV TRANSMISSION OF EVAPORATED ALUMINUM FILMS

x (A)	Upper Bound on Transmission for All λ's $\geq$ 0.2 μ
100	2.9×10^{-1}
300	2.3×10^{-2}
600	4.3×10^{-4}
1,000	3.6×10^{-6}
3,000	4.0×10^{-17}
6,000	2.0×10^{-33}
10,000	3.2×10^{-55}

5.4 OPTICAL OPACITY

The expression[17] for the reduction of amplitude of a light wave of wavelength λ, after traveling a distance x in a medium having an absorption coefficient k is $\exp(-2\pi xk/\lambda)$. Since the intensity of an electromagnetic wave is proportional to the square of its amplitude, the intensity is reduced by a factor $\exp(-4\pi xk/\lambda)$.

One problem under consideration here is how thick the aluminizing on the Mylar should be to ensure that sunlight impinging on a sphere made of this material in space does not deteriorate the Mylar and does not penetrate into the sphere. The expression does not take into account the reflection of solar radiation by either surface of the aluminizing -- only what happens inside the aluminizing. As such then, the expression is an upper bound on the fraction of sunlight energy of wavelength λ impinging on the sphere which gets through the aluminizing material to the Mylar.

The absorption index k for evaporated aluminum as a function of wavelength is given in Reference 18. From this figure one estimates that $K \geq 2.0$ at $\lambda = 0.2$ micron. From the Johnson[19] solar constant curve, one has that 0.02 percent of the sun's energy lies at wavelengths $\leq 0.2\mu$.

For those wavelengths greater than 0.2μ, one can say that the fraction of the energy at these wavelengths incident on the aluminizing which gets through to the Mylar is less or equal to the upper bound given in Table II and may be considered quite negligible.

Opacity of the balloon envelope is required to shield the constantly open optical system from ambient light. The preceding data from the Schjeldahl research laboratory indicate the performance of an aluminum coating in such shielding. A transmission of 4×10^{-17} is typical for a coating 3000 A thick. Experiments were scheduled to measure the opacity of the breadboard balloons to a simulated solar flux, but again this measurement proved to be meaningless due to problems resultant from the gore construction. Each Mylar layer was aluminized prior to lamination, resulting in good masking of the pinholes commonly present in single coat vapor deposition. Unfortunately, however, the manual taping of the small gores resulted in many areas with a nonuniform layer of adhesive varying up to twice the single Mylar thickness. This produced heavy, stiff interfaces at some joints resulting in crease marking of the aluminum coating as a result of handling and folding in packaging and inflation. The consequent light leakage is not high, but makes absolute measurement almost completely meaningless. Fabrication by drape forming will greatly minimize these rigid interfaces and the consequent handling and packaging damage.

6.0 FIBER OPTICS LIGHT RELAY

The use of a fiber optics bundle is considered the only feasible currently available techique for relay of light from a number of individual balloon test cells to a common spectrographic instrument. Fiber bundles have good transmission efficiency (typically at least 90 percent for one foot path length in the visible) and provide a flexible, strong and lightweight mechanical coupling in terms of packaging and deployment in an instrument system. The plastic fibers used in this feasibility study represent a very considerable improvement over glass fibers in their mechanical properties, permitting flexing and bending to a radius of curvature approaching 1/20 of the fiber diameter. Figures 10a and 10b show photographs of the cylindrical input end and slit output end of the bundle used in the breadboard spectrograph. It will not be attempted here to review the general characteristics of fibers as light piping devices, but rather to point out a few considerations pertinent to this specialized application as both light relay and input aperture to the spectrograph.

As shown in Figure 7, the optical transmission bandpass for the plastic fibers is somewhat poorer than that of comparable glass fibers, as evidenced by the attenuation in the short wave length region. This is undesirable, but the cutoff is not severe and is considered acceptable as a tradeoff against the superior mechanical strength properties.

Several of the parameters usually of great interest in the analysis of the light gathering or collection efficiency of fiber bundles are of virtually no consequence in this instrumental technique so far as efficiency is concerned. These include: individual fiber size, total number of fibers per individual bundle, and packing density, or the ratio of transmitting fiber core to non-transmitting cladding and potting material. This nondependence is due to the non-area-integrating nature of the sensor, where power density at the sensor surface is the only criteria for gaging real collection efficiency. Increase in either size, number or packing density of the fibers results of course in more total collection of light from within the test cell, but does not affect the power density at the input ends of individual fibers and consequently no increase of flux/unit area can be realized at the film plane where their terminal ends are finally imaged. Thus, these parameters may be deemed variables to be defined in other optical and mechanical tradeoffs.

An individual fiber diameter of 75μ was chosen for the present instrument. A smaller size was desired in order to obtain the same slit image width and resolution but with a more compact, shorter focus collimator. The 75-μ fibers, however, were the smallest currently in production by the manufacturer, Poly-Optics, Inc., of Paramount, California. (Subsequently other firms including E. I. duPont have announced commercial production of plastic fibers). This size was therefore accepted in order to avoid delay of the experimental program.
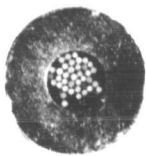
Figure 10a PHOTOGRAPH OF FIBER OPTICS BUNDLE SHOWING THE ENTRANCE END
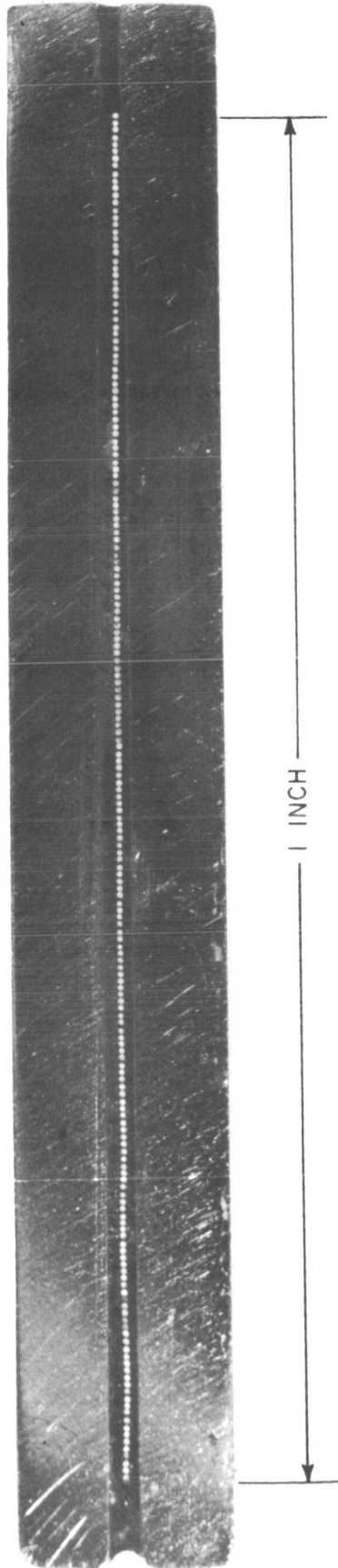
Figure 10b PHOTOGRAPH OF FIBER OPTICS BUNDLE SHOWING THE TERMINAL END

86-8242

-38-

Fibers with diameters down to a few microns have been produced and a much smaller size than this 75-μ diameter is feasible and will be used for the advanced design instrument. Within the limits imposed by the maximum grating dispersion possible, reduction of fiber diameter results in a linear scaling down of optical path length and consequent instrument packaging volume with no loss in data resolution. This is discussed in further detail in the discussion of the spectrograph design. As noted in this discussion, the use of 18.75-μ diameter fibers in the present optical system would permit the use of a 75-mm collimator instead of the present 300-mm focal length. The consequent 1:1 imaging of the fiber slit to the film would result in identical resolution with no effect upon dispersion and a 16 x gain in field acceptance angle within the test cell. The use of the 18.75-μ fibers with a 1200-line/mm transmission grating would yield the same data results in conjunction with both collimator and objective lenses of only 37.5-mm focal length. The resultant packaging gain is apparent in comparing the $f_1 + f_2$ distance of 75 mm to the 375 mm of the breadboard instrument. (This total is somewhat less than 375 mm due to the use of a telephoto design collimator with the consequent reduction in back focus).

The total number of fibers in the breadboard bundle was chosen to fill a 1-inch high terminal slit at maximum standard packing density. This height is much more than necessary for data reduction but was utilized solely to check the optical performance of the system over a wide collimator field angle in anticipation of the future requirement of a matrix slit composed of bundles from many balloons.

Packing density of the input fiber ends is of no major importance; that of the terminal or slit end must be optimized in an advanced design, again to allow efficient packaging of many bundles into a matrix slit configuration. The present bundle represents standard commercial production techniques. Current fabrication techniques permit packaging with fibers in actual contact, presenting the most efficient possible packing density in a given configuration.

The acceptance or collection angle of fibers is quite wide compared to other types of optical systems. Fibers have been constructed with core-cladding combinations of refractive indices which approach the theoretical maximum numerical aperture. In practice, however, there exists neither a standard technique for empirical measurement nor a numerical standard for determination of what constitutes the "cutoff" point at the extreme limits of the accepted field angle. For example, the plastic fibers used in this instrument are rated at an included acceptance angle of approximately 35 degrees, yet careful optical bench measurements indicate a transmission of better than 2 percent at an extreme half-angle of 42 degrees, representing a field of 84 degrees. This becomes quite academic, however, since anything approaching this degree of attenuation is intolerable in practical design. We shall therefore consider the

problems of acceptance or seeing angle within the balloon by using the conventional equation where the maximum acceptance (half) angle is given by:

$$\phi_{max} = \sin^{-1} \sqrt{\frac{N_1^2 - N_2^2}{N_0}}$$

where

N_0 = refractive index of air

N_1 = refractive index of the cladding material

and

N_2 = refractive index of the core transmitting material

Substituting for the values of the plastic fibers,

$$\phi_{max} = \sin^{-1} \sqrt{\frac{1.58^2 - 1.47^2}{1}}$$

$$= \sin^{-1} 0.579$$

$$= 35 \text{ degrees } 23 \text{ minutes}$$

The included acceptance angle then = 70 degrees 56 minutes. This also defines the numerical aperture of the fibers, since, by definition:

$$\text{N.A.} = N_0 \sin \phi_{max} \text{ , or } 0.579$$

A comparison with the conventional F/number system of rating lenses is shown by:

$$\text{F/number} = \frac{1}{2NA}$$

$$= \frac{1}{2(0.579)}$$

$$= F/0.86$$

The present collimator is a F/4 lens of 300-mm focal length and consequent 75-mm diameter. By simple geometry, and assuming simple lens theory, the included field of the collimator is 14 degree 12 minutes. Projection of this angle to the balloon interior shows that the present instrument views a trajectory length of only 0.75 inch in the case of a particle penetrating the balloon radially and normal to the optical axis. It was shown previously that this does not lower optical efficiency.

As also discussed previously, it is practical to considerably reduce the collimator focal length and thereby increase its N.A. or acceptance angle ϕ. However, the optimization of ϕ in fibers, collimator and objective will still leave some "dead" area in the test cell, and transmission efficiency will be reduced at the extremes of the field in spite of balloon reflection efficiency.

An advanced design will therefore employ a deviation from the conventional packaging where the fiber ends are parallel and the bundle input end forms a right cylinder. One approach would be that discussed in subsection 3.3 of this report, where ends of individual fibers view different but overlapping portions of the test area in order to avoid missing radiation from any near tangential penetrations. Since each fiber transmits to its unique area on the sensor, power density might vary along the slit-image height, but the maximum would still represent the highest transmission efficiency possible.

The fiber bundle used in the breadboard system was designed with two cylindrical input bundles terminating in a common exit slit as shown in Figure 5. The first, composed of 75 percent of the total number of fibers, transmitted the radiation from the balloon test cell. The second portion was used to record calibration exposure from a standard source, usually a low-pressure Osram mercury arc lamp. Figure 10c illustrates the resultant slit output by directing white light into the input ends which are placed at different distances from the source.

The flight instrument version of this design must employ a minimum of 100 balloon test cells, each equipped with a fiber optics relay bundle terminating in a slit configuration as described above. This results in a matrix or composite array of 100 small slits at the focal plane of the collimator. The optical system must be capable of accepting the illumination from the off-axis individual slits without degradation of the resultant dispersed slit image. This problem was simulated by means of the slit-holder device illustrated in Figure 10d. Separate film exposures to an Osram calibration lamp were made with discrete lateral displacements of the slit between successive exposures. The resultant composite print is shown in Figure 10e. The lateral displacement is deliberately exaggerated in the print in order to illustrate the movement.

It is seen that the off-axis positioning of the slit does not result in image degradation due to astigmatism or other aberrations. The only apparent difference between axial and off-axis slit positioning is the mechanical masking of extreme wavelengths by the camera film plane aperture. This masking results only because of camera and camera lens alignment to include two dispersive orders, and does not occur if alignment is made to record only the first order.
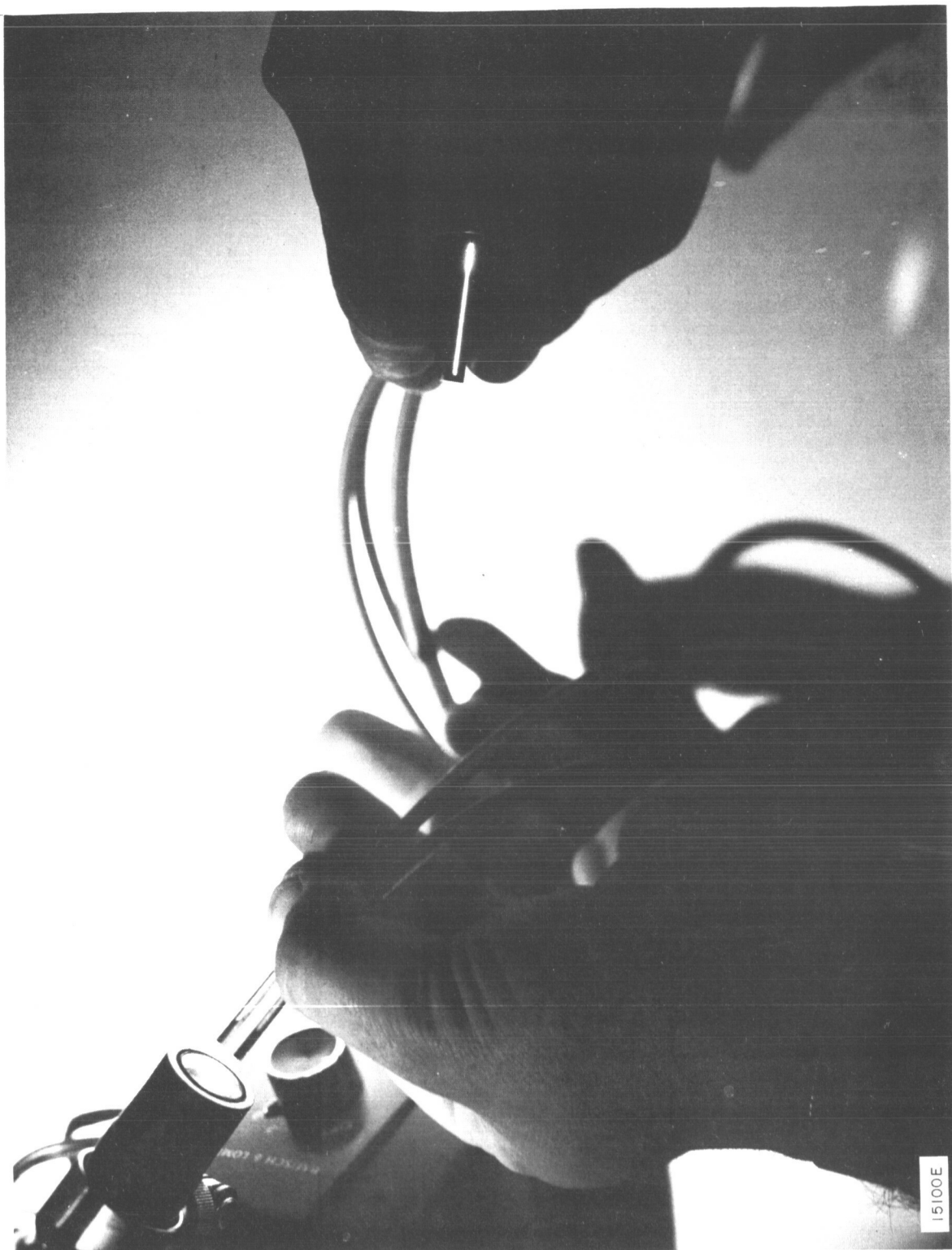
Figure 10c PHOTOGRAPH ILLUSTRATING DUAL INPUTS TO FIBER OPTICS BUNDLE

15100E

-42-
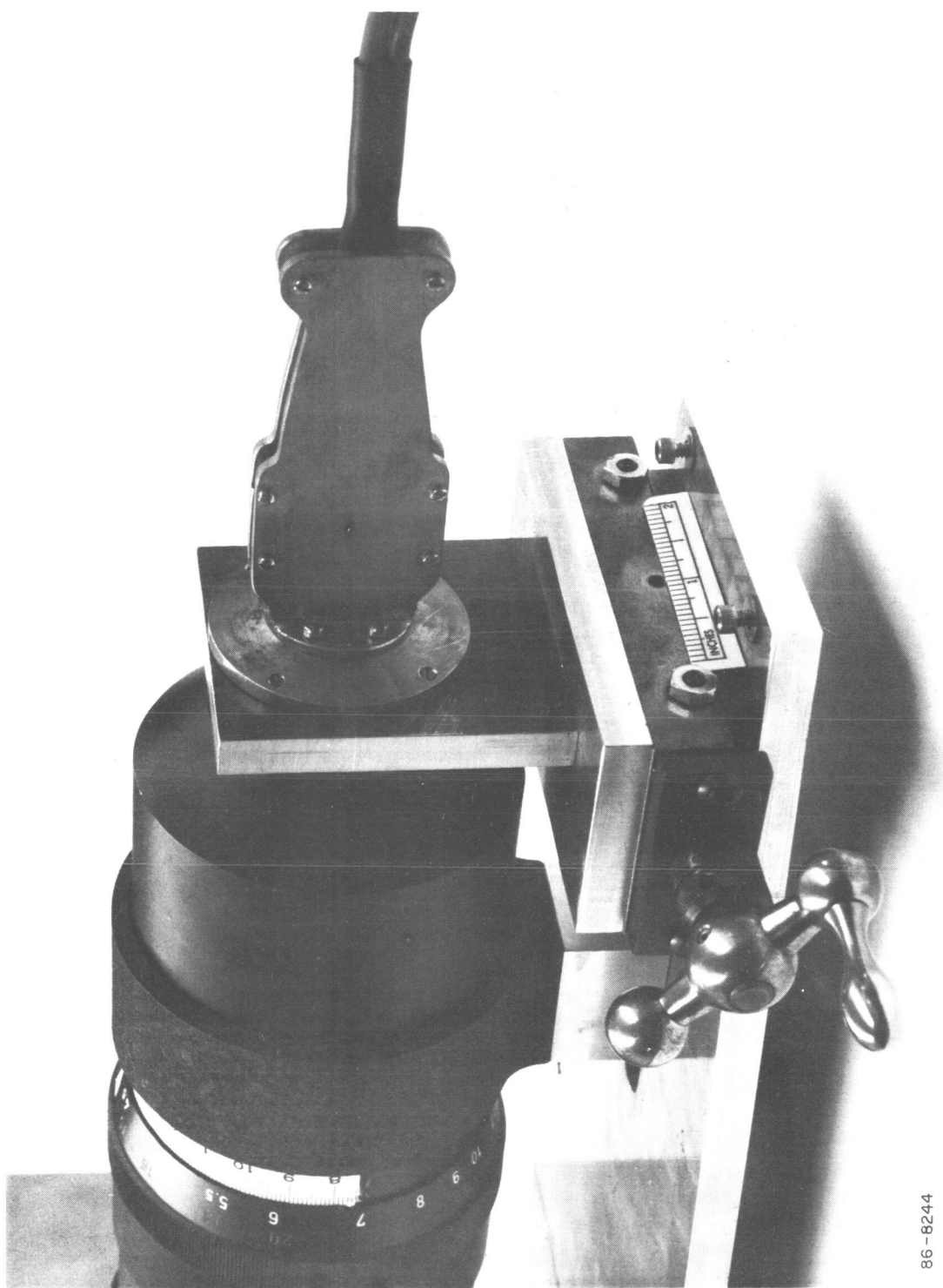
Figure 10d PHOTOGRAPH SHOWING AUXILIARY MOUNT FOR SIMULATION OF MATRIX
SLIT INPUT TO SPECTROGRAPH

86-8244

-43-
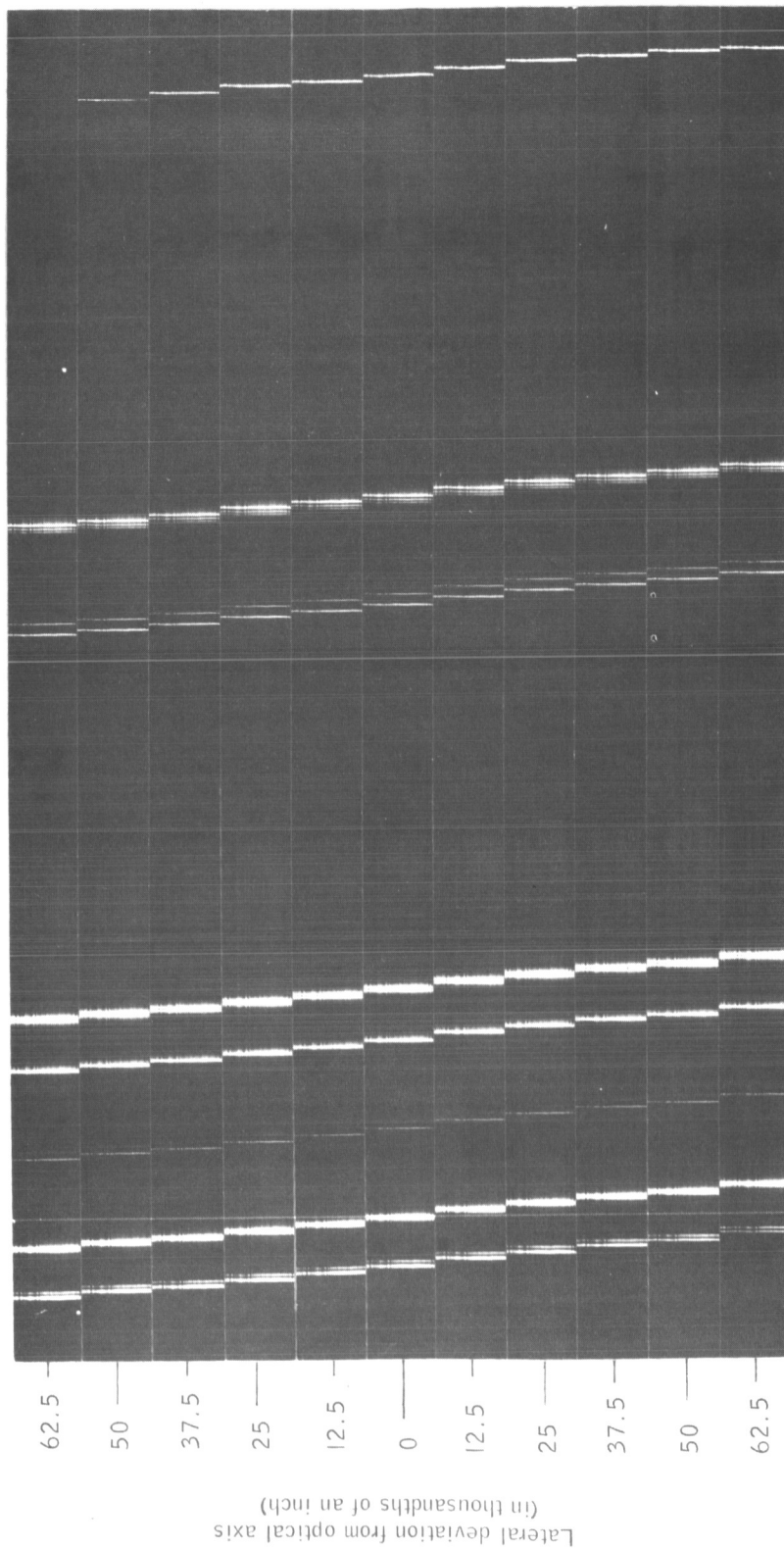
Figure 10e SIMULATION OF FIBER OPTICS MATRIX SLIT

Lateral deviation from optical axis
(in thousandths of an inch)

62.5 50 37.5 25 12.5 0 12.5 25 37.5 50 62.5

86-8244-1

-44-

7. 0 MICROMETEOROID SIMULATION EXPERIMENTS

7. 1 SIMULATION TECHNIQUE

The goal of these experiments has been to prove feasibility of the proposed technique of in situ analysis of micrometeoroid composition. Such proof has necessitated simulation of the parameters expected to be encountered by the final experiment in a space environment. This simulation is limited by present state-of-the-art restrictions imposed by the efficiency of launching techniques. These techniques are incapable of propelling a discrete particle of low enough mass at high enough velocity to approximate the micrometeoroid model. This is a difficulty unfortunately common to all laboratory approaches to the solution of problems involving the micrometeoroid hazard. The optimum approach is therefore to choose the simulation method capable of most closely approximating the desired conditions and to extrapolate the resultant data employing the best available physical and aerodynamic knowledge.

The light gas gun represents the only currently practical technique for launching a single particle of known mass and geometry at a hypervelocity. A . 22 caliber light gas gun (see Figure 1) was used for all of these experiments. Projectile particles, representing micrometeoroids, varied from 1/16-inch commercially produced glass spheres to irregularly shaped fragments of meteoritic origin with diameters down to a few thousandths of an inch. Sabots were used for all launches. Figure 11a shows an argon-filled balloon mounted in the ballistics impact tank prior to a shot. Figure 11b is a photograph of balloon damage after typical penetration of a 1/16-inch sphere at 22, 000 ft/sec. The balloon was pressurized with argon to 300 torr. A schematic of the vacuum tank instrumentation is presented in Figure 12.

7. 2 PROJECTILE PREPARATION

The spherical projectiles were employed in the previously discussed tests involving radiant flux measurement or comparison, since they provided a maximum consistency of geometry, mass, chemical composition and mechanical strength. These experiments included measurement of particle radiation during ablation in the test cell as a function of the independent variation of velocity and test cell gas pressure. Other experiments permitted the recording of radiant flux as a function of gas density at a constant absolute pressure, comparing the efficiency of argon and xenon. The same glass spheres were used to compare the relative optical efficiency and resolution of the spectrograph at varying apertures of the camera lens.

The meteoritic samples were quite difficult to launch due to their poor mechanical bond and overall lack of homogeneity. Experiments with these particles were therefore not only difficult to perform but also yielded unreproducable

COMMON GAS AND
VACUUM LINE

BALLISTICS
TRAJECTORY

FIBER OPTICS BUNDLES

MANOMETER LINE

RIGID MOUNT FOR POSITIONING
BALLOON TO TRAJECTORY
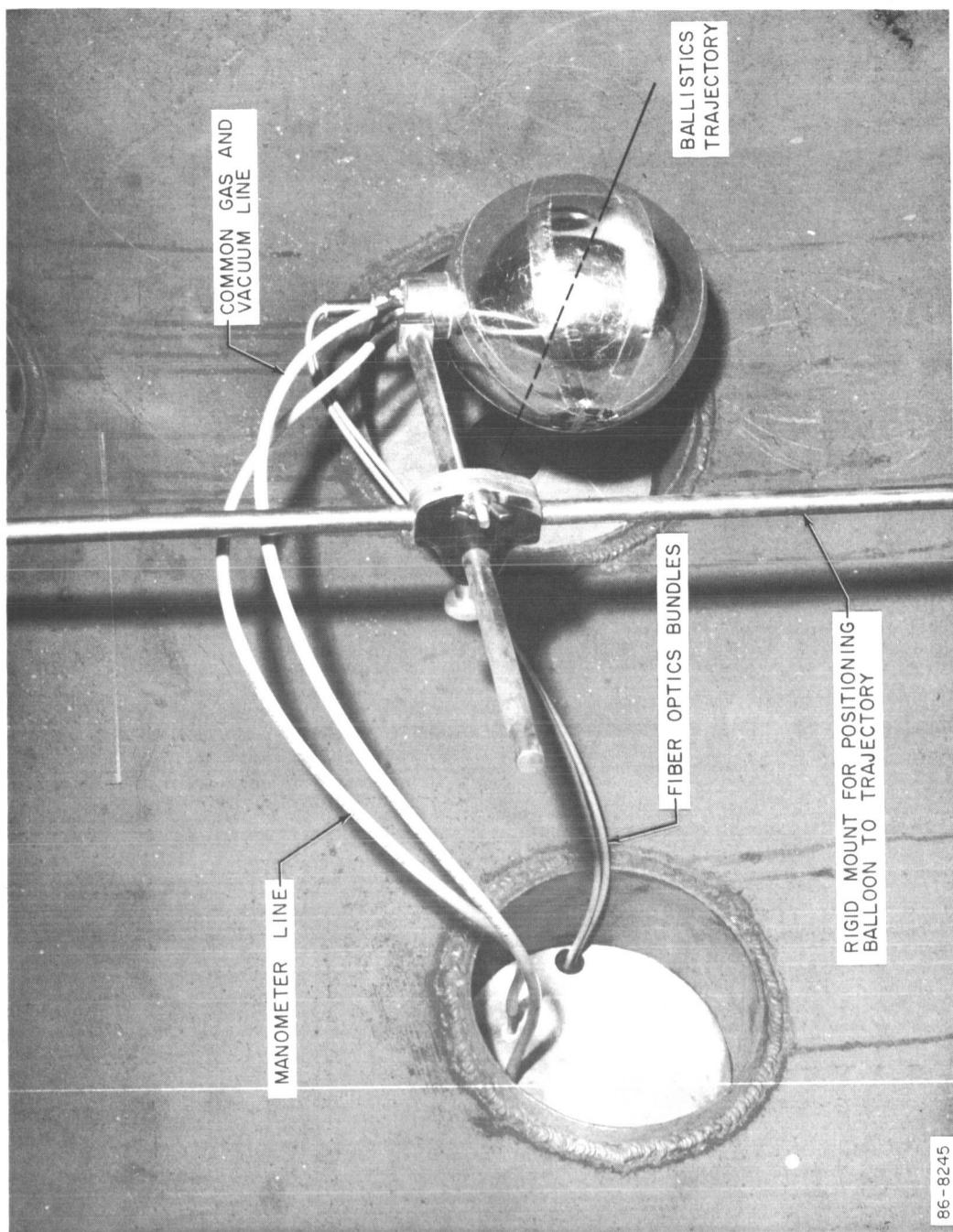
86-8245

Figure 11a PHOTOGRAPH OF BALLOON IN TARGET VACUUM TANK

PARTICLE EXIT PUNCTURE
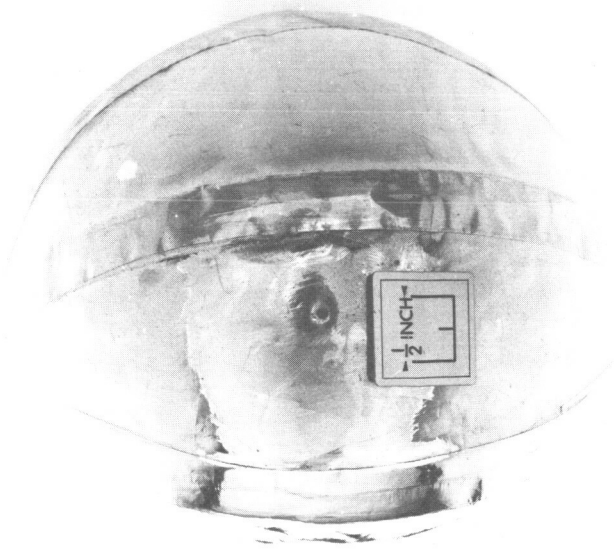
PARTICLE ENTRY PUNCTURE
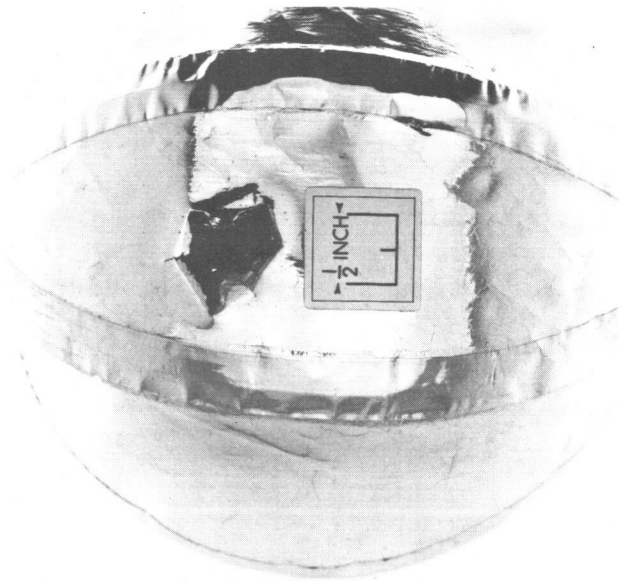
Figure 11b PHOTOGRAPH SHOWING BALLOON AFTER PENETRATION BY 1/16-INCH SPHERE

VALVES — TO GAS BOTTLES

VACUUM TANK

TO Hg MANOMETER

TO Hg CALIBRATION LAMP

FIBER
OPTICS

BREADBOARD
SPECTROGRAPH

BALLISTIC
TRAJECTORY

BALLOON
TEST CELL

EVACUATED

BALLISTICS RANGE
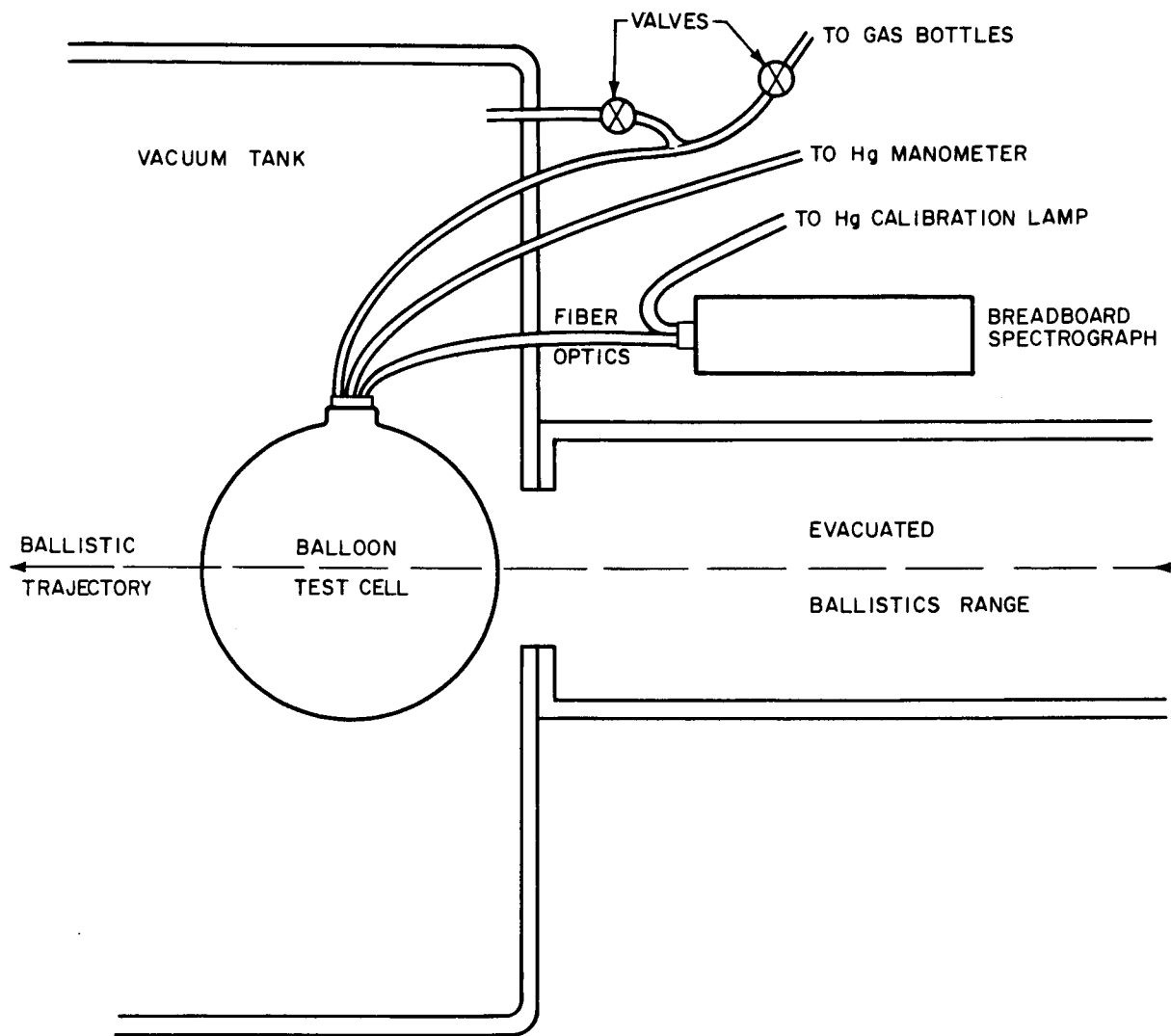
86-8247

Figure 12 SKETCH OF BALLOON INSTALLATION IN VACUUM TANK

-48-

radiant flux due to their tendency to fragment during and after launch. These factors confirmed earlier decisions to use commercially manufactured particles for the semi-quantitative comparative measurements. On the other hand, the use of actual meteoritic materials constitute the best possible simulation model in terms of proving the feasibility of analyzing the spectral "fingerprint" of micrometeoroids. Therefore, samples were procured of both Tektite and Siderolite meteorites as best representing the classical "stony" and "irony" type micrometeoroids. Representative samples of each were prepared for launch. The Tektite material proved to be quite homogeneous. When heated in a carbon crucible, small samples flowed into quite regular spherical shapes which were easily launched in the light gas gun. The Siderolite meteorite consisted of a honeycomb-like matrix of constituents having widely different melting points and poor mechanical bond. Efforts to fuse this material into a mechanically better form were unsuccessful, even when employing an induction furnace and an inert atmosphere. Mechanical techniques of grinding and coring produced several shapes which disintegrated at launch to fine powder. These extremely small dust-like particles decelerated to a velocity inadequate to either penetrate the balloons or to produce ablation temperatures in the test cells.

Finally a "shotgun" launch of several particles from this sample was successful. The parent sample was carefully cracked open and a number of fragments chosen for their apparent coherence. A good spectral record was obtained from this test. The exact mass and velocity of the several particles penetrating the test cell are not known.

A third meteoritic sample was procured by NASA/Manned Spacecraft Center personnel and prepared by them for light gas gun launch. This preparation consisted of coring several 1/16-inch diameter right cylinders. The composition of this sample was unknown to this laboratory, and its determination by use of the breadboard instrument system is one of the contractual requirements of this program. This material also evidenced poor strength and tended to violently disintegrate during launch. Two successful tests were made, however, and the resultant spectral data are analyzed in the following section of this report. One of these specimens was also vaporized in a carbon arc; the resultant spectral radiation was recorded by the breadboard spectrograph and is presented for comparison to the spectra recorded from the ballistic launched particles.

7.3 RESULTS OF THE SIMULATION EXPERIMENTS

The conclusive and critical phase of the feasibility program was the determination of composition of meteoritic particles by analysis of the spectrographic film records, many of which are given below. These recorded data are of radiation emitted during particle passage through the captive atmosphere of the balloon. Table III is an itemization of ballistics test data for those experiments whose results are illustrated in Figures 13 through 21. Particles included samples of an unknown meteorite supplied by NASA Manned Spacecraft Center,

TABLE III

BALLISTICS TEST DATA FOR REPRESENTATIVE METEOROID SIMULATION EXPERIMENTS

Test No.	Projectile Material	Test Cell Gas	Balloon Test Cell	Spectrograph Objective Lens F/No.	Velocity (ft/sec)	Test Cell Pressure (Torr)
49	Pyrex	Argon	No	1.5	22,900	760
59	Tektite Meteorite	Argon	Yes	1.5	22,800	300
60	Siderolite Meteorite	Argon	Yes	1.5	Approx. 22,000	300
61	Soda Lime Glass	Argon	Yes	1.5	21,500	300
62	NASA/MSC Meteorite	Argon	Yes	1.5	21,900	300
64	NASA/MSC Meteorite	Argon	Yes	1.5	22,500	300
68	Soda Lime Glass	Xenon	Yes	1.5	Approx. 22,000	300
70	Soda Lime Glass	Xenon	Yes	4	24,000	300
71	Soda Lime Glass	Argon	Yes	1.5	Approx. 22,000	20

and samples of the classical "stony" (Tektite) and "irony" (Siderolite) meteorites. In order to extend the sample variety, commercially produced spheres of soda lime and borosilicate (Pyrex) glass were also launched and the resultant spectra recorded. The composition of these materials is similar to that expected in some of the "stony" types of meteoroids.

Let us recall the expected spectral content of typical meteors, and also the test particles, to aid in judging whether meaningful signatures were achieved. All meteor spectra seem to consist of bright lines formed chiefly by the low excitation lines of common elements. In rare instances some molecular bands (e. g. FeO) appear, but their rarity causes them to be ignored in this study. Certain identification in various meteors of the following atoms has been made: (I refers to the neutral atom, II to singly ionized atoms):

Fe I and II, Na I, Ca I and II, Mg I and II,

Mn I, Cr I, Si I and II, Ni I and Al I, H I,

N I, and O I.

The ionized atoms seem to be absent from spectra of meteors with velocities less than about 30 km/sec[20]. The above list is not all inclusive, but typical.

In the "stony" meteorite, the alkaline earths (Ca, Mg) spectra seem to prevail, while in the "irony" type the iron spectrum dominates; however, these are not mutually exclusive. The compositions of the test particles (soda lime glass, Pyrex) are given in Table IV below:

TABLE IV

COMPOSITION OF SODA LIME AND BOROSILICATE GLASSES

	Typical Soda Lime Glass	Typical Borosilicate (Pyrex)
SiO_2	72 percent	80 percent
Na_2O	15 percent	4 percent
CaO	9 percent	-
MgO	3 percent	-
Al_2O_3	1 percent	2 percent
B_2O_3	-	14 percent

Figure 13 shows typical spectra of five different materials, recorded under various conditions. These spectra are displayed and discussed individually later, with more detail. In this figure several points should be noted: the first order covers about 4050 to 6910A, the second order about 4000 to 5500 A. This second-order range limitation is due to mechanical cutoff of the frame size adopted. In Figure 13, in all but the bottom (Pyrex) spectrum, the vertical variation in intensity is due to use of a continuous neutral density wedge covering a total density range of 0 to 1.5. The Pyrex spectrum was taken with a simple fiber-ribbon slit (i.e., the field of view was defined by a vertical stack of fibers the same geometry as the slit), while all the other spectra were taken with the final cylinder-to-slit fiber optics system discussed earlier.

Figures 13b and 13c show the close similarity, as expected, in spectra of the Tektite or "stony" meteor type and the soda lime glass. (See also Figure 15 and Figure 16a presented later).

Figure 14 shows again the Pyrex particle spectrum, with the major line multiplets due mostly to Na and Ca. Noteworthy here is, despite the presence of some weak Na I lines and also Ca II, the absence of AlO and BO (or B_2O_3) band spectra. There is also a continum background. The Li line is treated later.

Before further data presentation, the analysis of the spectra should be described. The accompanying analyses are derived from microcomparator measurements of the original photographic negatives. It is to be noted that the previously discussed first order resolution of 7-10 A is probably conservative in view of the measurement discrimination possible with these films. It should be kept in mind that all the spectra displayed have been degraded of necessity in the reproduction process. No spectral assignments have been made unless obvious lines were present in the original photographic negative records.

The accuracy of the species identification resultant from these measurements is crucial to final proof of feasibility of this entire experimental concept. To augment extensive analyses and consequent judgments, independent and objective consultation was sought. Such help was obtained from Dr. Peter Millman, who is well known for his pioneering work in the field of meteor physics at the Dominion Observatory and the Canadian National Research Council. Dr. Millman has devoted many years to identification and cataloging of meteor and, more recently, reentry spectra. He very kindly consented to spend a few days in analysis of spectra from the three types of meteoritic samples. Due to the limited time available, Dr. Millman worked with the metric film measurements made by this laboratory. Should any errors exist in the following species identification, it may be assumed that they result from these measurements.
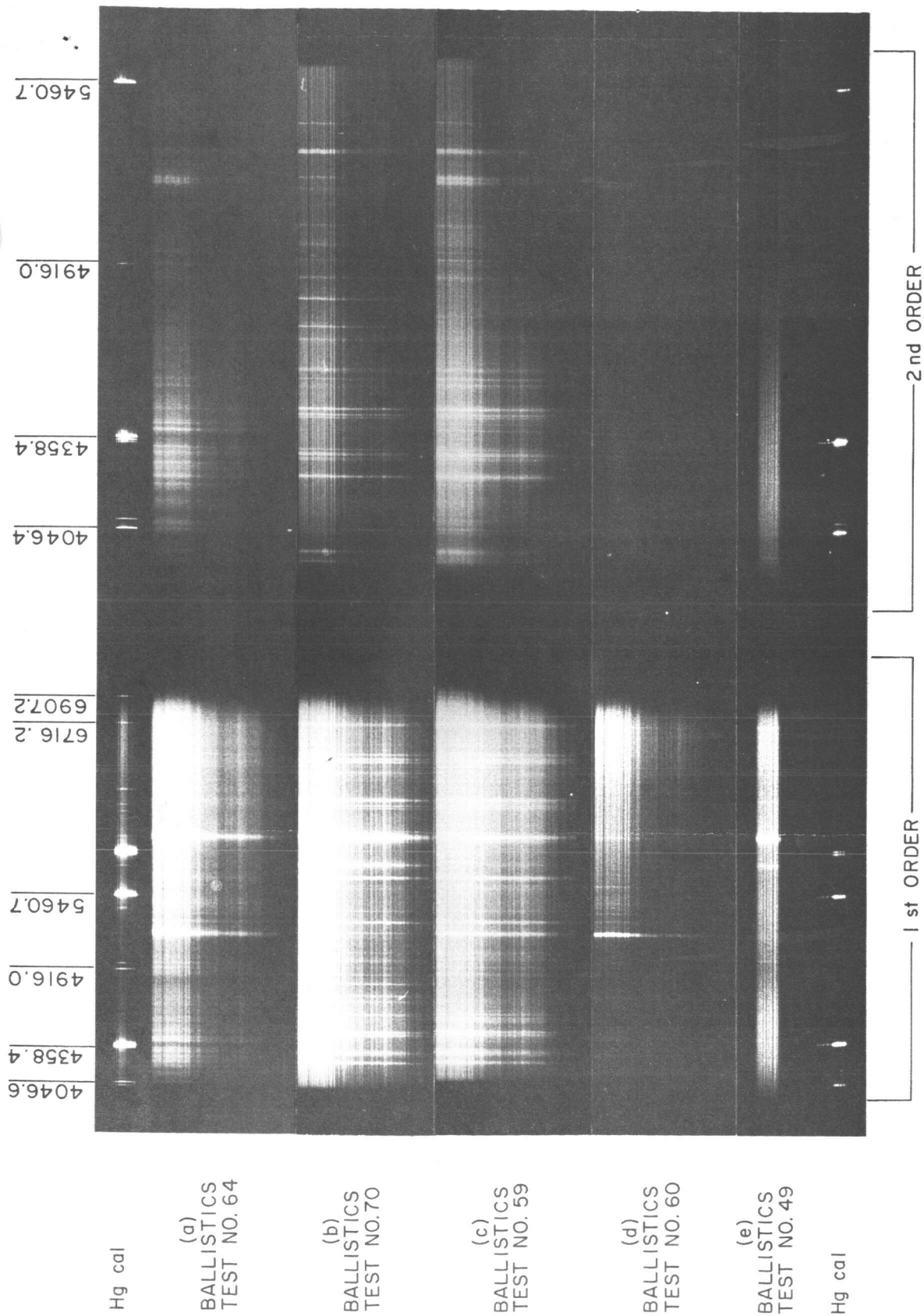
Figure 13 TYPICAL SPECTRA FROM ABLATION OF FIVE DIFFERENT MATERIALS

(a) NASA METEORITE IN ARGON
(b) SODA LIME GLASS IN XENON
(c) TEKTITE METEORITE (ORIGIN BOHEMIA) IN ARGON
(d) SIDEROLITE METEORITE (ORIGIN KANSAS) IN ARGON
(e) PYREX IN ARGON

Hg cal

(a)
BALLISTICS
TEST NO. 64

(b)
BALLISTICS
TEST NO.70

(c)
BALLISTICS
TEST NO. 59

(d)
BALLISTICS
TEST NO. 60

(e)
BALLISTICS
TEST NO. 49

Hg cal

86-8248

-53-
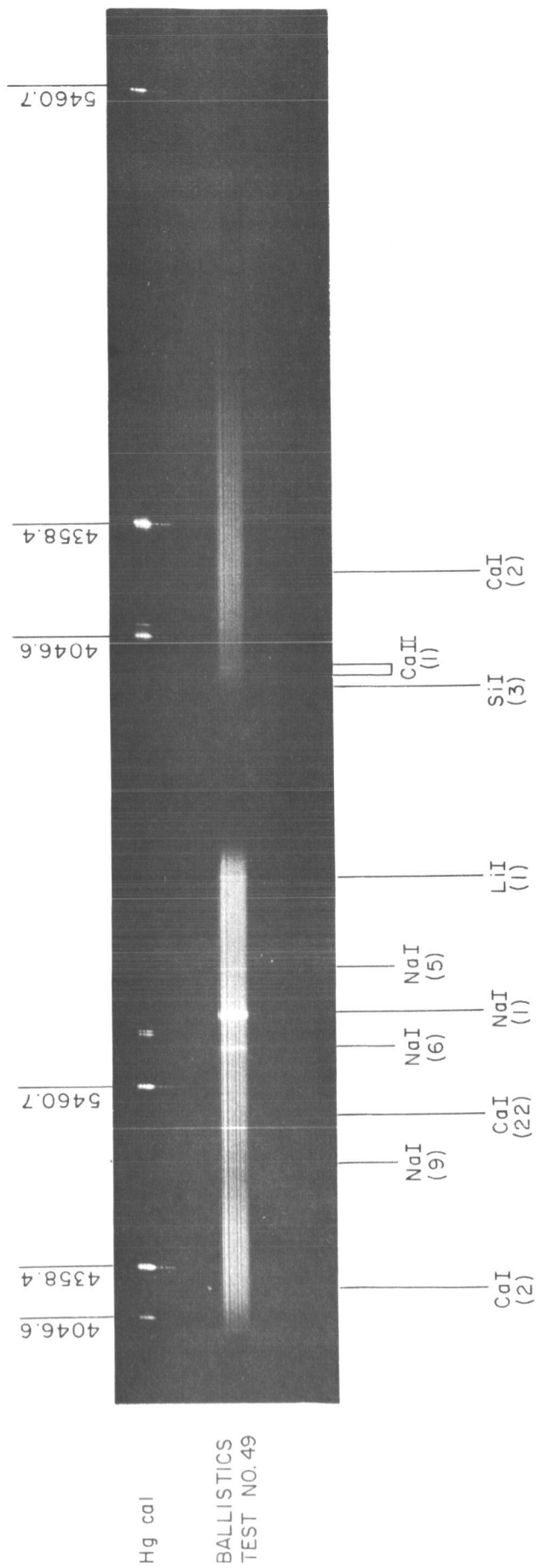
Figure 14 IDENTIFICATION OF THE MAJOR MULTIPLETS OF A PYREX PARTICLE

86-8249

-54-

Following his usual method of treatment of meteor spectra, Dr. Millman grouped and identified the lines in multiplets according to Charlotte E. Moore's A Multiplet Table of Astrophysical Interest.[21] Such multiplets found in our spectra are given in Tables V and VI which follow. The Li line at 6707 A deserves special note. Millman pointed out to use that this is the only line which shows in many of our laboratory "meteor" spectra, but has not been found yet in any true meteor spectrum.

Figure 15 displays the spectra of soda lime glass with more complete identification of the many multiplets of Ca I and II observed. This figure also shows the reproducibility of the spectra obtainable. An additional point is the apparent but certainly not serious degradation of data quality in increase of the optical aperture from F/4 to F/1.5.

Figure 16 gives spectra and detailed identification of the Tektite and Siderolite meteoritic particles. The Tektite spectrum is rich in the alkaline earth lines. Recall the Tektite-soda lime glass comparison of Figures 13b and 13c. Figure 16b, from the Siderolite "meteor" shot shows, in addition to the expected Fe spectrum, the presence of a strong Mg I multiplet at 5170 A.

Figures 17 and 19 are of major interest in this program in that they present spectra from a meteorite of unspecified composition and origin, supplied by NASA/Manned Spacecraft Center. Figure 17 compares the results of two ballistics tests and that from a conventional analytical type carbon arc. All were taken with the same breadboard spectrograph system with Fiber optics input. Figure 18 repeats the spectra with the identification of many lines given; many more have been identified but have not been labeled. The complete tabulation of all of these measured wavelengths is given in Table V.

These spectra show unequivocably that the NASA/MSC sample meteorite is of the iron type. Appendix A of this report presents a detailed analysis of an approach for semiquantitative evaluation of discrimination between the "iron" and "stony" types of meteoroids. Table V lists the wavelengths of the identified lines* in the included spectra (Figures 13 through 17).

TABLE V

A TABULATION OF LINES IDENTIFIED IN THE INDUCED SPECTRA

Li I (1)	Na I (5)	Na I (9)
6707.7	6160.7	4982.8
6707.9	6154.2	4978.5
Na I (1)	Na I (6)	Mg I (2)
5890.0	5688.2	5183.6
5895.9	5682.6	5172.7
		5167.3

*The lines, given in Angstrom units, are grouped according to multiplets within a given element. Charlotte E. Moore's "A Multiplet Table of Astrophysical Interest" was used as a reference. In the following tabulation, the elements are arranged in order of increasing atomic number. For each element, the multiplets are numbered (in parenthesis) as given in the Multiplet tables. The lines within a given multiplet are, in general, in order of decreasing intensity as suggested by the above-mentioned reference.

TABLE V (Cont'd)

Mg I (9)	Ca I (21)	Cr I (7)
5528.4	5588.8	5208.4
	5594.5	5206.0
Mg I (11)	5598.5	5204.5
4703.0	5601.3	
	5602.8	Mn I (2)
Mg I (15)	5582.0	4030.8
4167.3	5590.1	4033.1
		4034.5
Si I (3)	Ca I (22)	
3905.5	5270.3	Fe I (1)
	5265.6	5110.4
Ca I (2)	5262.2	5168.9
4226.7	5264.2	5166.3
	5261.7	5204.6
Ca I (3)		5225.5
6162.2	Ca I (23)	5247.0
6122.2	4585.9	5250.2
6102.7	4581.4	5255.0
	4578.6	
Ca I (4)		Fe I (2)
4454.8	Ca I (33)	4427.3
4435.0	5349.5	4375.9
4425.4		4461.7
4455.9	Ca I (34)	4482.2
4435.7	5041.6	4489.7
4456.6		4389.2
	Ca I (35)	4435.2
Ca I (5)	4878.1	4466.6
4302.5		
4299.0	Ca I (49)	Fe I (3)
4318.6	5188.8	4216.2
4307.7		4291.5
4283.0	Ca II (1)	4206.7
4289.4	3933.7	4258.3
	3968.5	4200.0
Ca I (18)		
6439.1	Cr I (1)	Fe I (4)
6462.6	4254.3	3859.9
6493.8	4274.8	3878.6
6471.7	4289.7	3824.4
6499.6		3856.4
		3886.3
		3899.7
		3927.9

TABLE V (Cont'd)

Fe I (15)	Fe I (41)	Fe I (71)
5269.5	4383.5	4282.4
5328.0	4404.8	4315.1
5371.5	4415.1	4352.7
5397.1	4294.1	
5405.8	4337.0	Fe I (111)
5429.7	4291.5	6421.4
5446.9	4367.9	6945.2
5455.6		6750.2
5434.5	Fe I (42)	6978.9
5506.8	4271.8	6663.4
5497.5	4307.9	
5501.5	4325.8	Fe I (152)
	4202.0	4260.5
Fe I (16)	4250.8	4250.1
5012.1	4147.7	4235.9
5051.6		4187.0
4994.1	Fe I (43)	4187.8
5083.3	4045.8	4198.3
5041.1	4063.6	4271.2
5107.5	4071.7	4299.2
5123.7	3969 3	4233.6
5142.9	4143.9	4210.4
5150.8	4005.2	4191.4
5127.4	4132.1	4222.2
4939.7		
5079.7	Fe I (62)	Fe I (168)
5151.9	6430.9	6495.0
	6335.3	6393.6
Fe I (37)	6265.1	6593.9
5167.5	6219.3	6462.7
5227.2		6318.0
5270.4	Fe I (68)	
5341.0	4528.6	Fe I (169)
5328.5	4494.6	6252.6
	4442.3	6191.6
Fe I (39)	4459.1	6136.6
4602.9	4447.7	
4531.2	4408.4	Fe I (207)
4654.5	4430.6	6230.7
4592.7	4482.2	6137.7
4632.9	4407.7	6065.5
		6322.7
		6200.3

TABLE V (Cont'd)

Fe I (268)	Fe I (409)	Fe I (816)
6678.0	4647.4	6400.0
6592.9	4691.4	6411.7
6546.2	4710.3	6408.0
6806.9		6246.3
6703.6	Fe I (467)	6301.5
	4786.8	6336.8
Fe I (318)	4772.8	
4957.6		Fe I (821)
4920.5	Fe I (554)	4678.9
4891.5	4736.8	4654.6
4871.3	4707.3	4705.0
4919.0	4668.1	4669.2
4890.8	4654.6	4745.8
5006.1	4637.5	4727.4
4957.3	4625.0	4619.3
4872.1	4607.7	
4859.7	4613.2	Fe I (1062)
4878.2		5476.6
4903.3	Fe I (686)	5563.6
4938.8	5615.7	5473.9
4985.6	5586.8	5478.5
	5572.8	
Fe I (350)	5569.6	Fe I (1066)
4466.6	5576.1	4983.9
4476.0	5709.4	4989.0
4443.2	5658.8	
4422.6	5624.5	Fe I (1107)
4454.4	5603.0	5763.0
		5753.1
Fe I (354)	Fe I (687)	5655.5
4181.8	4966.1	
4156.8	4946.4	Fe I (1146)
4107.5	5002.8	5424.1
4175.6		5383.4
	Fe I (693)	5370.0
Fe I (383)	4227.4	5367.5
5232.9	4247.4	5364.9
5192.4	4238.8	
5139.5	4217.6	Fe I (1165)
5191.5	4225.5	5415.2
5226.9		5404.1
5281.8		5410.9
5139.3		
5068.8		

TABLE V (Concl'd)

Fe I (1175)
5983.7

Fe I (1178)
6024.1
6020.2
6008.0
5852.2

Fe I (1180)
5862.4
5914.2
5930.2

Fe I (1253)
6569.2
6597.6
6495.8

Fe I (1258)
6420.0
6496.5
6469.2

Fe I (1260)
5984.8
5987.1
5975.4
6170.5
6103.2

Ba I (2)
5535.5

Ba II (1)
4554.0
4934.1

Figure 15 IDENTIFICATION OF THE MAJOR MULTIPLETS OF SODA LIME GLASS PARTICLES AND COMPARISON OF RESOLUTION AS A FUNCTION OF OPTICAL APERTURE
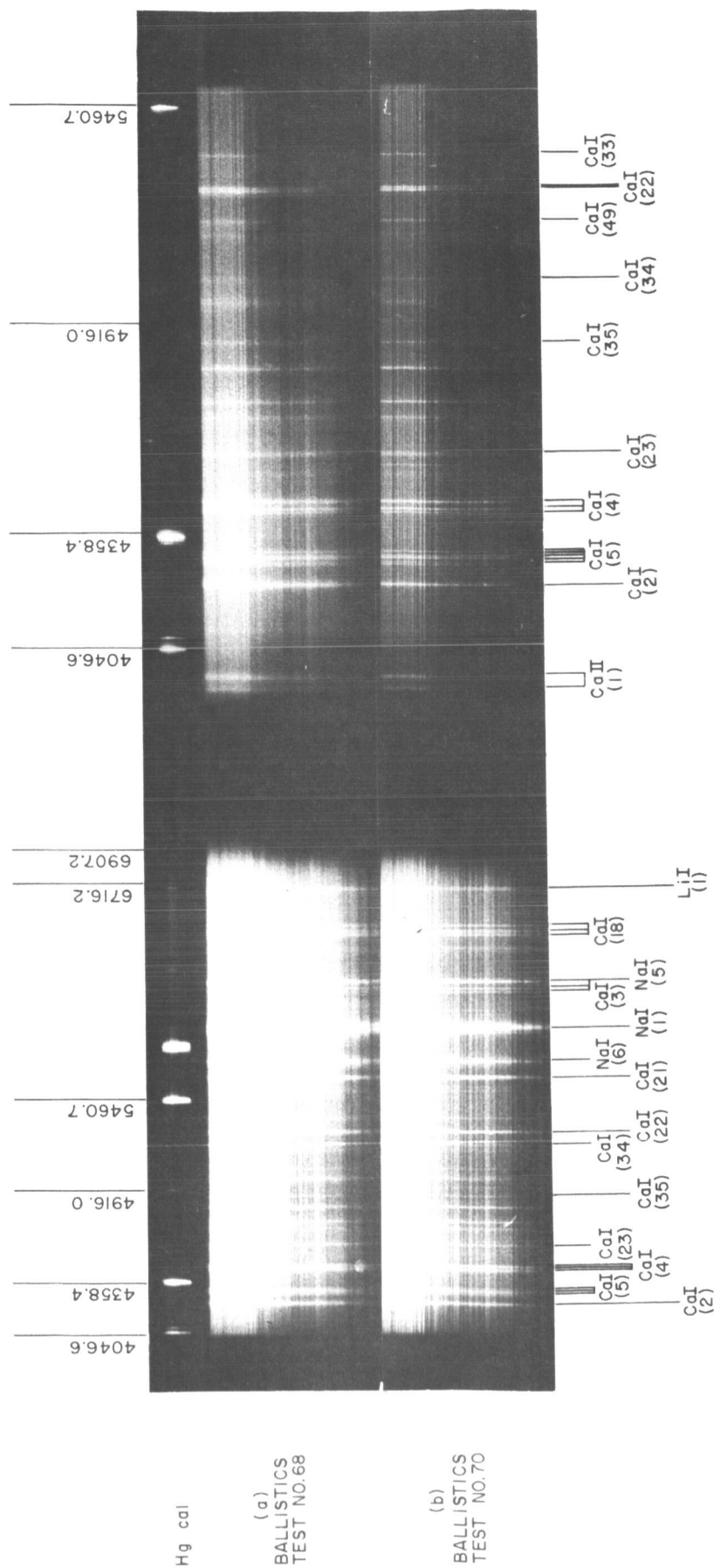
86-8250
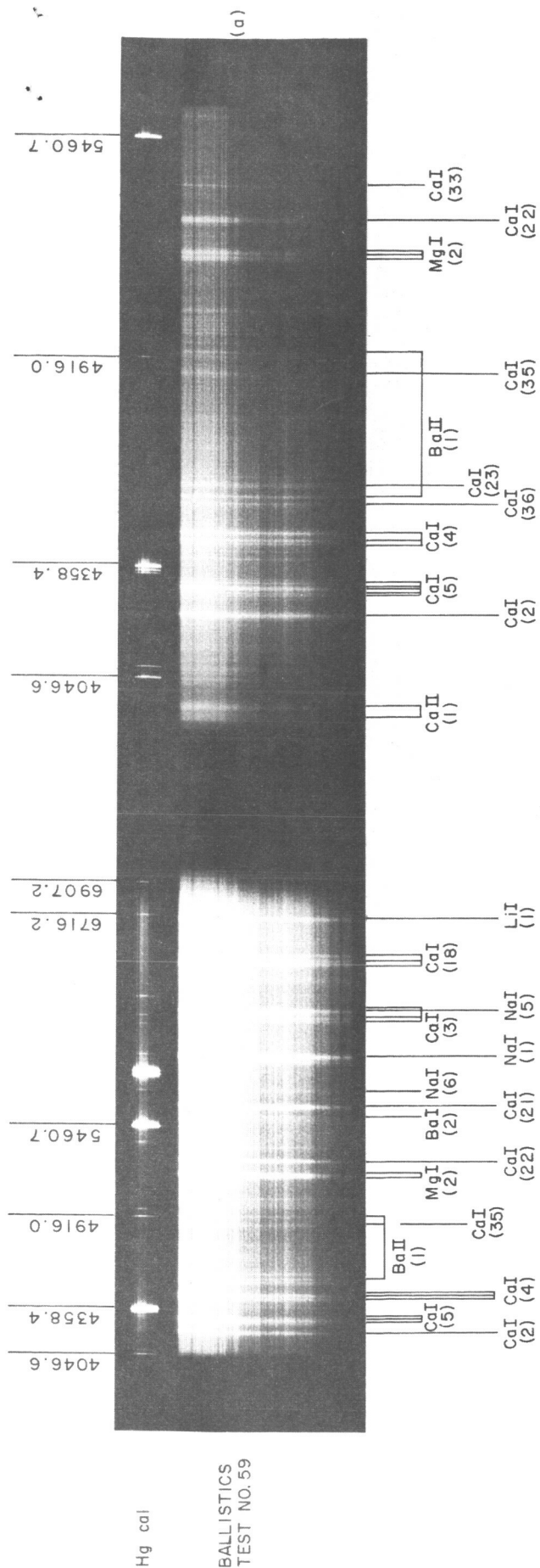
Figure 16a IDENTIFICATION OF THE MAJOR MULTIPLETS OF A METEORITIC
PARTICLE, VARIETY TEKTITE
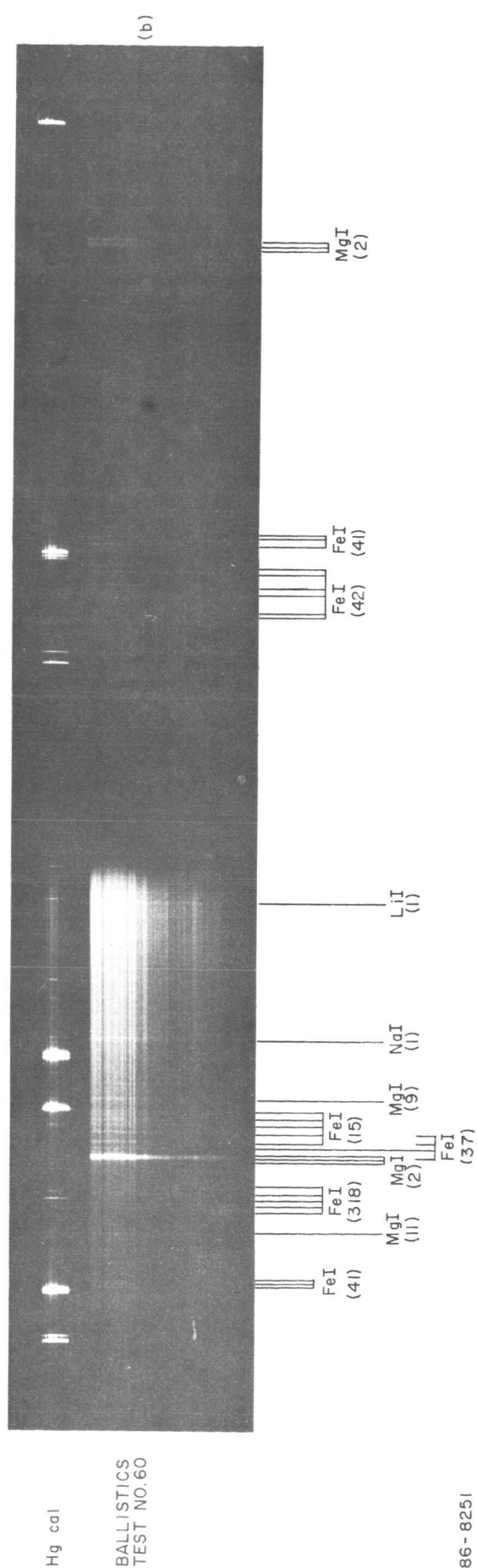
Figure 16b IDENTIFICATION OF THE MAJOR MULTIPLETS OF A METEORITIC
PARTICLE, VARIETY SIDEROLITE

86 - 8251

-61-

SPECTROGRAPH APERTURE | BALLOON PRESSURE | BALLOON GAS | PARTICLE VELOCITY
(a) F/4

(a) CARBON ARC SOURCE
(b) BALLISTICS TEST NO. 64
(c) BALLISTICS TEST NO. 62
Hg cal

5460.7 4916.0 4358.4 4046.6 6907.2 6716.2 5460.7 4916.0 4358.4 4046.6
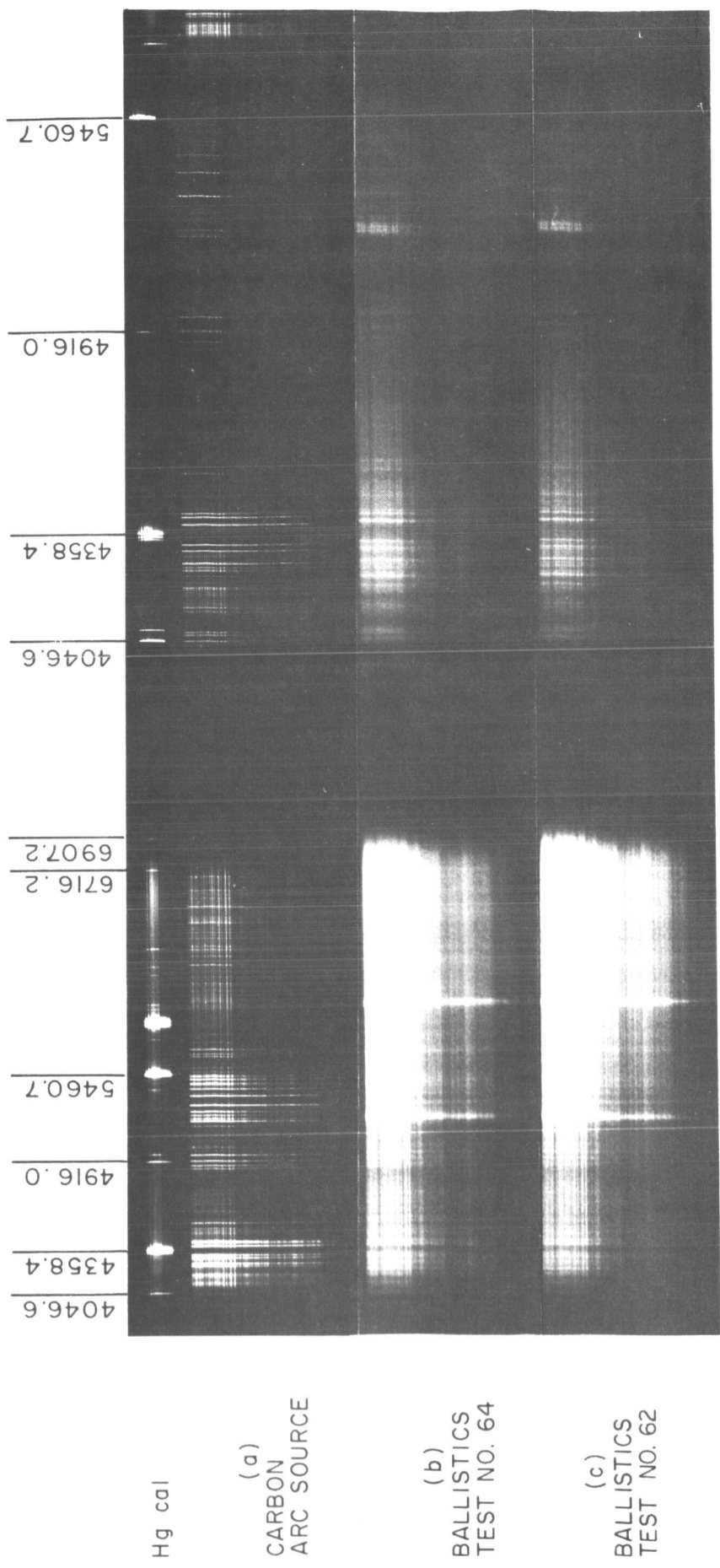
SPECTROGRAPH APERTURE	BALLOON PRESSURE	BALLOON GAS	PARTICLE VELOCITY
(a) F/4		AIR	
(b) F/1.5	300 torr	ARGON	22,500 ft/sec
(c) F/1.5	300 torr	ARGON	21,900 ft/sec

Figure 17 COMPARISON OF SPECTRA FROM THREE SAMPLES TAKEN FROM A
METEORITE OF UNKNOWN ORIGIN AND COMPOSITION SUPPLIED
BY NASA/MANNED SPACECRAFT CENTER

86-8252

-62-

Figure 18 IDENTIFICATION OF THE MAJOR MULTIPLETS OF METEORITE OF UNKNOWN ORIGIN AND COMPOSITION SUPPLIED BY NASA/MANNED SPACECRAFT CENTER
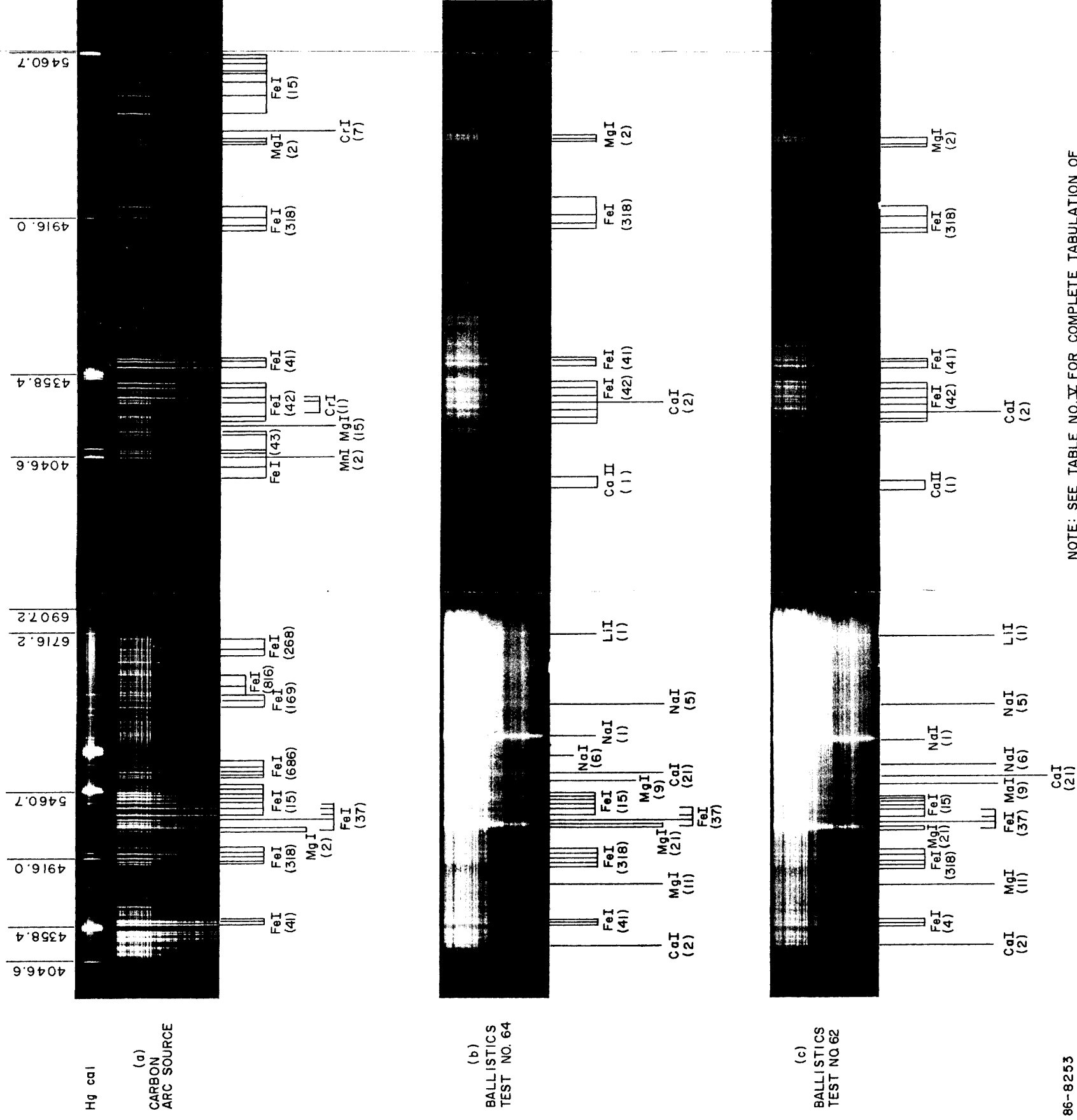
NOTE: SEE TABLE NO. X FOR COMPLETE TABULATION OF MEASURED WAVELENGTHS

86-8253

Three different spectra from the NASA/MSC meteorite are shown in Figure 17. Due to inadequate space on this illustration to list all multiplets, only the more prominent ones are included. All iron lines listed in Table V have been identified in spectra from all three experiments.

Therefore, Table VI below lists only those multiplets which are not common to all three tests. The breadboard spectrograph and Kodak I-F film were used for for all three. The first employed a laboratory carbon arc as source for sample vaporization; the other samples were light gas gun launched through argon-filled Mylar balloons at a velocity of 22, 500 ft/sec for test No. 64 and 21, 900 ft/sec for test No. 62. It is not known whether the differences shown below are resultant from varying excitation levels or from sample-to-sample variation within the meteorite or a combination of both factors. Similarities of the two ballistics tests suggest the former conclusion.

<u>TABLE VI</u>

COMPARISON OF MULTIPLETS IDENTIFIED IN SPECTRA
FROM THE NASA/MSC METEORITE IN THREE TESTS

Carbon Arc Source	Ballistics Test No. 64	Ballistics Test No. 62
	Li I (1)	Li I (1)
	Na I (1)	Na I (1)
	Na I (5)	Na I (5)
	Na I (6)	Na I (6)
	Mg I (9)	Mg I (9)
	Mg I (11)	Mg I (11)
Mg I (15)		
	Ca I (2)	Ca I (2)
	Ca I (21)	Ca I (21)
	Ca II (1)	Ca II (1)
Cr I (1)		
Cr I (7)		
Mn I (2)		

A majority of the ballistic simulation tests employed an argon atmosphere. Due to its higher molecular weight, xenon was used in some experiments in order to compare its relative efficiency of particle excitation and also to explore the possible spectral background contribution due its emission as a result of the high thermal shock. No such background contribution was found in any tests with either xenon or argon. The radiation levels produced using xenon were consistently and appreciably higher than those resultant from similar tests using argon with all other parameters held constant. A typical illustration of this comparison is shown in Figures 19a and 19b. (Note that the difference is even greater than graphically presented, due to the factor of 2 decrease in the test cell pressure of the xenon shot.) A quantitative evaluation of this relationship has not been made due to the relatively small number of tests employing xenon and the large variation in shot-to-shot radiation levels discussed in the earlier section on Laboratory Experiments. Such evaluation could be made by correlation of microdensitometry of the film data with the known attenuation of the entrance slit wedge and the D/log E response curve of the film. It is felt that the indicated experimental data spread, resultant from nonreproducible particle fragmentation and radiation level, makes such measurement misleading unless based upon a large number of tests designed around this single problem.

A similar statement may be made in reference to the gain of collection efficiency by the reflectivity of the spherical test cell. Figures 20a and 20b indicate the obvious gain realized in employment of the aluminized balloon in comparison to a similar shot using the identical spectrograph system but looking into the modified range section having a very minimal surface reflectivity. The same restraints of experimental reproducibility limit the meaningfulness of quantitative measure of this comparison. Static (nonballistic) laboratory testing will be employed to measure the reflection efficiency of advanced design balloon surfaces. Schjeldahl has provided a number of Mylar samples with various specular and diffuse reflecting surfaces which promise a relatively high gain, but this materials development must be coordinated with other balloon design problems such as mechanical fabrication techniques discussed earlier.

Figure 21 is a typical spectrum of particle radiation at a balloon pressure of 20 torr, the lowest pressure used in these tests.

Figure 22 is a photograph illustrating typical projectile fragmentation and ablation after penetrating a 1-mil Mylar membrane into an argon atmosphere.
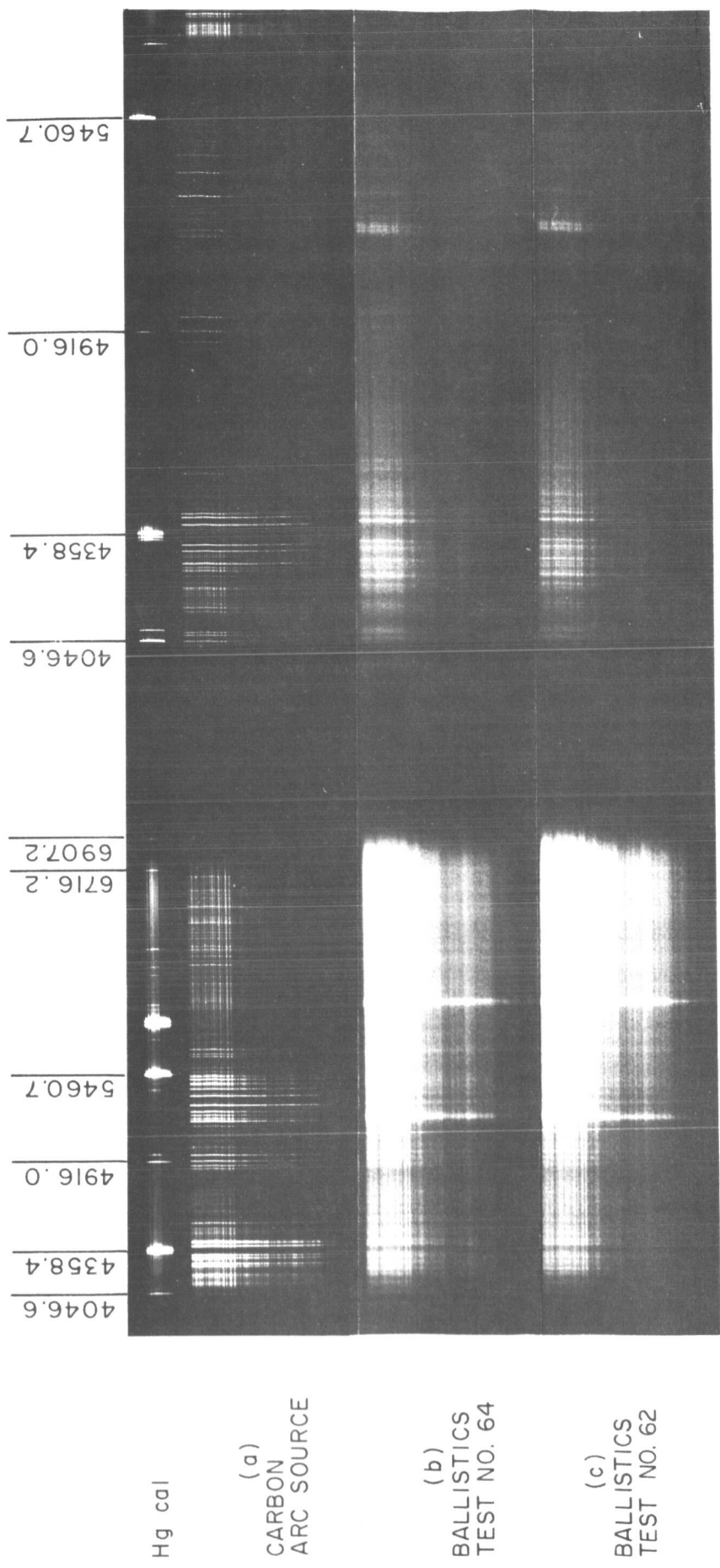
Figure 17 COMPARISON OF SPECTRA FROM THREE SAMPLES TAKEN FROM A
METEORITE OF UNKNOWN ORIGIN AND COMPOSITION SUPPLIED
BY NASA/MANNED SPACECRAFT CENTER

SPECTROGRAPH APERTURE	BALLOON PRESSURE	BALLOON GAS	PARTICLE VELOCITY
(a) F/4			
(b) F/1.5	300 torr	ARGON	22,500 ft/sec
(c) F/1.5	300 torr	ARGON	21,900 ft/sec
		AIR	

Hg cal

(a)
CARBON
ARC SOURCE

(b)
BALLISTICS
TEST NO. 64

(c)
BALLISTICS
TEST NO. 62

86-8252

Hg cal

TEST

5460.7Å

4916.0Å

4358.4Å

4046.6Å

2 nd ORDER

1st ORDER

SHOT NO: 59
VELOCITY: 22,790 ft/sec
TEST CELL ATMOSPHERE: ARGON, 350 torr

A: SPECTRUM FROM "TEKTITE" METEORITIC SAMPLE LAUNCHED THROUGH
BALLOON TEST

Hg cal

TEST

5460.7Å

4916.0Å

4358.4Å

4046.6Å

2 nd ORDER

1st ORDER

SHOT NO: 52
VELOCITY: 22,680 ft/sec
TEST CELL ATMOSPHERE: ARGON, 760 torr

B: SPECTRUM FROM "TEKTITE" METEORITIC SAMPLE LAUNCHED THROUGH
NONREFLECTING BALLISTICS RANGE TEST CELL
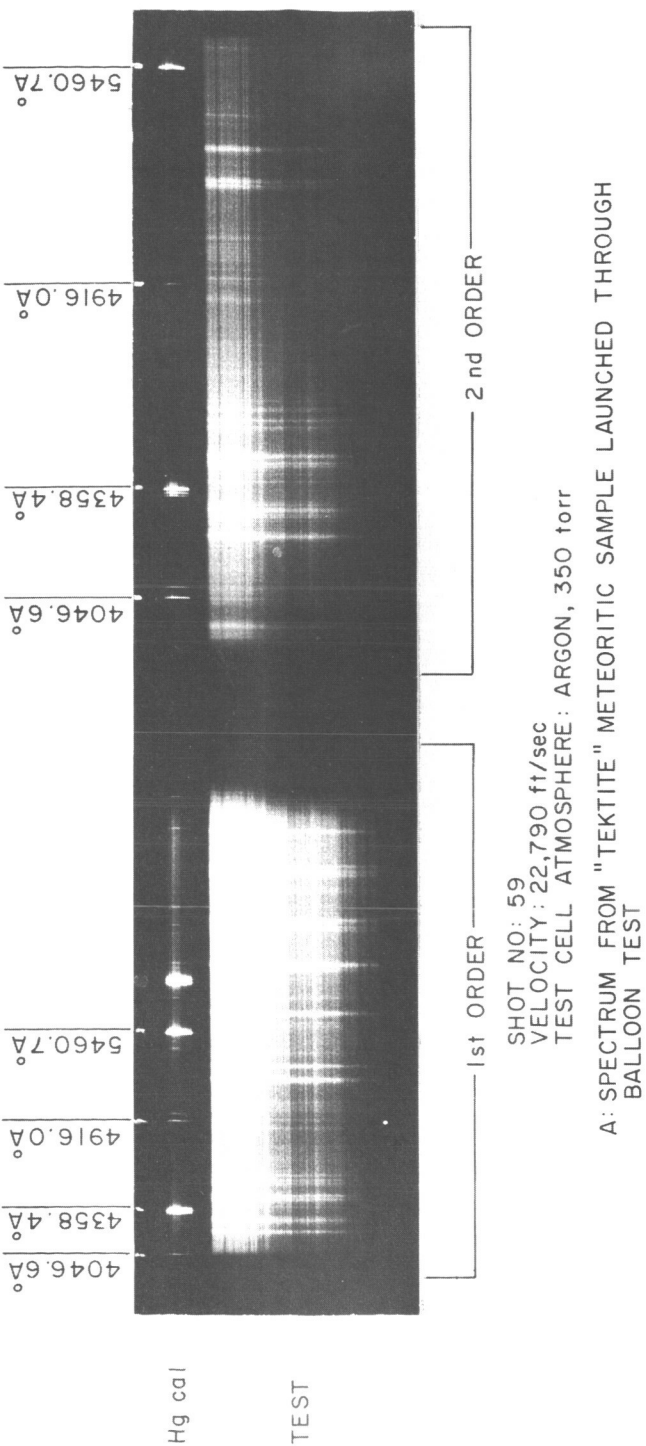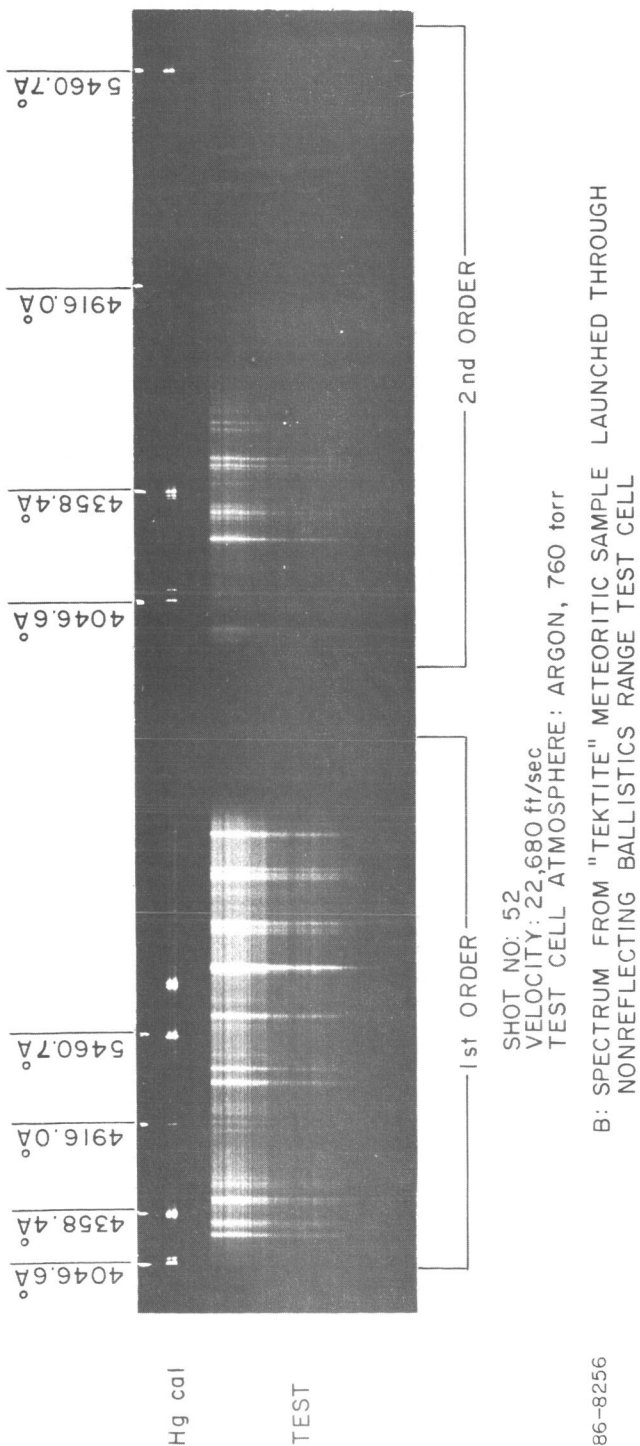
Figure 20 A COMPARISON OF SPECTROGRAPH SYSTEM EFFICIENCY GAIN BY USE
OF A REFLECTING BALLOON AS TEST CELL
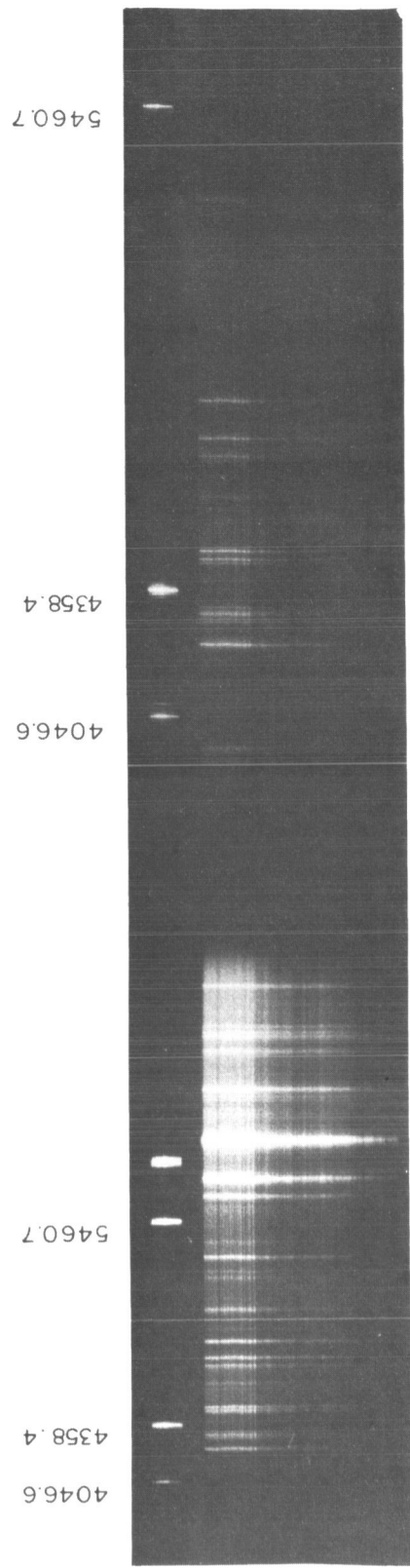
86-8256

Figure 21 SPECTRUM FROM 1/16-INCH SODA LIME GLASS SPHERE AT BALLOON
TEST CELL PRESSURE OF 20 TORR (XENON)

5460.7

4358.4

4046.6

5460.7

4358.4

4046.6

Hg cal

BALLISTICS
TEST NO.71

86-8255
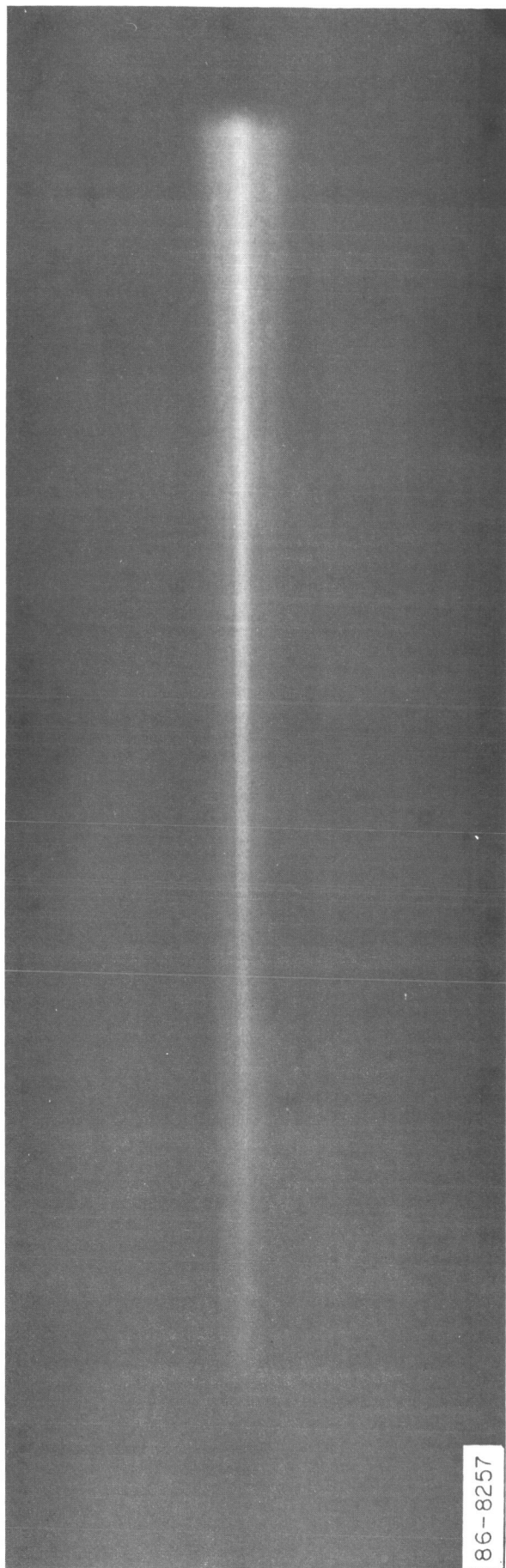
Figure 22 PHOTOGRAPH OF 1/16-INCH PYREX SPHERICAL PROJECTILE PASSING THROUGH 50-TORR ARGON ATMOSPHERE, VELOCITY: 23,700 FT/SEC

86-8257

8.0 PROTOTYPE FLIGHT INSTRUMENT DESIGN

8.1 INTRODUCTION

The following conceptual design for a flight instrument system package is based
directly upon results of the laboratory experimentation and analytical studies
conducted under this feasibility contract. In order to illustrate a typical adapta-
tion of this experiment to a specific vehicle and mission, consideration has been
given to deployment during earth orbit of the Apollo laboratory, launched by the
two-stage Saturn SIIIB-SIVB configuration. It has been assumed that the orbit
may be anywhere within the 100 to 400-nautical mile design range of the two-
stage Apollo launch vehicle. Evaluation of possible thermal control problems
has considered the total spectrum from the best to the worst conditions to be
encountered by the experiment as a result of favorable or unfavorable vehicle
attitude orientation relative to the earth and sun. The experiment permits either
simple retrieval of the recorded data by an astronaut during rendezvous or the
storage and telemetry of the information to an earth-based station.

It is to be strongly emphasized that neither this analyzer concept nor this basic
engineering approach is limited to or restrained by either the Saturn vehicle or
an earth orbital mission. This study has been devoted to consideration of the
problems inherent in application of this experimental approach to any environ-
ment outside the earth's atmosphere.

An artist's sketch of the meteoroid analyzer is shown in Figure 23. This sketch
and the functional block diagram shown in Figure 24 represent the present con-
ceptual design. An engineering design and prototype development will require
additional effort to optimize the design for a specific mission including the pack-
aging, deployment, launch and space environment, etc. associated with the
experiment.

This section will describe the sequential operation of the flight instrument at and
following deployment. Finally, a description of the major components of the
system giving specifications and the present state of development will be given.

8.2 SEQUENTIAL OUTLINE OF FLIGHT INSTRUMENT OPERATION

The following outline is referenced to the block diagram of the instrument sys-
tem as shown in Figure 24.

8.2.1 Deployment and System Activation

Deployment is programmed to take place after vehicle stabilization in orbit. A
single electrical signal releases and ejects a port cover on the vehicle skin,
exposing a cannister containing the packaged balloons and their individual um-
bilicals. The same signal opens a single, normally closed gas valve between

(a)

(b)
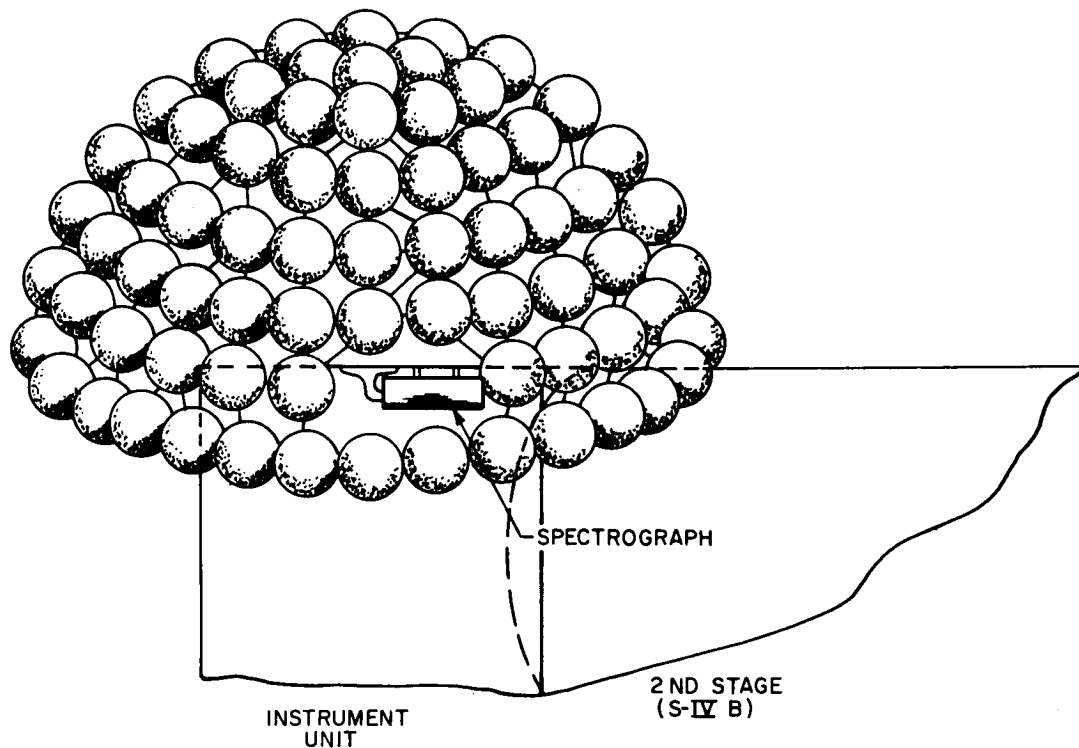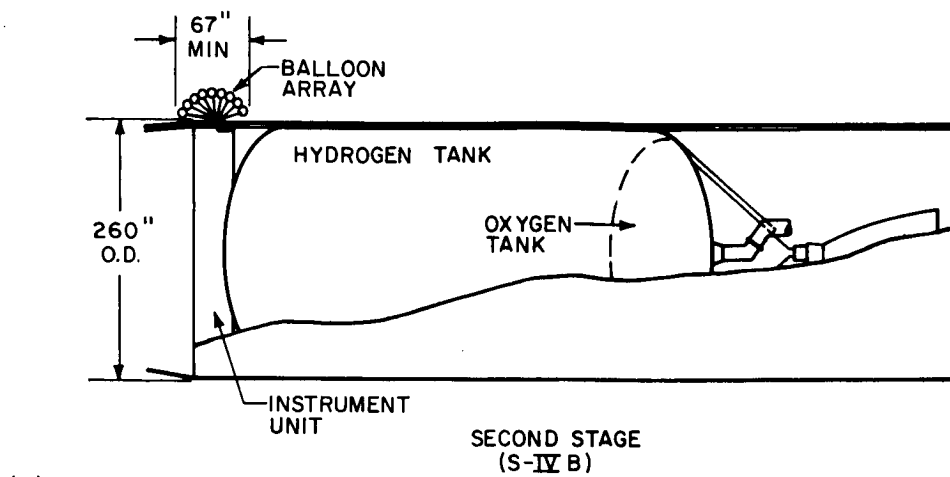
86-9674

Figure 23 ARTISTS CONCEPT OF FLIGHT MODEL OF METEOROID COMPOSITION
ANALYZER SPECTROGRAPH IN TYPICAL SPACE DEPLOYMENT (INTEGRATION
WITH SATURN S-IVB APOLLO-LABORATORY INSTRUMENT UNIT,
EARTH ORBITAL CONFIGURATION)

-72-
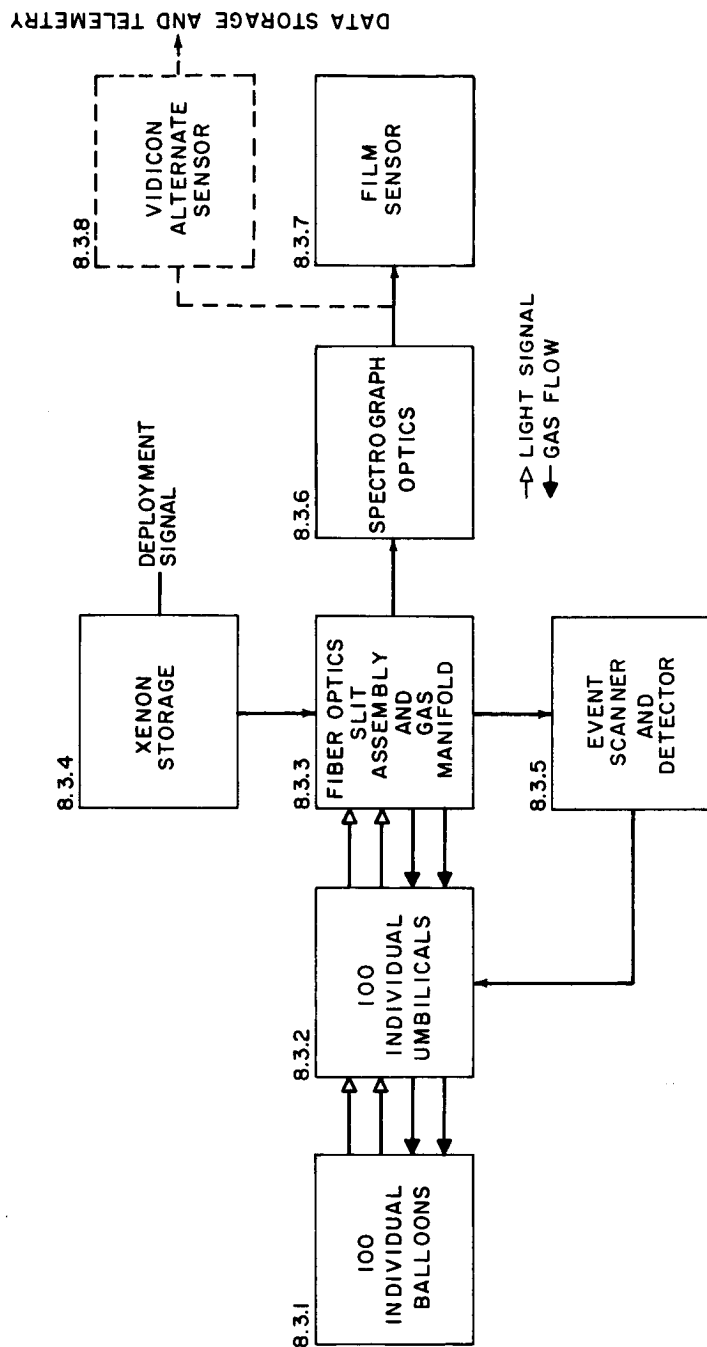
Figure 24 BLOCK DIAGRAM OF FUNCTIONAL COMPONENTS OF FLIGHT MODEL
ANALYZER SPECTROGRAPH SYSTEM

86-9675

-73-

the xenon reservoir and the gas manifold. A low-pressure gas flow slowly inflates the balloons through their individual umbilicals (which also include the fiber optics bundles). Inflation of the balloons effects a hemispherical deployment of the cluster around the port.

After inflation and resultant deployment are complete, a time-programmed electrical signal reduces the gas flow to maintain a minimum 100-day system pressure of 10 torr, controlled by the gas manifold valving and the restriction of the umbilical gas tubes. This signal also activates the event detector and fiber optics shutter device for recognition of balloon penetrations. In the case of the photographic film sensor, the system is now active. Substitution of the alternate vidicon sensor simply requires that the programmed signal activates the vidicon camera circuitry.

8.2.2 Description of System Operation

Referring to the block diagram in Figure 24, the following sequence of events takes place after a particle impact: A particle penetrates a balloon and is heated by interaction with the contained gas atmosphere. The resultant visible energy is transmitted through the individual fiber optics bundle to its terminal slit at the spectrograph's entrance plane. This light is then dispersed and imaged on the sensor. A portion of the fiber bundle, diverted at the slit assembly, also transmits light from the balloon to the event detector which senses the transient event and sends an electrical signal to the calibration lamp and to the sensor. In the case of film this signal serves to advance the exposed frame. In the alternate vidicon version, this signal initiates the read out of the displayed information. The event detector provides a second vital function in the sensing of unacceptable levels of continuous light flux from a punctured balloon. In this case, the device locates which is the offending balloon and sends an electrical signal to a small electrical coil surrounding the appropriate umbilical, melting and mechanically separating the plastic fibers, thereby blocking light transmission from that balloon. The system is now ready to receive additional data inputs.

8.3 FUNCTIONAL COMPONENTS OF THE FLIGHT INSTRUMENT

8.3.1 The Balloons or Spherical Test Cells

8.3.1.1 Function

Each individual balloon serves as an encapsulation device to contain a volume of inert gas. The thin sidewall membranes permit entry of micrometeoroids into the captive gas atmosphere where interaction with the gas raises the particle temperature, causing excitation of its constituent species and subsequent radiation during passage through the interior of the balloon.

8.3.1.2 Description

The individual balloons are 20-cm diameter spheres constructed of 14-micron thick Mylar. The drape-forming technique will be employed for fabrication. The exterior surfaces are multiple-aluminized in order to minimize UV deterioration of the Mylar, and to provide an opaque envelope to shield the open optical system. Interior surfaces of the balloons will also be aluminized for optical gain.

The basic experiment requires the deployment of a cluster of 100 balloons (see Appendix B) exposed to the space environment. The balloons, attached to their umbilicals, will be packaged in a cannister just inside the skin of the vehicle. After opening of a port in the vehicle surface, deployment will be effected by slow inflation of the balloons, avoiding mechanical deployment mechanisms which might injure the fragile membranes.

The 100-balloon cluster will be fabricated and packaged to deploy as a minimum 34-inch radius hemispherical configuration (see Figure 23) upon inflation. Each balloon is tethered by a short Nylon strip to each of its six neighboring balloons thereby creating, when inflated, a semi-rigid structure consisting of a triangular girder-like network. This basic geometry may be compared to that employed in inflatable radomes and similar structures. This tethering both aids efficiency of deployment by sole means of balloon inflation and also insures that, once deployed, the balloons assume and retain the hemispherical configuration which presents maximum surface area exposure. .

8.3.1.3 Developmental Status

Small Mylar balloons have been fabricated and successfully employed in this laboratory feasibility study. Mylar balloons have been successfully employed in a number of space experiments. State-of-the-art fabrication techniques developed by specialized vendors for these programs will be utilized for construction of the specific size balloons required for this experiment.

inside a balloon by means of a simple rigid connector. The fiber bundles are cylindrical, with the balloon ends "splayed" in order to see the entire balloon interior (see Subsection 3.4 of this report). The terminal end of each bundle is separated, a minimum of one fiber going to the event detector, and the ends of 20 fibers arranged in a slit configuration at the focal point of the spectrograph collimator.

A shutter device is provided for each fiber bundle to prevent ambient light from punctured balloons from entering the system. The fiber bundles will be destroyed by melting the plastic fibers and physically displacing the two remaining halves. This is accomplished by a small coil of AVTEMP alloy formed around each bundle. This metal possesses memory properties and the coil will be formed around each bundle from initially straight wire. Upon heating to 150° C by an electric current, the heat will melt the fibers and the wire will assume a straight geometry pulling the two halves apart and hence destroying the light transmitting properties of the fibers. Power required will be 5 watts and is applied for 10 seconds. Figure 25 shows the shutter before and after heating.

8.3.2.3 Status of Development

The fiber optics bundles are standard commerical shelf items. Several firms have fabricated composites employing a even larger number of individual fibers than the 2000 required for this geometry. The sheathing can be selected from a number of commercially available tubings and subjected to environmental testing.

8.3.2.4 Characteristics

    a. Weight: Total of 0.8 pound, including fittings

    b. Power: None (Shutter power included in Event Detector description)

    c. Size and Volume: (complete with balloons)

        1) Packaged: 44 cubic inches

        2) Deployed: The balloons will form a hemispherical array of approximately 3-foot radius. The umbilicals, of 34.5-inch length, disperse radially from the slit assembly to the individual balloons.

8.3.3   Plate and Gas Manifold Assembly

8.3.3.1 Function

This assembly provides the means of terminating the fiber optic elements to: (1) form the slit array; (2) illuminate the sensors used to detect the event and
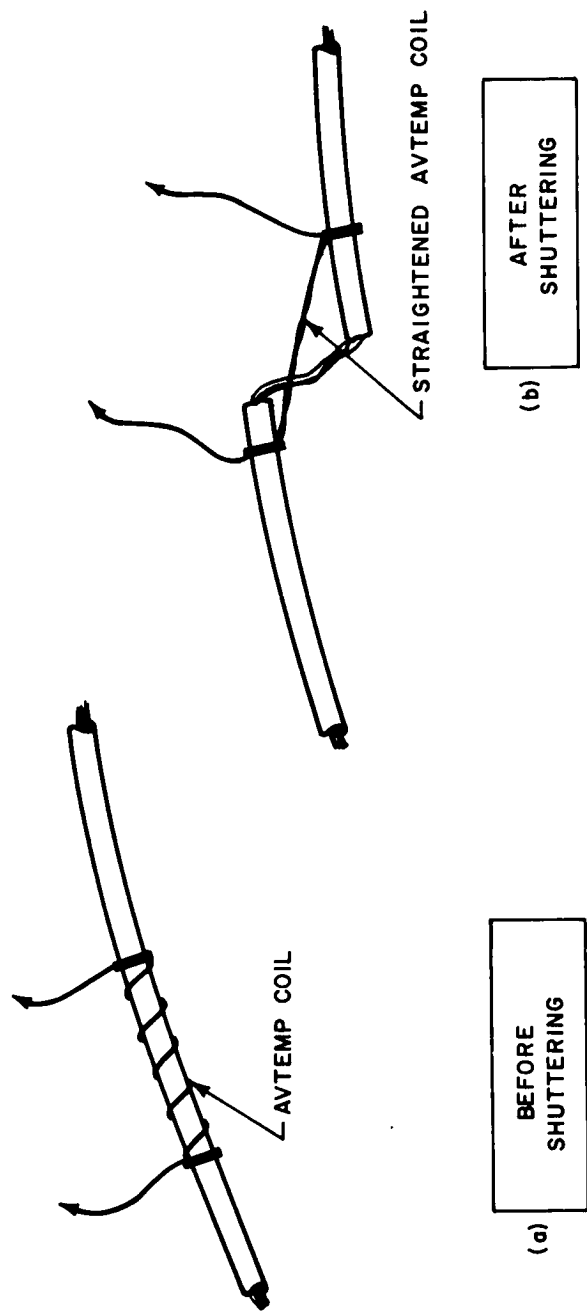
STRAIGHTENED AVTEMP COIL

AFTER
SHUTTERING

(b)

AVTEMP COIL

BEFORE
SHUTTERING

(a)

86-9676

Figure 25 THERMO-MECHANICAL SHUTTER FOR FIBER OPTICS BUNDLES

-78-

provide the fiber optics shutter signals; and (3) provide connection between the balloons and the xenon supply, via the outer fiber optic bundle jackets, for balloon filling and replenishment.

8.3.3.2 Description

The slit assembly is a plate approximately 3 inches in diameter and 1 inch thick. (See Figure 26a). The fiber optic bundles enter from the left. The outer sleeve terminates at the gas manifold header. The fiber elements are then separated into two groups; the first group leads to the right-hand face where the fibers from each bundle are arranged in single rows forming the spectrograph entrance slits. The second group of fibers lead to the periphery of the plate where the optical sensors used for event detection and fiber bundle shuttering are located. The slits formed by all the bundles are arranged in 10 x 10 array with a maximum occupied area of 0.1 x 0.3 inch including input from a spectral calibration lamp. The event sensing fibers terminate in two rows around the periphery to provide sufficient spacing to accommodate all 100 of their associated sensors. An inlet is provided into the gas manifold header for connection to the xenon gas supply and storage system.

The face of the fiber optics slit plate is covered by a composite neutral density filter consisting of a matrix of individual wedges, each wedge positioned in front of an individual slit. This provides continuous transmission attenuation along the slit height in order to further extend dynamic recording range of the system to cope with the anticipated broad event brightness range. The matrix filter will be formed by vapor deposition of inconel in order to provide flat spectral attenuation over the accepted bandpass.

8.3.3.3 Status of Development

Arraying of this number of fiber elements is within the current state-of-the-art. The major effort required for this item will be to set up for fabrication of this specific array. The gas manifold and the event sensor mountings are not expected to present any difficulties. Fabrication of the wedge filter is state-of-the-art but will require special tooling.

8.3.3.4 Characteristics

    a. Weight: 0.4 pound; total for the slit plate and event sensors.

    b. Power: None

    c. Size: 3-inch diameter x 1-inch thick plate. (extension to system optical system housing)

    d. Temperature Range: -50° C to +150° C
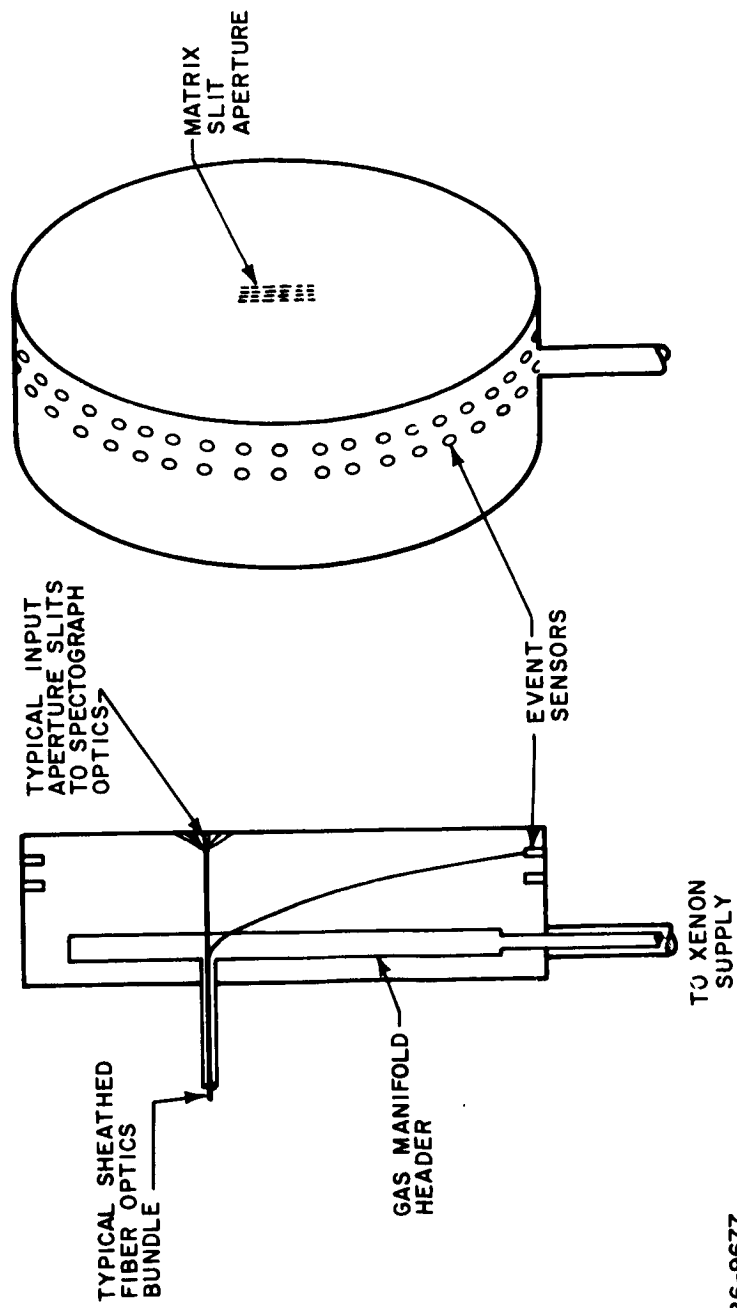
MATRIX SLIT APERTURE

TYPICAL INPUT APERTURE SLITS TO SPECTOGRAPH OPTICS

EVENT SENSORS

TYPICAL SHEATHED FIBER OPTICS BUNDLE

GAS MANIFOLD HEADER

TO XENON SUPPLY

Figure 26a SLIT PLATE AND GAS MANIFOLD

86-9677

8.3.4 Gas System

8.3.4.1 Function

The gas system serves two functions in this experiment: (1) It provides the motive power to deploy the sensor balloons from their launch package, and (2) it provides the atmosphere to heat the meteoroids for spectrographic analysis.

8.3.4.2 Description

Gas must be supplied at approximately 1 lb/in.^{2} to inflate the balloons properly and to deploy them. Once the balloons are deployed, a pressure of only 10^{-1} torr provides enough gas to interact with meteoroids penetrating the balloons.

The gas system to meet these requirements will consist of a storage container, a two-stage pressure reducer, a gas manifold, and the gas lines leading to each individual balloon. The storage container will be a one-half liter sphere. At 900-lb/in.^{2} pressure, such a container will hold 550 grams of zenon which provides a reasonable margin over what is needed to initially inflate the balloons and to provide makeup gas (See Appendix B).

The first stage of pressure reduction will be from 900 to 1 lb/in.^{2} A valved line will lead from this point to the manifold for inflation purposes. The second stage of pressure reduction will be from 1 lb/in.^{2} to 10^{-1} torr. After the line providing inflation pressure has been shut off and the balloons have lost pressure through leakage, this line will maintain 10^{-1} torr pressure in the manifold to feed the balloons.

The design and function of the restrictive flow gas lines to the balloons is discussed in paragraph 8.3.2.2. The only additional point that should be noted here is that when these very small lines are fed with 1-lb/in.^{2} pressure it will take about one day for the balloons to come to equilibrium at this pressure.

8.3.4.3 Status of Development

Small, high-pressure tanks of the type discussed are state-of-the-art flight hardware as is the first-stage pressure regulator. The second-stage regulator will have to be developed. An initial look at its requirements indicate that it is feasible.

8.3.4.4 Characteristics

    a. Weight: Pressure sphere .5 pound
                    Pressure reducers .75 pound total
                    Shutoff valve and piping .25 pound

b. Size: one-half liter sphere (9.6 cm diameter)

Other above equipment (another 500 cc)

Total: 61 cubic inches

c. Power: One-shot external trigger signal: 24 watts for 0.1 second.

d. Operating Temperature Range: -50°C, +100°C (minimum range)

8.3.5 <u>Event Detector and Fiber Optics Shutter System</u>

8.3.5.1 Function

The functions of the detector and shutter system are to detect an event, provide
a signal for advancement of film or start of vidicon recording, to search for
those fiber optic elements transmitting continuous background radiation into
the system, and to provide power to the appropriate shutters to effect removal
of those bundles from the system.

8.3.5.2 Description

It is obviously necessary to detect when a balloon has been impacted by a particle.
The event sensors described in the description of the slit plate will have a common
return so as to provide this signal. (See Figure 26b). Depending on the size of
the hole left in the balloon and the orientation of the system with respect to the
sun and earth, light may leak into the system causing fogging of the film (or
saturation of the vidicon tube) and obscuring of the spectral image. Light leakage
may also cause loss of subsequent film frames or vidicon images. Worst-case
estimates indicates that it is necessary to limit the exposure from such leakage
to less than 10 seconds.

A system is provided to sequentially scan the 100-event sensors. This is
accomplished using two 10-state counters driven by a clock pulse generator,
and 100 three-input "and" gates. Scan rates will be 50 to 100 scans per sec-
ond. Two of the inputs are used to perform the scan function and the third in-
put comes from the event sensor. When the three signals are simultaneously
present, the gate output fires a silicon controlled rectifier (SCR). The SCR
acts as a latching relay and supplies current to the proper fiber bundle shutter
to effect removal of that bundle and hence the leakage from the system. Some
integration of the event sensor output will be required since film readouts will
also integrate the leakage. The current to the shutters will be automatically
removed after a period just shorter than the scan cycle time to prevent spurious
signals from causing unnecessary removal of fiber bundles. Such a single short
current pulse will not activate the shutter. If on the next scan, the signal from
the event sensor is still present, the SCR will refire. This will continue until
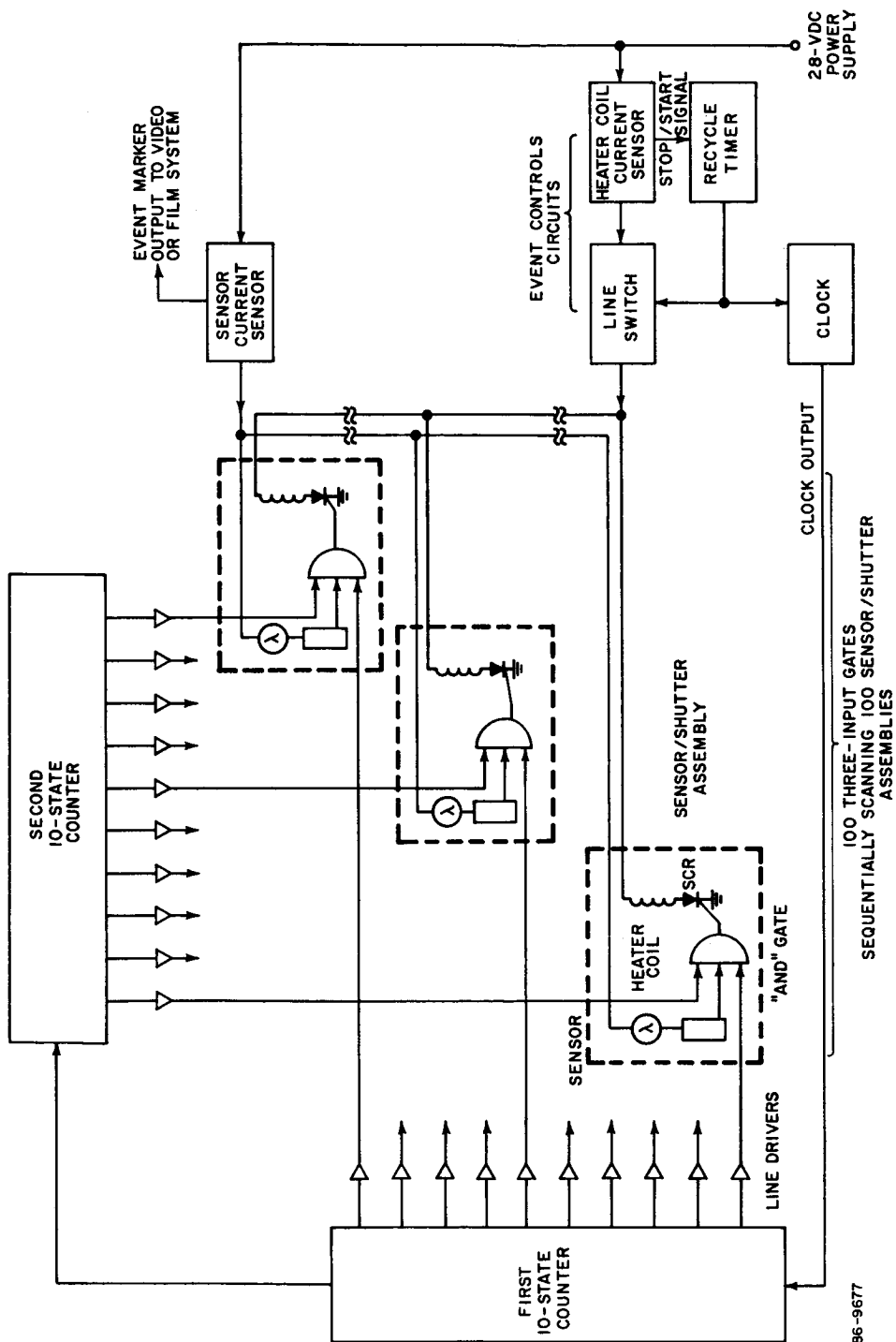either the fiber has been cut off or until a time-limiting, slow-acting fuse cuts

Figure 26b BLOCK DIAGRAM OF ELECTRONIC SHUTTER SYSTEM FOR MICROMETEROID COMPOSITION ANALYZER

86-9677

out that circuit. This will prevent continuous, unnecessary loading of the power supply. When several balloons are simultaneously punctured, provision is made to stop the clock pulse generator after turning on several shutters. This is done to limit the power supply drain. After 10 seconds, it will allow the clock to continue the scan.

Heat dissipated by these components will be used to keep the balloon temperatures above the liquification temperature of the xenon if required.

8.3.5.3 Status of Development

The entire system uses standard components of proven reliability. The only development required is to assemble this specific logic system and perform testing.

8.3.5.4 Characteristics

a. Weight: 1.2 pounds (event sensors are included in the slit-plate weight and shutters are included in the fiber bundle weight).

b. Power: 3.6 watts continuous; an additional 15 watts may be drawn for periods up to 30 seconds

c. Size: 9.3 cubic inches (can be arranged in almost any shape)

d. Temperature Range: -55 to +100°C

8.3.6 The Spectrograph Optics and Film Transport

8.3.6.1 Function

The optical system collects the light emitted from the fiber optics bundles at the slit assembly, collimates this light, disperses it as a function of wavelength, and images it upon the sensor. The film transport advances the film one frame after each data signal is recorded or as pre-programmed to minimize the integration of background light backage or very small particle impacts that produce below threshold spectral levels.

8.3.6.2 Description

The optical system is of symmetrical design, employing matched 75-mm focal length F/1.5 chromatically corrected lenses, one serving as collimator and the other as camera lens. Substitution of the second 75-mm lens for the longer lens used in the breadboard is permitted due to the use of smaller diameter fibers. Resolution is not degraded. Between them is a 600-line/mm transmission grating blazed for maximum efficiency in the visible. The resultant dispersion at the sensor plane of approximately 200Å/mm, in conjunction with the fiber image size of 0.001 inch (25.4 microns), yields a theoretical maximum

resolution of 5 A. This is within the resolution capabilities of both recommended sensors. System degradation to a final resolution of, at worst, 10 A is probably realistic and is acceptable.

The film transport mechanism requires a single, low-torque motor, and a switching device to activate the motor for advance of a frame upon command from the event detector. A common cylindrical housing contains the optics, film storage and transport, and provides for mounting of the slit attachment and gas manifold. All of these components, including the motor, will be designed for hard vacuum operation, but, for optimum reliability, the system will be sealed and pressurized. The takeup film cannister portion of the housing will be separately removable by the astronaut in either a shirtsleeve or hard vacuum environment.

8.3.6.3 Status of Development

All optical components are commercial shelf items and have been employed in design and subsequent testing of the breadboard instrument. Motors and minor electrical components suitable for the film transport system represent proven state-of-the-art space hardware. The only development will consist of fabrication of the mechanical housing and film transport mechanism, and the remounting of the lens elements in ruggedized cells integral with the housing.

8.6.3.4 Characteristics

    a.   Weight: 6.1 pounds

    b.   Size: 78 cubic inches, including film, instrument housing and slit plate

    c.   Power: 3 watts intermittent, for approximately 10-second duration

8.3.7 Primary Sensor: Photographic Film

8.3.7.1 Function

The film will record and store the spectral record of particle composition. This record will be retrieved for earth-based processing and analysis.

8.3.7.2 Description

Perforated 16-mm Extended Range (XR) film will be used. Developed by Edgerton, Germeshausen, and Greer (E.G.&G.) in conjunction with Eastman Kodak Co., this is a multiple layer film consisting of three panchromatic silver halide emulsions of varying sensitivities. The prime result of this configuration is the attainment of a very broad dynamic recording latitude. This latitude constitutes a maximum range of 10^6 to 1, providing excellent signal-to-noise

discrimination over four decades and usable data from the last two decades.

Final choice of the XR film is based specifically upon this superior dynamic latitude. Consideration of all of the tradeoffs involved in film selection points to maximum recording range as the most crucial sensor parameter. This is due to the several and considerable uncertainties involved in prediction of luminous flux levels from the vaporizing particles.

This film was not employed in the feasibility study because the Kodak Bimat on-board processing technique was previously considered for unmanned mission data readout and telemetry. The multilayer XR film is not adaptable to this diffusion transfer chemical process. The Bimat technique is no longer recommended for this experiment, and the sole objection to the XR film is no longer valid.*

8.3.7.3 Status of Development

The XR film is a shelf item in the required configuration. Its sensitometric characteristics have been thoroughly analyzed in consideration for use in the Apollo lunar missions.[22] Employment in an earth orbit will represent exposure to a far less hostile environment, particularly in terms of hard radiation background.[23, 24, 25]

8.3.7.4 Characteristics

    a. Weight: Included in specifications for optics and housing (approximately 0.02 pound for 100 data frames).

    b. Size: Included in dimensions of optical system housing.

    c. Power: Included in specifications for optical housing and film transport.

    d. Operating Temperature Range: Optimum: 0°C to +30°C

                                    Permissable: -50°C to +40°C, continuous soak

    <u>NOTE</u>: The film is not damaged by lower temperatures and responds down to -196°C but with reduced sensitivity and contrast.

---

*Deletion of the Bimat processing technique for unmanned missions: During initial planning of this experiment, both on-board film processing and vidicon camera systems were considered for missions requiring telemetry of the spectral data. At that time, performance of vidicon systems in the space environment had not warranted a high confidence level. The Bimat technique (subsequently employed in the Lunar Orbiter)[26] was therefore investigated as an alternate. Today, both techniques have been proven successful, but vidicon systems such as the Apollo Command Module instrument offer the least complex route. The prime advantage of a film-Bimat system compared to the vidicon camera is the much higher total number of information bits which can be recorded by the film. This experiment does not require such high information storage capacity.

8.3.8 Alternate Sensor: Vidicon Camera System

8.3.8.1 Function

If mission requirements should preclude the use of film, the alternate readout sensor would be a vidicon camera system.

8.3.8.2 Description

In this application, the vidicon photoconductor surface will be placed at the image plane of the spectrograph. Upon exposure to the dispersed spectral image, a corresponding charge pattern will be built up on the photoconductor surface where it is stored for a finite period of time until it is removed by electron-beam scanning. This scanning process generates a vidio signal that will be recorded on magnetic tape and subsequently telemetered to a ground station. The system best suited to this application is a modified Apollo Command Module TV camera. [15(b)]

The vidicon camera will scan continuously at a rate determined by the bandwidth of the on-board recording equipment. In this mode of operation, the photoconductor surface will be prepared for exposure at all times except for the 5-to 10-scanning periods required to remove the residual image following an exposure. When an exposure occurs, a signal derived from the event detector discussed previously will cause the scanning beam to be blanked off and returned to its starting position. If the recording equipment on board the vehicle requires an activation time following the arrival of a signal from the event detector, the readout scan will be delayed for a short period.

For maximum sensitivity and signal-to-noise ratio, 2 or 3 frames will be recorded because of the lag or residual image characteristics of slow-scan photoconductor surfaces. A typical slow-scan vidicon tube has about 35-percent residual signal after one scanning frame. After the third frame, the residual signal is down to approximately 10 percent.

8.3.8.3 Status of Development

Two minor modifications of the existing Apollo camera will be necessary in order to make it compatible with the proposed system. In its current form, it has been designed for continuous scanning at a frame rate of 10 frame/sec. At this frame rate, the horizontal resolution is limited by the bandwidth of the vidio amplifier to 220 TV lines. By modifying the camera sync-generator and deflection circuitry to reduce the frame rate, the horizontal resolution can be increased to 600 lines as required by the spectrograph optics for 10 A resolution. The existing 220-line vertical resolution is adequate for this application. The second modification will be the addition of a capability to interrupt and recycle the beam deflection circuitry upon command from the "event detector"

pulse. According to the manufacturer*, neither of these modifications will require major development.

8.3.8.4 Characteristics of the Apollo Camera

    a. Weight: 4.5 pounds

    b. Power Consumption: 6.5 watts

    c. Volume: 89 cubic inches

    d. Operating Temperature Range: -10°C to +55°C

8.3.9 <u>Summary of System Requirements</u>

8.3.9.1 System Using Film Sensor

    a. Total Weight: 10.5 pounds

    b. Total Volume: 192 cubic inches

    c. Total Power:

        1) Continuous: 3.6 watts

        2) Intermittant:

            a) One-shot pulse of 24 watts for 0.1 second

            b) Approximately 15 watts for 30 seconds for each data point

            c) Approximately 3 watts for 10 seconds for each data point.

8.3.9.2 System Using Alternate Vidicon Sensor

    a. Total Weight: 15 pounds

    b. Total Volume: 281 cubic inches

    c. Total Power:

        1) Continuous: 10.1 watts

        2) Intermittant: Same as in film system.

---

*Private Communication, Mr. R.A. House, Astro-Electronics Div., Radio Corp. of America, Princeton, N.J.

APPENDIXES

A. SPECTRAL DATA ANALYSES: Si/Fe (Ratio) DETERMINATION

B. SURVIVABILITY OF BALLOONS IN SPACE

C. THERMAL CONSIDERATIONS IN METEOROID COMPOSITION
   ANALYZER SPECTROGRAPHIC SYSTEM

APPENDIX A

SPECTRAL DATA ANALYSIS: SI/FE (RATIO) DETERMINATION

The following discussion concerns analytical data reduction of spectral records of meteoroid composition. Specific attention is given to discrimination between the primary "stony" and "iron" categories of particles, with consideration to the optical bandpass constraints of the present instrument system. A semi-quantitative technique is investigated and is seen to be applicable.

Given a spectral plate containing lines of Fe and Si, one basic question is; what is the range of ratios of Fe and Si contribution as determined from the intensity ratios of a given pair of Si and Fe lines? More pertinent, is it realistic to consider the Si emission detectable with this instrument as a reliable indicator of the stone-like class of meteorites?

A problem in determining the classification of a meteorite is that the percentages of composition can vary.[27] Types range from the iron-like materials with about 90 percent Fe and 10-percent Ni through intermediate composites of stone and iron to the stonelike type with about 20 to 50-percent SiO_2 + near 15-percent MgO plus several percent each of Fe_2O_3, FeO, Al_2O_2, and CaO. These are optimistic values as far as Si detection is concerned; see Reference 27 for an excellent table of meteorite composition. The Fe-Ni meteorite will have a clearly dominant spectrum of Fe.

Even in the case of a predominantly stone-like meteorite, the presence of Fe in any realistic proportion can mask the Si line (with Si detection limited to the 3905 A due to attenuation of the optical system). For example, take a meteorite of m grams with 50 percent by weight SiO_2 and 5 percent Fe_2O_3, plus 45 percent other components. Then there is 0.23m of Si and 0.035m of Fe available. If the temperature and time permit complete atomization of the oxides, then the ratio of Si/Fe in the gas phase is 6.6. As shown below, the Fe will interfere appreciably with Si for Si/Fe ratios of the order of 10 or less. This short and necessarily incomplete analysis leads to the conclusion that it is better to ignore Si as an indicator of stone-like character, and instead, consider the radiation from other atoms like Ca.

The following is an indication of how such questions can be approached and an example of the more detailed calculations which must be done for the flight experiment. A more complete treatment is given in Reference 28, supported by the tables in Reference 29.

The intensity (I) of a given line is given by $I = N_n h \dfrac{c}{\lambda} A_{nm}$

where N_n is the population (particle density) of the upper level n producing the transition from n to m of wavelength λ; c is the velocity of light and h is Planck's constant. A_{nm} is the line transition probability for emission. The intensity can be rewritten in terms of the total particle density N, the oscillator strength f, and the partition function U:

$$I = \frac{N}{U} g \, e^{-E/kT} \frac{8\pi^2 e^2 h}{\lambda^3} f$$

where $U = \sum_n g_n e^{-E_n/kT}$ is summed over all levels of significant population. T is the gas temperature, and g_n the statistical weight of each level.

If we assume thermal equilibrium and, that in an ablating meteorite, the ratio of Fe (subscript 1) and Si (subscript 2) in the gas phase is the same as the solid phase (no selective distillation), then

$$\frac{I_{Fe}}{I_{Si}} = \frac{I_1}{I_2} = \frac{N_1/U_1}{N_2/U_2} \frac{e^{-E_1/kT}}{e^{-E_2/kT}} \frac{g_1 f_1/\lambda_1^3}{g_2 f_2/\lambda_2^3}$$

Example:

The SiI (neutral Si) line at $\lambda_2 = 3905$ A has $(gf)_2 = 0.20$; the transition has upper level E2 at 40,992 cm^{-1}. The value of U_2 (summed up to levels corresponding to 14000°K)[1] = 9.5. This is not a particularly strong line, but is the only Si line detectable in the range of the spectrograph of concern here; one must go to 2881 A for an appreciably stronger line, and then to 2528 A for other strong lines. The selection of a suitable FeI line is more difficult because of the richness of the many-line spectrum. Within the instrumental constraints of λ_1 between 3900 A and 6900 A there are still many lines. However, one meaningful calculation is the intensities of the iron doublet (3903.0 and 3903.9), which can mask the Si line at 3905.5 A. i.e., how much Fe will render the Si undetectable? The Fe constants are:

λ, A	gf	E	U
3903.0	1.3	38175 cm^{-1}	28.5
3903.9	0.95	48727	
3906.5	0.012	26479	

See references 28 and 29, for other adjacent FeI lines.

Since the wavelengths are practically the same, and taking the gas temperature as 5000°K,

$$\frac{I_{Fe}}{I_{Si}} = \frac{(N_1/28.5)}{N_2/9.5} 1.3e \frac{\dfrac{-38175 \text{ cm}^{-1}}{kT} + 0.95 e \dfrac{-49727 \text{ cm}^{-1}}{kT}}{0.20 e^{-40,992/kT}} \quad ;$$

thus

$$\frac{I_{Fe}}{I_{Si}} = 4.96 \frac{N_{Fe}}{N_{Si}} \quad .$$

Then for equal intensities of the lines in question $N_{Si} = 5N_{Fe}$, or the gas should be about 85 percent Si and 15 percent Fe. However, to provide positive identification of Si with the resolution and calibration accuracy available, it seems realistic to depend on almost the total absence of Fe, as determined by the weakness or absence of other moderately strong Fe lines, like that at 4046 A. Thus the ratio Si/Fe = 6.6 given earlier is unrealistic for positive identification of Si.

Turning to the use of Ca as an indicator, most iron meteorites contain little Ca^{27} (although the NASA "test" sample shows significant Mg). However, Ca is characteristic of the stony meteorites. Take a case where the Ca is low, but still typical of the "stony" meteorite (chondrites, 86 percent of total terrestrial falls); i.e., 2-percent CaO and 10-percent FeO.

Calculations of the type previously illustrated can be made. However, sufficiently good estimates can be obtained using Reference 29, where intensities from different elements can be directly compared since, in this definitive work, intensity data has been reduced to a common excitation temperature (coincidently, for present purposes, of 5100°K) and for the same atomic percentage of each element. Thus, tabulated intensities[29] can be used to estimate relative abundances of different elements. For the strong lines in the visible of interest here:

Spectrum	λ,A	Intensity (relative)
CaI	4227	1100
FeI	4000 to 6900	300 at 4046 A; 170 and usually much less elsewhere in this range

In the 2-percent CaO-10-percent FeO case, the ratio of Ca to Fe is 0.91. Then the Ca line will be 3.3 times as intense as the Fe line at 4046. In general, one may expect this and other Ca lines to dominate Fe until there is appreciable departure from the typical stony composition. Intermediate or mixed compositions will require closer analysis, and probably confirmation by test spectra with the actual instrument.

93/94

Appendix B

SURVIVABILITY OF BALLOONS IN SPACE

1.0 PENETRATION PROBABILITIES AND GAS-MASS LOSSES

The deployment of the meteoroid analyzer concept for measurement of the composition of meteoroids in a space environment requires that the balloons remain inflated for an extended period of time. The length of this time is determined either by the mission duration or by the time required to secure an adequate number of data points. This latter time depends upon the expected meteoroid flux density. The diffusion rate of a heavy gas such as xenon through the aluminized Mylar is sufficiently small to permit the deployment of a balloon in a vacuum environment for periods of order 1 year without requiring any significant replenishment of the gas. Assuming that the filling tubes, valves, reservoir chambers, etc., can be made equally free from leaks, then the primary threat to the survivability of the experiment comes from the loss of gas through tiny holes made by meteoroid particles which are too small to provide a radiation signature in the gas, but large enough to puncture the aluminized Mylar skin.

The extrapolation of laboratory data obtained at velocities up to 10 km/sec to the actual velocities encountered in the space environment in order to determine the mass and size of a meteoroid, which will penetrate the balloon surface and have sufficient remaining energy to produce the necessary spectral signature, is very difficult to do with assurance. First, the penetration parameters are not well established and, secondly the density-mass-velocity distributions of the meteoroid flux to be measured are not well defined.

The data obtained on Pegasus I and II have been published by Naumann. [30] These data show that penetration of a 38-micron aluminum panel backed up by a 12-micron Mylar dielectric occurred on both satellites at a fairly reproducible frequency of order 1.5×10^{-6} penetrations/meter^2-second. Regardless of the penetration parameters, these data show that a 14-micron Mylar surface will be penetrated with at least this penetration rate and with sufficient energy or momentum to have penetrated a reasonable thickness of aluminum in addition. Assuming that such a penetration into one of the meteoroid analyzer balloons will produce a signal, the mean time required to produce a signal assuming a 20-cm diameter balloon and assuming a hemispherical surface of this balloon to be exposed is:

$$\bar{T} = \cfrac{1}{A_{(balloon)} \times \cfrac{\text{Frequency of Penetrations}}{m^2 - \text{second}}}$$

$$= \cfrac{1}{2\pi (0.10)^2 \times 1.5 \times 10^{-6}}$$ (1)

$$= 1.06 \times 10^7 \text{ seconds } = 123 \text{ days}$$

The probability that such a balloon will be penetrated at a given time T is given by:

$$P = 1 - \exp - T/\bar{T}$$ (2)

This expression indicates that 100 balloons, each exposing a hemispherical surface will receive 63 penetrations or data producing events in $T = \bar{T}$ or 123 days. If one takes a nominal mission duration of 100 days as a desirable goal, it is necessary to determine the quantity of gas required to maintain a captive atmosphere of suitable pressure to provide signals for the spectrograph. The rate of growth of the combined area of holes produced in the balloon surface by meteoroids smaller than those which produce a signal is desired. Some lower cutoff limit in mass must exist which will not produce a penetration of the Mylar surface.

A plot[31] of the rate of arrival of particles with mass greater than m grams is shown in Figure B-1. Plotted on this graph are data points obtained from satellite observations as indicated. The data representing penetrations of the 38-micron panels on Pegasus II and III is located as shown by the arrow. A lower limit of mass required to penetrate the surface may be taken as 10^{-10} grams; however, it can be shown that the leakage rate is very insensitive to this lower limit so that the number selected is quite unimportant.

One may assume, for purposes of analysis, that the meteoroid particles are spherical in shape, and that they produce a hole equal in area to the cross-sectional area of the sphere. (Note, the hole area may be slightly larger than this cross-sectional area but probably not more than a factor of 2. This small factor will be neglected in the absence of experimental data.) The puncture area, Q, per penetration is related to the mass by

$$Q = 1.2 \left(\frac{M}{\rho} \right)^{2/3}$$ (3)

where

M = mass in grams

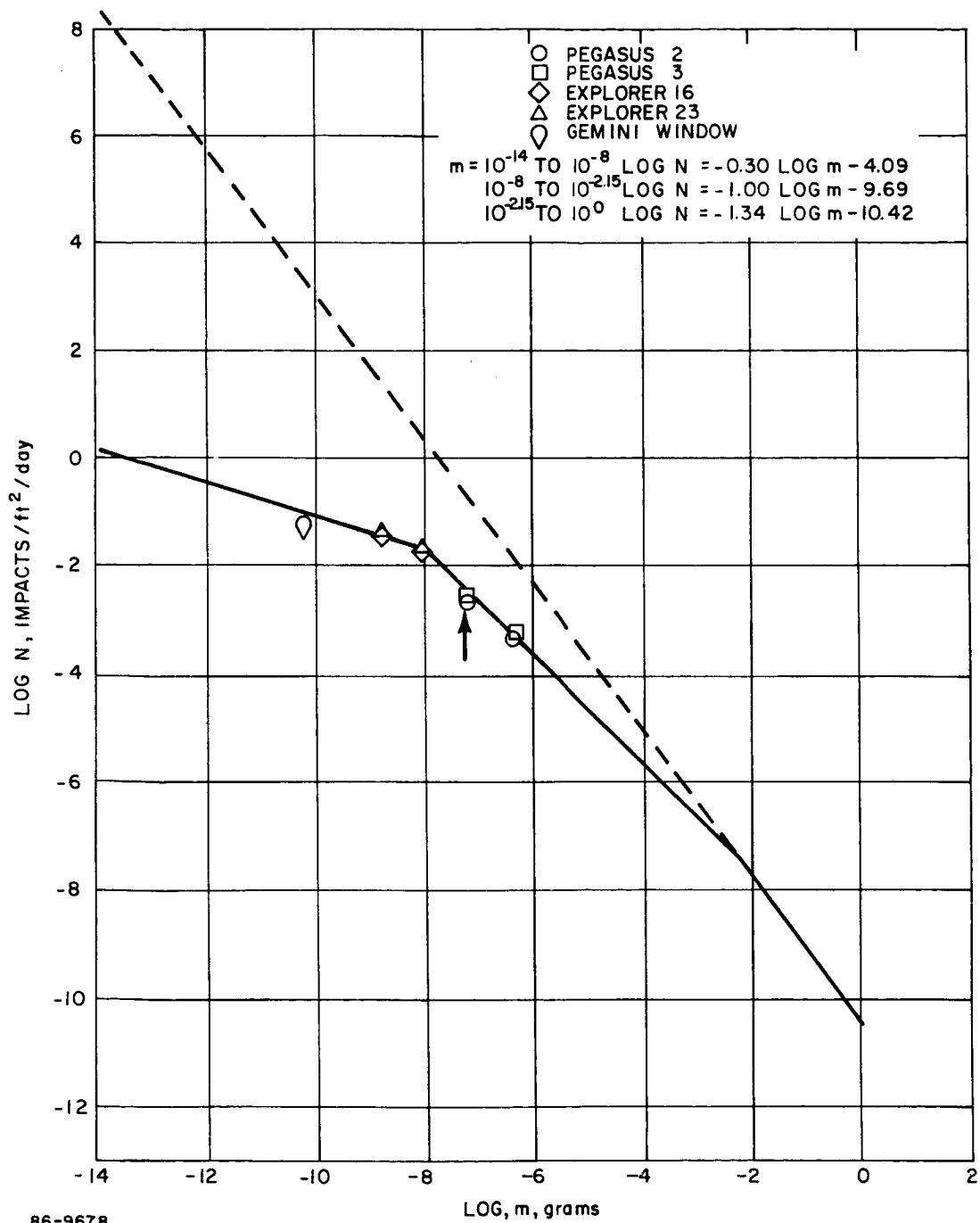ρ = density of meteoroid in gm/cm^3

Figure B-1 PLOT OF MICROMETEROID FLUX DENSITY VERSUS MASS

86-9678

The leakage area S increases with time, t, and is given by:

$$S = A_b \frac{1.2}{\rho^{2/3}} t \int_{M_p}^{M_s} \frac{dN}{dM} M^{2/3} dM \qquad (4)$$

where M_p is the minimum mass which will produce a penetration, and M_s is the mass required to produce a signal or end of required life of the balloon. If M_p is chosen as 10^{-10} gram and M_s is $10^{-7.3}$ gram, the integration of Equation (4) using the relations of N and M of Figure B-1, yield (for $\rho = 3$):

$$S = 49.7 \times 10^{-9} t \text{ cm}^2 \qquad (5)$$

The rate at which gas is lost from a container through a hole in a thin wall is given by:[32]

$$R = 3.62 \sqrt{\frac{T}{M}} P \text{ torr liters/cm}^2\text{-sec}$$

where

R = leak rate into a vacuum

T = temperature in °K

M = molecular weight of gas.

This equation assumes free-flow, that is, where viscous forces are negligible and the mean free-path is greater than the hole diameter ($p \leq 1$ torr). It neglects the effect of the wall thickness on the flow and therefore gives results which are greater than that to be expected in the actual case.

For xenon at 300°K,

R = 5.5 P torr liters/cm²-sec

now,

$$1 \text{ torr-liter of Xe} = \frac{130}{22.4 \times 760} = 7.63 \times 10^{-3} \text{ grams}$$

therefore,

R = 42.1 x 10^{-3} P gm/cm²-sec

= 3.64 x 10^3 P gm/cm2-day $\qquad$ (6a)

For pressures greater than 1 torr, viscous flow must be considered. An engineering relation for a thin aperture for air at 300°K is

$$R_{air} = 19.8 \ P \ torr \ liters/cm^2\text{-sec}$$

Assuming that viscous forces dominate, the same formula for xenon would be

$$R_{xenon} = 19.8 \ \frac{\eta_{air}}{\eta_{xenon}} \ P \ torr \ liters/cm^2\text{-sec}$$

$$= 15.9 \ P \ torr \ liters/cm^2\text{-sec}$$

where:[33]

$$\eta_{air} = \text{viscosity of air} = 1.796 \times 10^{-4} \ dyne\text{-sec/cm}$$

$$\eta_{xenon} = \text{viscosity of xenon} = 2.236 \times 10^{-4} \ dyne\text{-sec/cm}$$

This may be expressed:

$$R_{viscous} = 10.5 \times 10^3 \ P \ gm/cm^2\text{-day} \tag{6b}$$

A reasonable approximation for the flow rate for pressures $0.1 \le P \le 10$ torr would be an average of these two flow rates or

$$R_{av} = 7 \times 10^3 \ P \ gm/cm^2\text{-day} \tag{6c}$$

The rate of increase of gas consumption is then:

$$R_{av} S = 28.3 \times 10^{-5} \ Pt \ gm/day \tag{6d}$$

The mass of gas required to maintain an initial pressure of P torr is

$$Mg = \int_o^t RS \ dt$$

$$= \int_o^t 28.3 \times 10^{-5} \ P t \ dt$$

$$= 14.2 \times 10^{-5} \ P t^2 \ gm/torr \tag{7}$$

For a time period of 100 days, this indicates a total of 1.4 Pgm/torr. The initial mass of xenon gas in a 20-cm diameter balloon is 0.032 gm/torr.

The relation shown in Equation (7) indicates clearly that it is desirable to operate at a minimum pressure inside the balloon consistent with the production of an adequate optical signature from the ablation products of the meteoroid particle. The following section describes the interaction of a meteoroid with a low-pressure gas.

2.0 PASSAGE OF PARTICULATE MATTER THROUGH LOW-PRESSURE GASES

Most experimental work on the radiation from particles passing through gases has been performed under conditions in which the mean free-path of the gas has been considerably less than the size of the particle. Under these conditions, the radiation from the ablation products of the particle is thermal radiation from the shock layer in the vicinity of the particle and from the heated wake.

In the low-pressure extreme, the mean free-path in the gas is considerably larger than the body dimension of the particle. Under these conditions, there is no shock layer, and the radiation arises from the collisions of the ablation products with the cold ambient gas. Since the velocity of these products with respect to the cold gas is essentially that of the particle, the initial kinetic energy of the ablation molecules or atoms is quite high, tens of, electron volts. It is therefore reasonable to state that the amount of radiation released per ablation atom or molecule is much greater in the low-pressure case than that observed in the high pressure case.

The important criteria, then, in the low-pressure case, is whether or not appreciable vaporization does indeed occur.

At low pressures, the heat flux to a particle of radius r is

$$P = \frac{1}{2} \pi r^2 \rho v^3 \text{ erg/sec} \tag{8}$$

where ρ is the gas density and v the velocity if a thermal accomodation co-efficient of unity is assumed. At the velocity of encounter (2×10^6 cm/sec) the kinetic energy of a xenon atom striking the surface is about 270 electron volts. At this energy the atom will penetrate into the particle, ensuring a high accomodation coefficient. The thermal radiation from the particle will be

$$P = 4\pi r^2 \, 5.67 \times 10^{-5} \, T^4 \text{ erg/sec} \tag{9}$$

if the thermal emissivity is assumed to be unity. From Equations (8) and (9) one can calculate the equilibrium temperature, assuming no other losses (i.e., ablation), to be

$$T = (700 \, \rho \, v^3)^{1/4} \, ^{\circ}K \tag{10}$$

Now, the density of xenon, at a pressure of p torr, is 7.7×10^{-6} p gm/cm^3, hence

$$T = 0.271 \, (p \, v^3)^{1/4} \, ^{\circ}K \tag{11}$$

-100-

At a velocity of 2×10^6 cm/sec,

$$T = 1.46 \times 10^4 \, p^{1/4} \, °K$$

so that even at a very low pressure (10^{-2} torr), an equilibrium temperature of $4.6 \times 10^3 °K$ would be attained. At this temperature most refractory materials boil, so that appreciable ablation would occur even at 10^{-2} torr. At 10^{-1} torr, the equilibrium temperature would be much higher ($8.2 \times 10^3 °K$). Actually, the ablation would utilize enough energy to prevent the attainment of such a high temperature, so that, at pressures above 10^{-2} torr, the effect of radiation from the body can be neglected.

Another question is whether or not there will be sufficient time to heat the fragment. Actually, the fragment will be heated to a very high temperature by the impact on the Mylar film, so that it is reasonable to neglect the time required to heat a cold particle.

Now, the rate of evaporation, if we neglect other losses, is given by

$$dm/dt = -\frac{1}{2} A \rho v^3 / L \tag{12}$$

and the rate of slowdown

$$dv/dt = -A \rho v^2 / m \tag{13}$$

where A is the projected area of the particle. These two equations can be combined and integrated to obtain

$$m = m_0 \exp - (v_0^2 - v^2)/4L \tag{14}$$

where m_0 is the initial mass, v_0 the initial velocity, and L the latent heat of evaporation per gm. Since L is about 5×10^{10} erg/gm for most materials, and v_0 is 2×10^6 cm/sec, it is clear that most of the mass is lost before appreciable velocity change occurs. Equations (12) and (13) cannot be exactly integrated to find the mass lost as a function of distance traversed. However, one can estimate the lower limit on mass loss by assuming the mass remains constant in Equation (13), finding the rate of slowdown, and using this in Equation (12). Thus

$$v^{-2} dv = -(A \rho / m_0) \, dt$$
$$-1/v = -A \rho t / m_0 - 1/v_0$$
$$v = v_0 (1 + A \rho v_0 \, t / m_0)^{-1}$$
$$x = (m_0 / A \rho) \ln (1 + A \rho v_0 \, t / m_0)$$
$$= (m_0 / A \rho) \ln (v_0 / v) \tag{15}$$

$$v = v_0 \exp - A \rho x / m_0 \qquad (16)$$

If v is nearly v_0, $A \rho x / m_0$ is small, and

$$v_0^2 - v^2 = 2 A \rho v_0^2 x / m_0 \qquad (17)$$

On insertion of Equations (17) into (14), we have

$$m = m_0 \exp - A \rho v_0^2 x / 2 L m_0 \qquad (18)$$

from which the relative change in mass is

$$\Delta m / m_0 = - A \rho v_0^2 x / 2 L m_0 \qquad (19)$$

Now, let us assume that the particle is a dense sphere, of density about 3. Then $A = 0.5 m_0^{2/3}$. Also $\rho = 7.7 \times 10^{-6} P$ for xenon, and $L = 5 \times 10^{10}$. Then

$$\Delta m / m_0 = -3.84 \times 10^{-17} x P v_0^2 / m_0^{1/3} \qquad (20)$$

For an initial velocity of 2×10^6 cm/sec, and a mass of 10^{-6} grams,

$$\Delta m / m_0 = -1.54 \times 10^{-2} x P \qquad (21)$$

The path length in the balloon will average about 20 centimeters, so that the fractional mass loss will be

$$\Delta m / m_0 = -0.3 P$$

At a pressure of 1 torr, about 30 percent of the mass will be lost, and at 0.1 torr 3 percent of the mass will be lost. In actual practice, it is highly likely that the particle will fragment, as a result of the stresses encountered on impact, and because of the high temperature attained. If the fragments have a mass of 10^{-9} grams, the relative mass change is increased by a factor of 10, so that a 30-percent loss occurs at a pressure of 0.1 torr.

At these low pressures, the mean free-path of the gas is large compared to the body dimension. At 0.1 torr the mean free-path is about 0.5 mm, whereas a compact mass of 10^{-6} grams has a diameter of 0.08 mm.

From the preceding equations, one can also estimate the amount of energy deposited per unit length of path by the evaporated vapor. That is

$$dE/dx = 1/2 \rho v^2 \, dm/dx$$
$$= 1.92 \times 10^{-17} P v_0^4 m_0^{2/3} \qquad (22)$$

for a particle of density 3, mass m_o, and initial velocity v_o. For a typical particle of mass 10^{-6} grams, and velocity 2×10^6 cm/sec,

$$dE/dx = 3.06 \times 10^4 \, P \, erg/cm$$

where P is the xenon pressure in torr. Since the total kinetic energy of the particle was 2×10^6 ergs, the relative amount of energy available to cause radiation is

$$1.5 \times 10^{-2} \, P \, erg/cm \text{ path length.}$$

Thus, even at a pressure of 10^{-1} torr, the total energy released into the vapor in a 20-cm path length is

$$E = 6 \times 10^5 \, P = 6 \times 10^4 \, ergs.$$

One can estimate also the temperature increase associated with the passage of the particle, by assuming the energy is deposited in a distance of about 3 mean free-paths from the trajectory of the particle. The mean free-path at a pressure of P torr is about $5 \times 10^{-3}/P$ cm. Thus the volume affected per unit length of path is $7 \times 10^{-4}/P^2$ cm^3, and this volume receives an energy of $3.06 \times 10^4 \, P$ ergs, or an energy per unit volume of $4.4 \times 10^3 \, P^3$ erg/cm^3. Now, xenon at a pressure of P torr has a heat capacity of $7.4 \, P$ erg/cm^3 °K. The temperature rise of the gas is thus only $600 \, P^2$ °K and one would not expect to observe any large amount of thermal radiation at pressures below a few torr. However, the kinetic energy of the vaporized gas, with respect to the cold xenon, during the first few collisions, is much larger than the average kinetic energy of the heated gas. Radiation then occurs as a result of the collisions between the very high energy vapor species and the xenon. Since this energy is much higher than the thermal energy of the heated gas, the radiation from the primary collisions will far exceed the thermal radiation.

In summary, it appears that operation of the meteroid analyzer experiment at low pressures (10^{-1} torr) is feasible, provided that a sufficient portion of the energy available as a result of vaporization is released as radiation. Because at low pressures, the radiation arises from high energy collisions between the vaporized matter and the cold xenon, it is reasonable to state that this efficiency will be higher than the efficiency of radiation from a thermal source. Also, the total energy available from the passage of a small particle through a low-pressure gas is proportional to the fourth power of the velocity; and since the radiation must arise from a primary collision process, the radiation in turn is proportional to the fourth power of the velocity. The radiation should also be proportional to the pressure. In effect, these considerations indicate that extrapolation of data obtained at high pressures to low pressures should be conservative, provided that the low pressure is high enough to permit ablation.

Thus, the low-pressure limit for small particles should be on the order of 10^{-1} torr.

For the conditions assumed (one balloon, 100 days) in arriving at Equation (7), it is apparent that the mass of gas required for maintaining a minimum pressure of 10^{-1} torr is of order 0.15 gram. The weight penalties for supplying this quantity of gas even for 100 balloons is not severe.

One can derive the pressure as a function of time relationship based on the leak rates established in Equation (6d) assuming that a balloon is initially pressurized to P_o torr.

$$R_{av} \ S = 28.3 \times 10^{-5} \ P \ t = \frac{dm}{dt} \quad \text{gm/day.} \quad (6d)$$

For the conditions of constant temperature and constant volume of the balloon, the pressure of xenon is related to the mass by:

$$P = 31.3 \ m \tag{23}$$

$$\frac{dP}{dt} = 31.3 \ \frac{dm}{dt} \tag{24}$$

Using this relationship, Equation (6d) can be written:

$$\frac{dP}{dt} = 88.7 \times 10^{-4} \ P \ t$$

or

$$\frac{dP}{P} = 88.7 \times 10^{-4} \ t \ dt \tag{25}$$

This may be integrated to yield:

$$P = P_o \ \exp - 44.4 \times 10^{-4} \ t^2 \tag{26}$$

If it is desired to permit P to vary from an initial pressure of 10 torr to a minimum pressure of 0.1 torr, the time required is 14 days. It is not possible to provide an initial pressure in the balloon to assure a pressure of 0.1 torr for a period of 100 days.

It is desirable, therefore, to maintain a pressure of 0.1 torr in each balloon by means of a tube connected to a central reservoir. If one considers the flow of gas through a long pipe exhausting into a vacuum, the flow rate, neglecting viscous effects, is [34]

$$R_p = 3.81 \sqrt{\frac{T}{M}} \frac{D^3}{l} P \text{ torr-liter/sec} \tag{27}$$

where

D = diameter of pipe in centimeters

l = length of pipe in centimeters

For xenon at 300°K

$$R_p = 3.82 \times 10^3 \frac{D^3}{l} P \text{ gm/day} \tag{28}$$

Setting this flow rate through the long pipe equal to the maximum flow rate at the end of 100 days given by equation (6d), one obtains:

$$28.3 \times 10^{-3} P = 3.82 \times 10^3 \frac{D^3}{l} P$$

or

$$\frac{D^3}{l} = 7.41 \times 10^{-6} \tag{29}$$

Let

l = 100 centimeters

then

D = 0.09 centimeters

Such a filling tube would thus limit the maximum flow rate for a reservoir pressure of 0.1 torr to 0.0028 gm/day. Even if the balloon were missing from the filling tube, the total loss of gas in 100 days would be only 0.28 gram. The mass of gas required to pressurize the balloon to 0.1 torr is 0.032 gram. The above flow rate will fill the balloon in a reasonable time period. These conditions are based on free-flow conditions and, therefore, the flow rates calculated may be smaller than actual flow conditions but should be within an order-of-magnitude. Clearly, the flow rate can be adjusted by changing the diameter of the tube and its length. These numbers indicate that a nearly passive system can be built to maintain the pressure within the balloons without requiring sophisticated pressure sensors in each balloon.

APPENDIX C

THERMAL CONSIDERATIONS IN METEOROID COMPOSITION ANALYZER SPECTROGRAPHIC SYSTEM

1.0 THERMAL CONTROL

1.1 Requirements and Constraints

The overall temperature of an orbiting satellite (or component) is a function of heat lost by radiation through exterior surfaces and that energy absorbed from ultraviolet, visible, and infrared thermal radiation as well as from internally generated heat. In the absence of gravity, heat is transferred by conduction (internally) and radiation (internally and externally) only, with radiation the predominant means of energy exchange. Therefore, since radiation is a significant factor, temperature control can, in most cases, be achieved through purely passive means, i.e., by properly orienting radiative energy exchange and interchange surfaces and by applying coatings having specified radiative properties to external and internal surfaces. Further control is possible by limiting or increasing the heat leakage between external surfaces and the interior, and between adjacent surfaces or components. Heat leakage can be controlled by applying thermal insulation and, where applicable, by specifying contact resistances between joints.

The basic function of the thermal control system is to maintain the temperature level of all components within limits during exposure to a constantly changing external thermal environment. Typical nonoperative and operative temperature specifications for significant components of the meteoroid analyzer spectrographic system are summarized in Table C-1. The analyzer temperature limitation is dictated by the option selected for data recording (photographic film or Vidicon camera system). The balloon temperature specification depends on the base material selected. Mylar is assumed.

The proposed analyzer system/Saturn S-IV B integration in the orbiting configuration is shown in Figure 23.

1.2 Thermal Control System Description

The preliminary design thermal-control system evolved to satisfy the above worst considerations is discussed in the following sections. The meteoroid analyzer spectrographic system consists essentially of the instrumentation module, the balloon array (consisting of one hundred 20-cm diameter balloons), fiber optics strands connecting the instrumentation module and the balloons, and hardware for balloon ejection, pressurization, etc. The instrumentation module, containing the analyzer and data processing equipment, is mounted to a thermal conditioned panel integral to the S-IV B instrumentation unit.

TABLE C-1

TYPICAL COMPONENT TEMPERATURE SPECIFICATION FOR FLIGHT INSTRUMENT

Component	Material	Typical Temperature Specification		Location	Thermal Design Approach
		Nonoperative (°F)	Operative (°F)		
1. Analyzer	Various	-50 to +250	(1) 0 to 175 (1)	Instrumentation module inside instrumentation unit	Active system (Thermal conditioned panel) from launch to orbit injection (2). Passive system (coatings and insulation). supported by heat supplied on demand through heating elements during orbital mission.
A. Photographic film option		-50 to +70	(3)	Instrumentation module	Same as above
B. Vidicon Camera option	Various	0 to +140	(4) +20 to +100 (4)	Instrumentation module	Same as above
2. Balloon Array	Aluminized Mylar (5) Argon Gas	-320 to +212 / >-310	(6) / (8)	Instrumentation unit; exposed to space after inflation	Low - ε, low - α coating; Radiant and/or conductive heat supply on demand after inflation (7)
3. Fiberoptics bundles	Crofon Polyester			Instrumentation unit	Integrated heater wire to supply heat on demand after balloon inflation (7)
4. Pressurization system		-100 to +300		Instrumentation unit	None required

(1) Temperature limits for electronics components
(2) Supplied by spacecraft manufacturer
(3) Temperature control within +30 to 70° F desirable; upper short-time limit +100° F
(4) Environmental Temperature; more close control by integrated heaters.
(5) Preliminary material specification
(6) Thermal cycling test temperature specification, supplied by Schjeldahl Company
(7) Requirement depends on orbit selection and spacecraft attitude relative to the sun and Earth.
(8) Melting point of solid argon; lower limit -169° F if substituted by xenon.

Thermal control of the S-IV B during ground operations and throughout flight until some time after orbit injection is provided by circulation of a methanol-water mixture, which enters the cold plate at 60° F (max.) and leaves at 70° F (max.). The total allowable heat load per panel is 500 watts. The advantage of an active thermal control system is utilized until the water used to remove heat through a heat exchanger has been boiled off. The preliminary thermal control system considered for operation during the following 30- to 100-day orbit is a passive system utilizing coatings with specified radiative properties, insulation materials and in the worst-attitude case, some additional heat supplied through electric resistance heaters on demand. No final definition, however, is possible without more extensive analysis and prior knowledge regarding orbital parameters (altitude, inclination) as well as vehicle orientation (fixed attitude, rolling or tumbling vehicle).

Low-ϵ coating (ϵ = infrared emittance) are utilized on the balloons and on all exposed surfaces of the instrumentation module. In addition, the instrumentation module is highly insulated by the application of reflective super-insulation layers. A low-α value of the coating provided for the balloon assures reasonable temperatures during full-sun exposure.

Additional heat may be supplied, if required, through resistance heaters located such that they conduct and/or radiate thermal energy effectively to the balloons. Two systems, a radiating and a conducting system, have been considered. The first system consists of a heat source located near the center of the hemisphere which provides energy to the balloon array through radiation; the second system conducts heat to each individual sphere and consists of small heaters attached to the fiberoptics bundle near the balloon. Thermostatic control is required for both systems.

1.3 Preliminary Design Performance Evaluation

A satellite (or space exposed component) in orbit around the earth is subjected to a natural thermal environment from three sources: (1) direct solar radiation, (2) earth thermal radiation, and (3) solar energy reflected from the earth (albedo). Direct solar radiation is obviously the most significant heat source. For a detailed thermal control analysis, the fraction of the energy radiated from the sources that actually impinge on the surfaces of consideration must be determined. The calculation of incident energy due to direct solar radiation is straightforward, since for practical purposes the light can be considered parallel. The prediction of the incident thermal radiation and albedo is complicated by the fact that the energy reaches the vehicle from multiple directions (particularly for low-altitude orbits), making the analysis sensitive to the geometry and orientation relative to the earth. Consequently, for analysis of earth thermal radiation and albedo, it is necessary to consider specific configurations in space. The variations in magnitude and direction of the three energy sources follow independent relationships and can, therefore, be treated separately. The total natural thermal environment is obtained by summing these sources.

The control of the radiant-energy exchange between the surfaces of interest and the space environment depends primarily on their solar absorptance (α) and infrared emittance (ϵ). It is apparent that the lower the α/ϵ ratio the lower the temperature and, in case of internal heat dissipation, the higher the ϵ, the lower the temperature. In general, the mean temperature is a function of the following parameters:

- Orbital mean impinging energy rates from the natural environment,

- Ratio of projected area to total area of sun-exposed surfaces

- α/ϵ ratio of sun-exposed surfaces

- Internal heat dissipation rate

- Total area of surfaces exposed to space

- Infrared emittance of surfaces exposed to space

Because of the orbital variation of incident heating rates, external-structure and equipment skin temperatures will experience significant excursions about the mean temperature level. Transient temperatures of the external skin, however, are of importance only as they influence internal temperatures. The establishment of structure and component temperature histories to further determine thermal-control requirements (coatings, insulation, orientation of components and radiation surfaces, etc.) requires extensive analysis. A digital general heat-transfer program (thermal analyzer), an orbital heat-flux program, and radiative-interchange factor programs will have to be utilized during the course of further studies.

For the purpose of this study, a brief analysis was performed by simplified methods. For the balloon array, the steady-state heat balance was calculated as follows:

$$Q_{in} = Q_{out}$$

$$\alpha S A_P = \epsilon \sigma A_T T^4$$

$$T^4 = \frac{S}{\sigma} \frac{\alpha}{\epsilon} \frac{A_P}{A_T}$$

Q = Heat flow by radiation, Btu/hr

α = Solar absorptance

S = Solar radiation, 442 Btu/hr-ft^2 near earth

A_p = Projected area, square feet

σ = Stefan-Boltzmann constant, 0.1714×10^{-8} Btu/ft^2 -hr- $°R^4$

ϵ = Infrared emittance

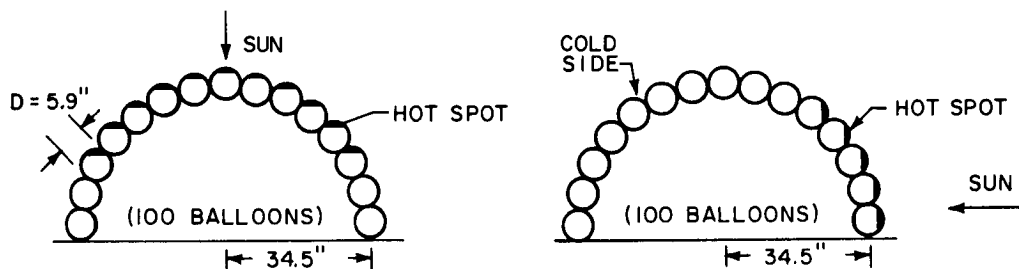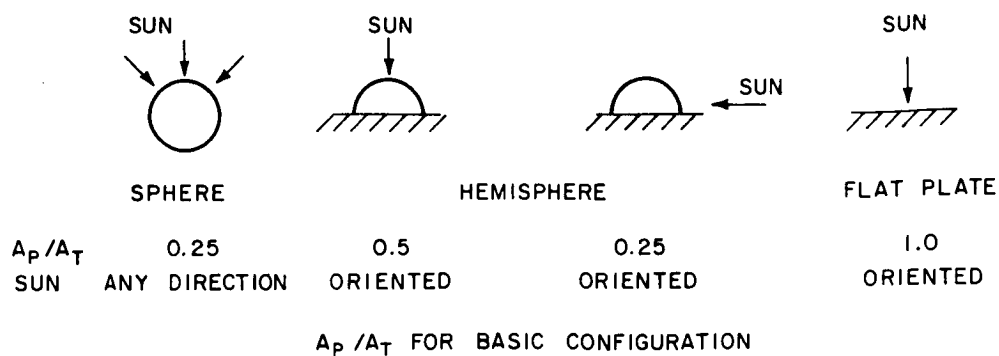A_T = Total area, square feet

T = Absolute temperature, $°R$

By the assumption that $a = 0.1$ and $\epsilon = 0.03$*, the steady-state temperature was calculated for a variety of A_p/A_T values. Results are shown in the following table and in Figures C-1 and C-2:

A_p/A_T	t(°F)	Comments
0	-460	S = 0, no solar radiation
0.10	+81	Solar radiation to a fraction of the total area (Projected area = 10 percent of total area)
0.25	+220	Solar radiation to sphere and hemisphere, perpendicular to main axis
0.50	+350	Solar radiation to hemisphere, parallel to main axis
1.00	+502	Solar radiation to flat plate, approximation for sphere cap.

For the case $A_p/A_T = 0$ (or S = 0), i.e., balloons in shade of the spacecraft or spacecraft in shade of the earth, the temperature tends to approach the absolute minimum of -460° F which is below the freezing temperature of any gas. Sun impingement at a small area of a balloon will raise its average temperature to an acceptable level; if, for example, the projected area is 10 percent of the total area and receives solar energy, the average temperature is up to +81° F.

The power requirement to maintain the thermal balance during shaded periods has been calculated assuming an average total area of 34 ft^2 (hemispherical, 34.5-inch radius array of 100 balloons). Results are presented in the table below.

---

*Data supplied by the Schjeldahl Co.

SUN

SUN

SUN

SUN

SPHERE

HEMISPHERE

FLAT PLATE

| A_P/A_T | 0.25 | 0.5 | 0.25 | 1.0 |
| SUN | ANY DIRECTION | ORIENTED | ORIENTED | ORIENTED |

A_P/A_T FOR BASIC CONFIGURATION

D = 5.9"

SUN

HOT SPOT

(100 BALLOONS)

|← 34.5" →|

COLD SIDE

HOT SPOT

SUN

(100 BALLOONS)

|← 34.5" →|

BALLOON ARRAY THERMAL CONSIDERATIONS
(SECTION VIEW)

ALBEDO

SUN

EARTH

ILLUMINATED BALLOON ARRAY

SHADED BALLOON ARRAY
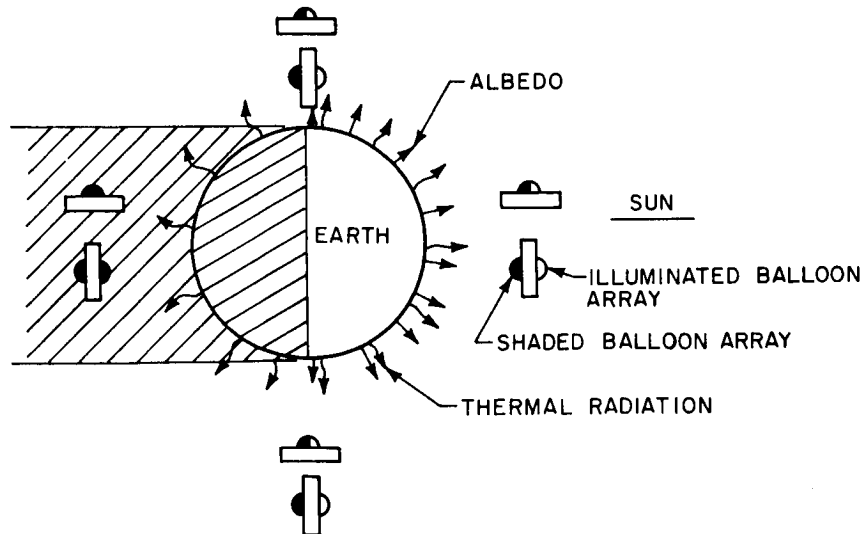
THERMAL RADIATION

ORBITAL CONSIDERATIONS FOR SELECTED BALLOON ARRAY

86-9679

Figure C-1 BASIC THERMAL ANALYSIS CONSIDERATIONS

-112-
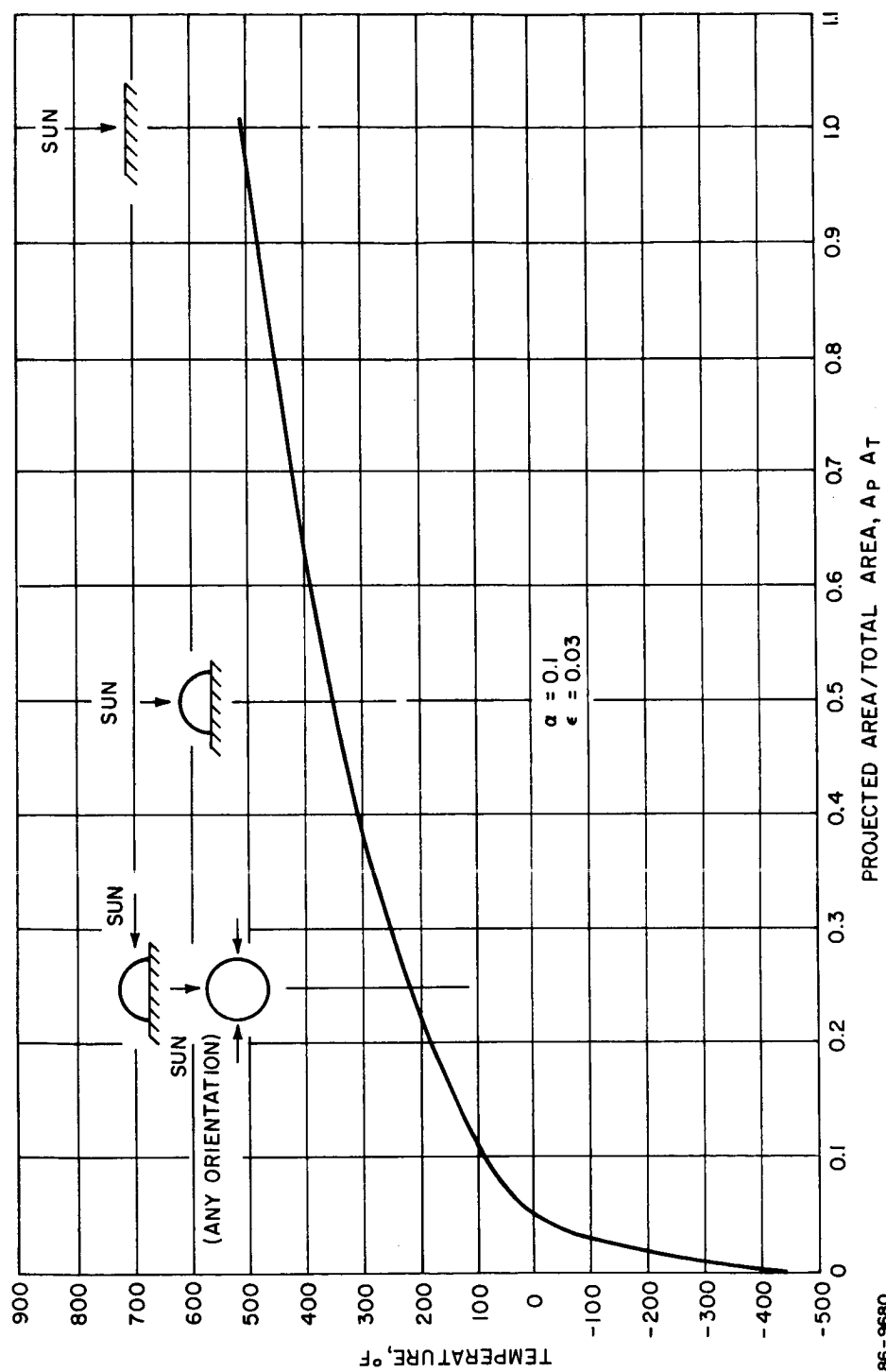
Figure C-2 BALLOON STEADY-STATE TEMPERATURE VERSUS RATE OF PROJECTED (SUN EXPOSED) AREA/TOTAL RADIATING AREA

86-9680

-113-

Balloon Temperature	Total Power Required	Power per Balloon
t (°F)	Watts	Watts/100
-100	17	0.017
-200	4.6	0.046
-300	0.7	0.007

It can be seen that only a very small amount of power (0.7 watt) is required to maintain the balloon temperature above the boiling point of argon (-185.7° C). The actual power requirement will be higher if heat losses and difficulties in the distribution of an equal amount of power to each balloon are considered. For xenon, the power required is 15 to 20 times larger than for argon.

1.4 Conclusions

It is concluded from this brief investigation that the temperatures anticipated as a result of extremes in incident heat fluxes may require provisions for thermal control. More detailed analyses, however, are required to verify the results of this preliminay investigation and to establish design parameters and guidelines in addition to the following:

a. Design towards an orbital mean-temperature level nearer the lower limit than the higher limit; components falling below the lower limit (failure mode) will normally recover, while temperatures above the higher limit can cause permanent damage.

b. Locate components sensitive to environment temperature fluctuations in modules of high thermal capacity. Provide low-ϵ coatings (except on surfaces designed for heat radiation) that are less prone to temperature fluctuations in a predominantly radiative thermal environment.

SUMMARY

A laboratory study has been performed to empirically demonstrate the feasibility of the proposed instrumentation concept in determining the composition of micro-meteoroids. This concept utilizes a space-deployed miniature spectrographic system to record the emission spectra resultant from particle heating in passage through a captive inert atmosphere. This gas is encapsulated in a series of balloon-like test cells whose thin-wall membranes permit penetration of the high-energy particles into the internal gas environment. The resultant radiation is relayed through plastic fiber optics bundles to a single miniature spectrograph where the terminal ends of the fibers form the entrance aperture to the dispersive optics. The spectral data are then stored for either astronaut retrieval or transmittal for earth-based analysis. This concept does not demand the recovery of any portion of the instrument package.

Feasibility proof necessitated dynamic simulation of meteors in order to develop and test a breadboard model of this system. Simulation was effected by hypervelocity launch of a number of both artificial and real meteoritic samples by a .22 caliber light gas gun. Argon and xenon were used as test cell gases.

Monochromator measurements using a photomultiplier readout in conjunction with spectrographic film record analysis indicate that no anomalous radiation effects occur in the argon or xenon atmosphere as a function of pressure or velocity within the limits investigated in this experiment. A strong velocity dependence of radiation occurs as expected by simple aerodynamic theory and by experience gained from similar radiation studies in air atmosphere. It does not seem feasible to extrapolate these data significantly beyond the limits tested in the laboratory because of the inherent fluctuation in the data and because of possible changes in the aerodynamic flow regimes represented by the actual meteoroid velocity conditions. Instead, such extrapolation must be based upon an appraisal of the best current theoretical model of the anticipated physical phenomenon.

In order that maximum sensitivity can be achieved for the proposed in situ measurement of meteoroid composition, a miniature spectrograph has been developed to provide an effective F/1.5 optical system. It has been concluded that the practical realization of such a fast spectrograph must of necessity involve an empirical approach to the design utilizing optimum available optical components. This spectrograph has been designed for use with either photographic film or a television-type vidicon sensor. The data obtained in this report were recorded on photographic film using the miniature spectrograph coupled by fiber optics to a prototype balloon for containing the captive atmosphere. Spectral data have been obtained on several simulated and actual meteoritic materials. Thorough analysis of these data shows excellent correlation with ground-based recording of actual meteor spectra.

It has been demonstrated that adequate resolution can be achieved together with sufficient exposure to provide spectral data which exceed the quality of meteor spectra obtained by earth-based photographic systems. These data are entirely adequate to define the composition of meteoroid materials and have been shown to be free from background radiation caused from impact with the balloon walls or from the excitation of the captive inert gas.

A preliminary conceptual engineering design has shown application of the scientific concept and instrument system to a typical satellite mission. Fundamental design parameters are delineated and further development suggested where required. The experiment is shown to be practical for exposure to a space environment.

REFERENCES

1. Millman, P., One Hundred Meteor Spectra, presented at the 81st meeting of the American Astronomical Society, Ottawa, (19-23 June 1949).

2. Millman, P., The Physics of Meteors, The Bulletin of the Canadian Association of Physicist, Vol. 12, No. 2, (Summer 1956).

3. Soberman, R. K., Micrometeorite Collection from a Recoverable Sounding Rocket, AFCRL 1049 (November 1961).

4. Hibben, R. D., Micrometeorite Data Challenges Theories, Aviation Week and Space Technology, (5 September 1966).

5. Wentink, T., J. C. Keck, J. C. Camm and B. Kivel, Radiation from Hot Air: Part II, Shock Tube Study of Absolute Intensities, Annals of Physics, Vol. 7, No. 1, (May 1959).

6. Dmitrieff-Kikline, A., Spectrographic Studies of the Radiation Emitted by Hypersonic Projectiles, CARDE Technical Note 1564 (May 1963).

7. Among others: Sawyer, R. A., Experimental Spectroscopy, Dover Publications (1963).
   Jenkins, F. A., and H. E. White, Fundamentals of Optics, McGraw Hill (1957).
   Fastie, W. G., A Small Plane Grating Monochromator, Journal of the Optical Society of America, Vol. 42, No. 9, (September 1952).
   Megill, L. R., and L. A. Droppleman, Study of the Effect of Large Aperture on the Performance of an Ebert Spectrometer, Journal of the Optical Society of America, Vol. 52, No. 3 (March 1962).
   Kudo, K., Optical Properties of Plane-Grating Monochromator, Journal of the Optical Society of America, Vol. 55, No. 2 (1965).
   Murty, M. V. K. R., Aspheric Ebert Monochromator for Simultaneous Observation of Many Wavelengths, Journal of the Optical Society of America, Vol. 52, No. 5 (1962).

8. Bass, A. M. and K. G. Kessler, Large Aperture Grating Spectrograph Utilizing Commercial Camera Components, Journal of the Optical Society of America, Vol. 49, No. 12 (December 1959).

9. The Construction and Calibration of a Bass-Kessler Grating Spectrograph, Memorandum RM-212, Research Department, Grumann Aircraft Engineering Corporation.

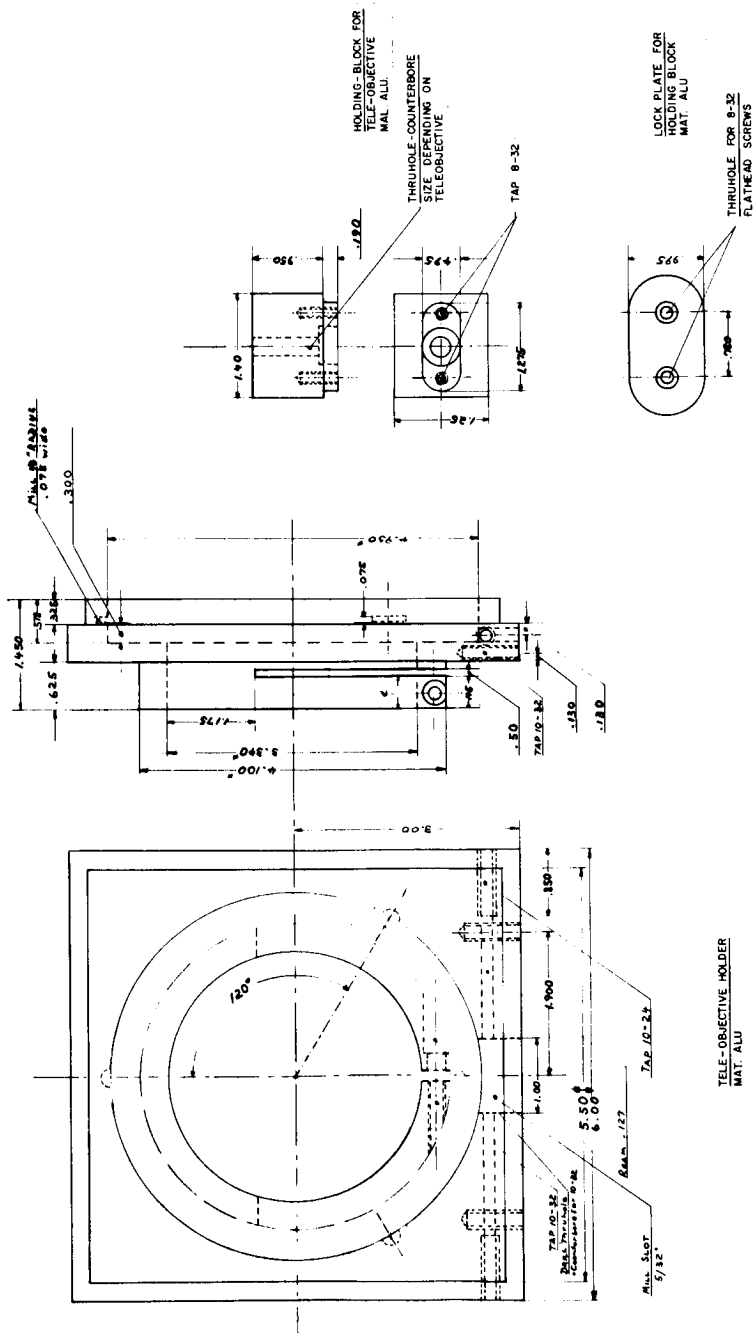10. Jenkins, F. A. and H. E. White, opus cited, p. 465.

11. Kodak Publication No. P-9, Kodak Photographic Films and Plates for Scientific and Technical Use.

12. Kodak Publication No. P-63 Two Papers on the Kodak Bimat Process.

13. Kodak Pamphlet No. P-65, An Introduction to the Kodak Bimat Processing System.

14. Lunar Orbiter: A Photographic Satellite, Journal of the SMPTE, Vol. 74, (September 1965).

15. (a) Nimbus: Model QTV-2 Advanced Vidicon Camera System, RCA Bulletin DEP/SCN-201-64.
    (b) Apollo: Lowrence, J. L., and P. M. Zucchino, Television Camera for the Command Module of the Command Module of the Apollo Spacecraft, Journal of the SMPTE, Vol. 74, (February 1965).
    (c) Ranger: Mesner, M. H. and A. J. Gravel, Camera System for Ranger, IEEE Transactions on Broadcasting (July 1965).
    (d) Tiros: RCA Bulletin No. DEP/SCN-205-64.

16. Johnson, R. E., Vidicon Performance Characteristics at Slow Scan Rates, RCA Publication No. ST-3066, reprinted from RCA Review, Vol. XXVII, No. 1 (March 1966).

17. Handbook of Chemistry and Physics, 31st Edition.

18. Schulz, L. G., The Optical Constants of Silver, Gold, Copper and Aluminum; I - The Absorption Coefficient, Journal of the Optical Society of America, Vol, 44, No. 5 (May 1954).

19. Johnson, Francis, S., The Solar Constant, Journal of Meteorology, Vol. II (December 1954).

20. Millman, P., A Complex Perseid Spectrum, Sky and Telescope, Vol. XV, No. 10, (August 1956).

21. Moore, Charlotte E., A Multiplet Table of Astrophysical Interest, National Bureau of Standards, Technical Note No. 36, (1959).

22. Wyckoff, C. W., and J. C. McCue, A Study to Determine the Optimum Design of a Photographic Film for the Lunar Surface Hand-Held Camera, Edgerton, Germeshausen and Greer Final Report No. B-3076, Contract No. NAS-9-3613, to NASA/MSC (1966).

23. Ibid.

24. Second Symposium on Protection Against Radiations in Space, NASA-SP-71, Published by NASA/STID (1965).

25. Brock, G. C., et al, Photographic Considerations for Aerospace, Itek Corporation (1965).

26. Kosofsky, L. J. and G. C. Broome, Lunar Orbiter: A Photographic Satellite, Journal of the SMPTE, Vol. 74, (September 1965).

27. Wood, J. A., Chapter 12, P. 348, Table 10 of the Moon Meteorites, and Meteors, (Middlehurst and Kuiper, Eds.) University of Chicago Press, (1963).

28. Corliss, C. H. and W. R. Bozman, Experimental Transition Probabilities for Spectral Lines of Seventy Elements, NBS Monograph 53, U. S. Government Printing Office (1962).

29. Meggers, W. F., C. H. Corliss and B. F. Scribner, Tables of Spectral Line Intensities, NBS Monograph 32, U. S. Government Printing Office 1961 (2 Vols.).

30. Naumann, Robert J., Pegasus Satellite Measurements of Meteoroid Penetration, (February 16 - July 20, 1965), NASA TM X-1192 (December 1965).

31. NOTE: This Figure was generated by Mr. H. Zook, NASA Houston. It represents unpublished data. It is used here by permission of the Contract Monitor.

32. Barrington, Alfred E., High Vacuum Engineering, Prentice Hall, Englewood Cliffs, N. J., (1963) P. 53.

33. Kennard, E. H., Kinetic Theory of Gases, McGraw Hill, (1938), p. 149.
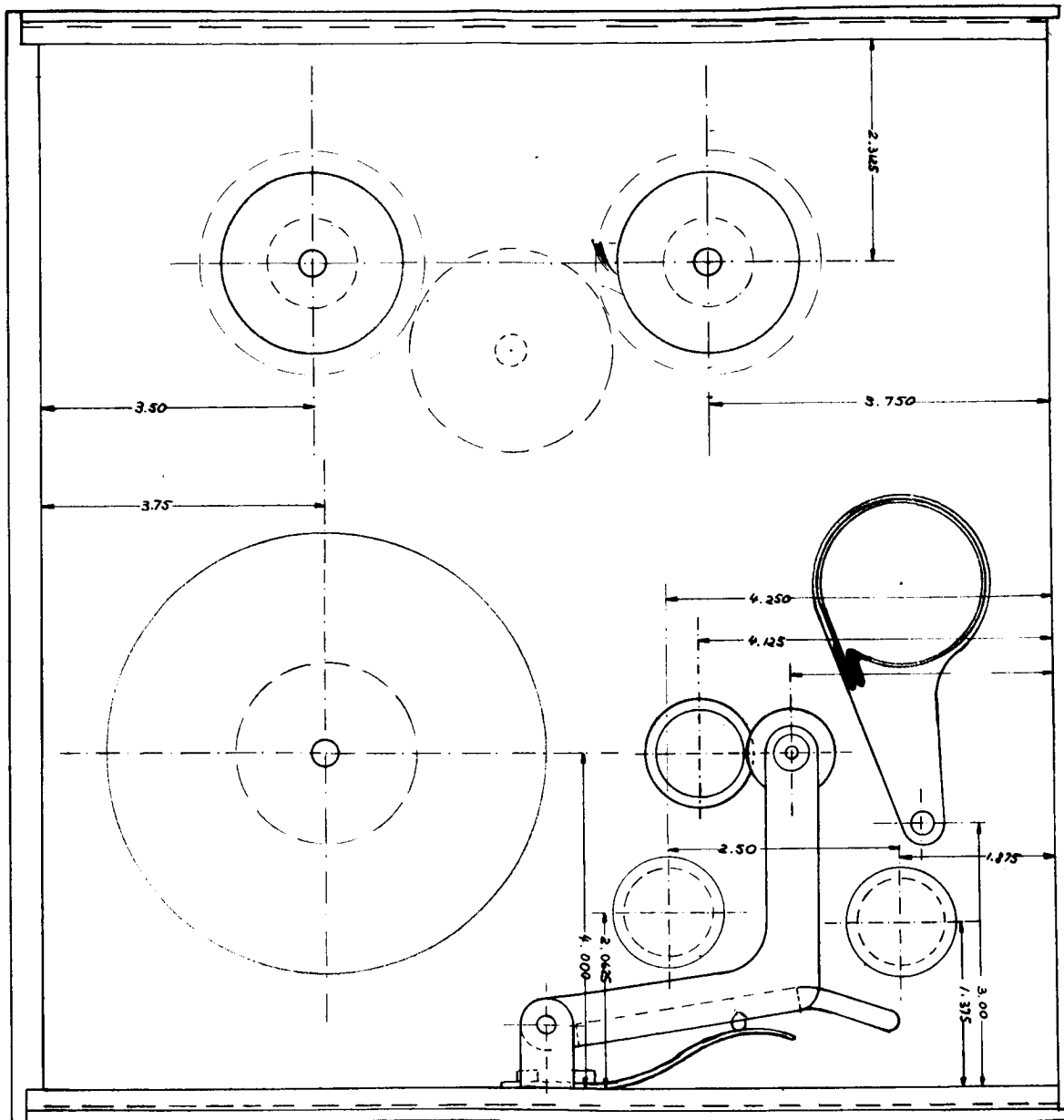
34. Ibid, p. 55.

DRILL AT TAP FOR 1/8" ADJUSTING PIN
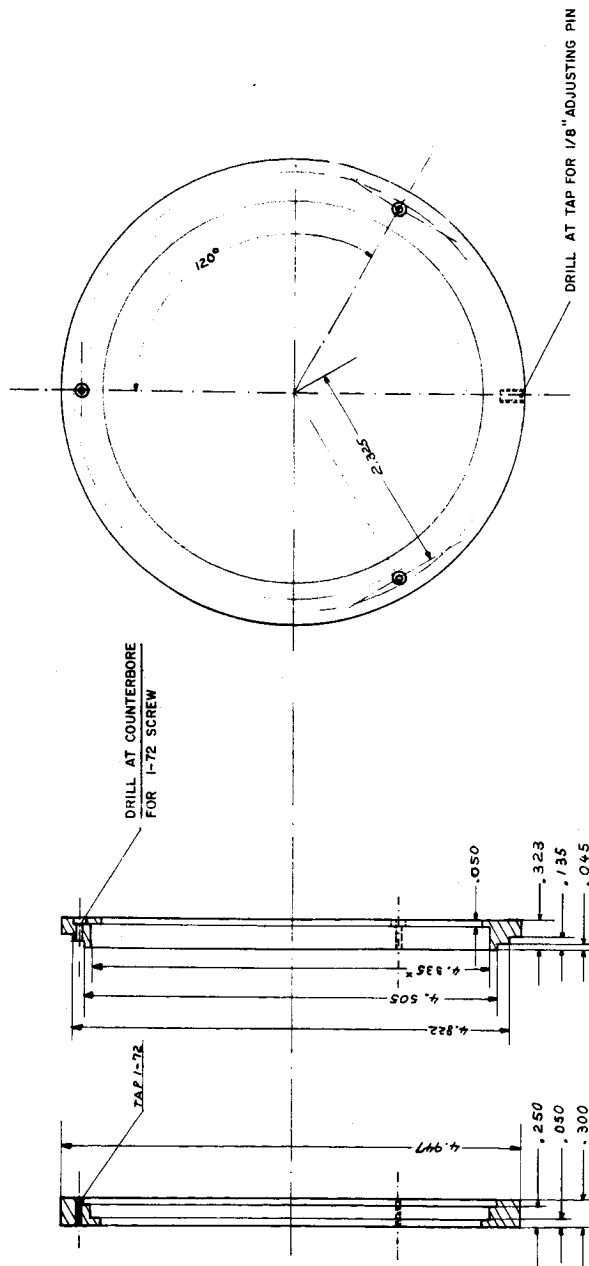
NOTICE: INSIDE DEM. X MAY CHANGE DEPENDING ON GRATING TOLERANCES

DRILL AT COUNTERBORE FOR 1-72 SCREW

TAP 1-72

120°

2.325

Pring No. 1a BREADBOARD SPECTROGRAPH: GRATING HOLDER (ALUMINUM)

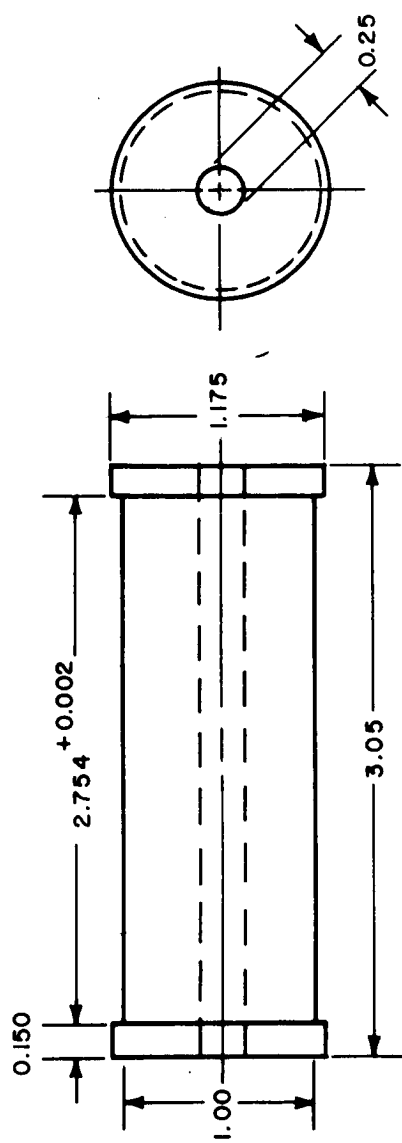Print No. 1b BREADBOARD SPECTROGRAPH: COLLIMATOR LENS HOLDER

HOLDING-BLOCK FOR TELE-OBJECTIVE MAL. ALU.

THRUHOLE-COUNTERBORE SIZE DEPENDING ON TELEOBJECTIVE

TAP 8-32

LOCK PLATE FOR HOLDING BLOCK MAT. ALU

THRUHOLE FOR 8-32 FLATHEAD SCREWS

TELE-OBJECTIVE HOLDER MAT. ALU

Print No. 1c BREADBOARD SPECTROGRAPH: BASEPLATE
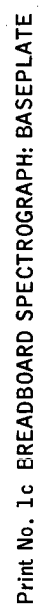
Print No. 2 BIMAT PROCESSOR: PROCESS CHAMBER FOR KODAK 35-MM AND
70-MM FILM
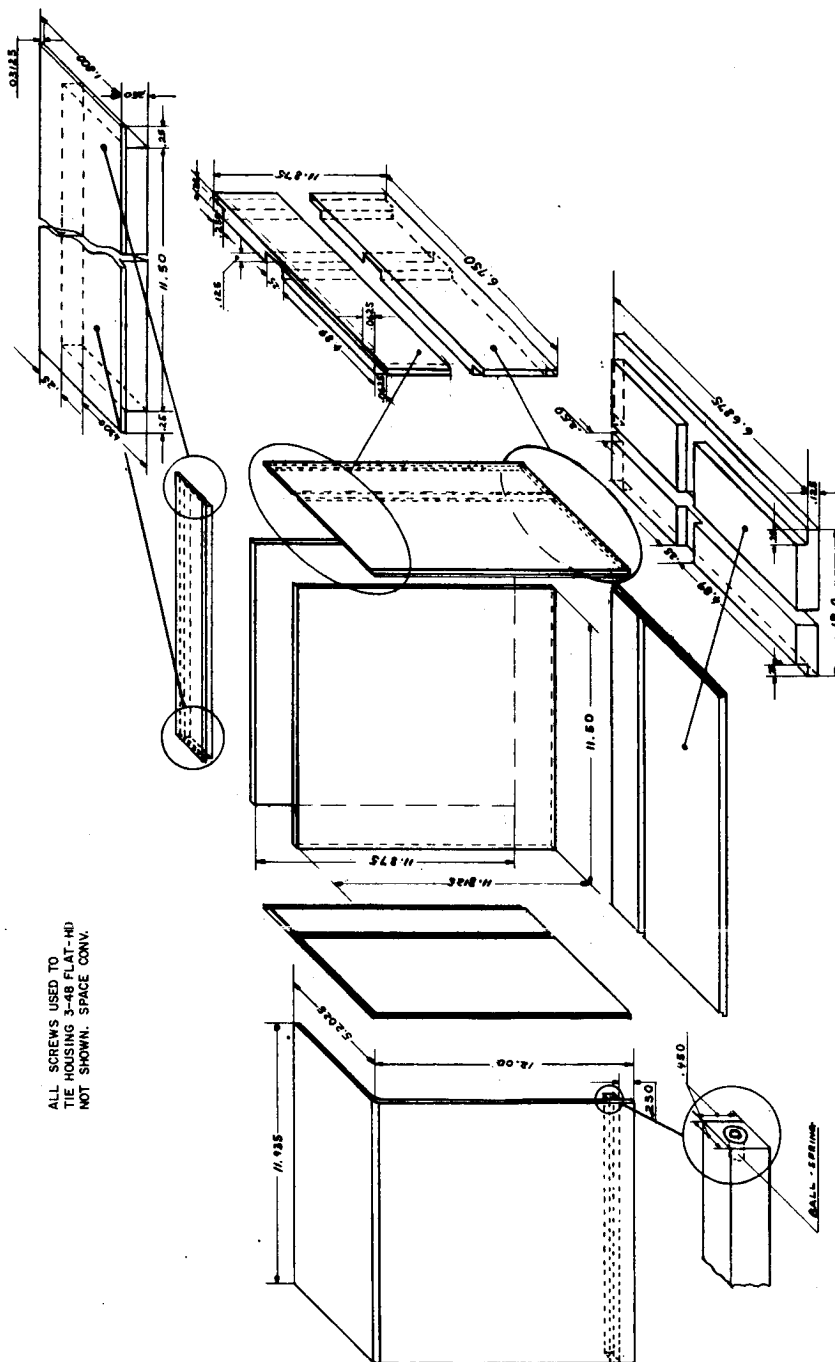
ALL SCREWS USED TO
TIE HOUSING 3-48 FLAT-HD
NOT SHOWN. SPACE CONV.

Print No. 3 BIMAT PROCESSOR: BIMAT HOUSING MATERIAL (ALUMINUM)
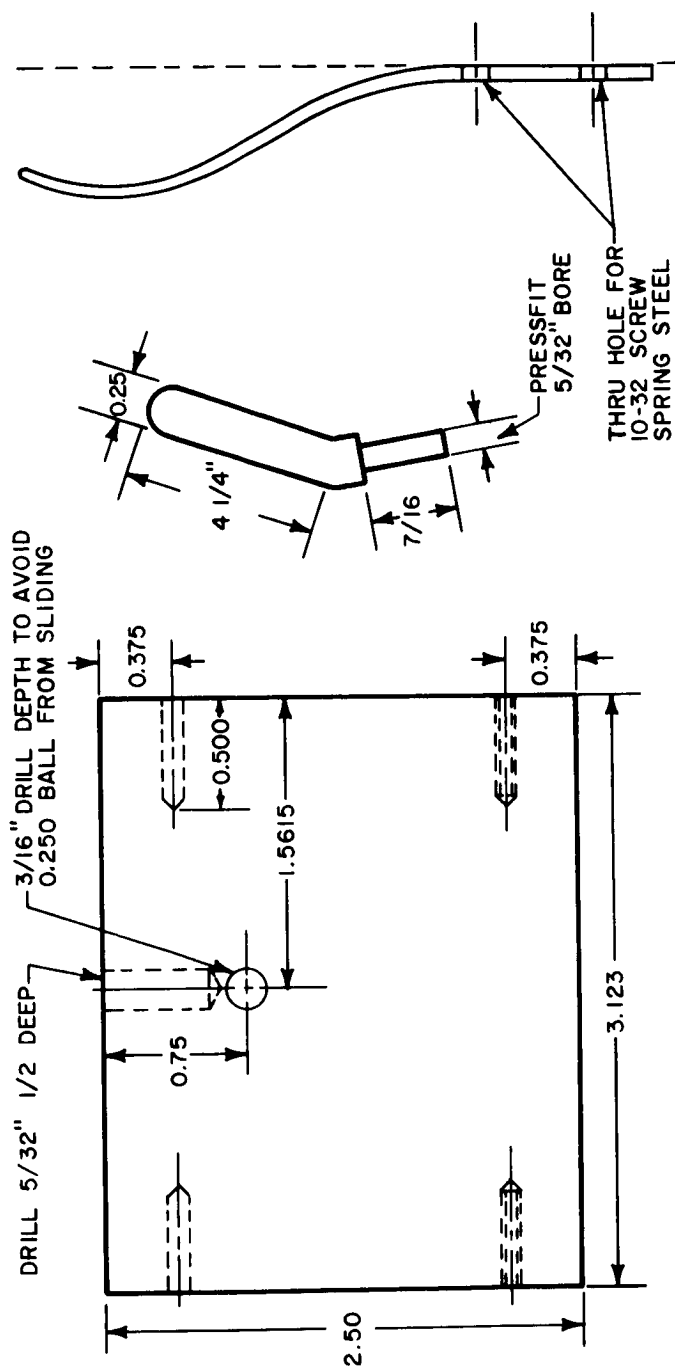
MATERIAL — NYLON

0.25

1.175

2.754 +0.002

3.05

0.150

1.00

0.25

1.175

1.377 +0.001

3.05

0.150

1.00
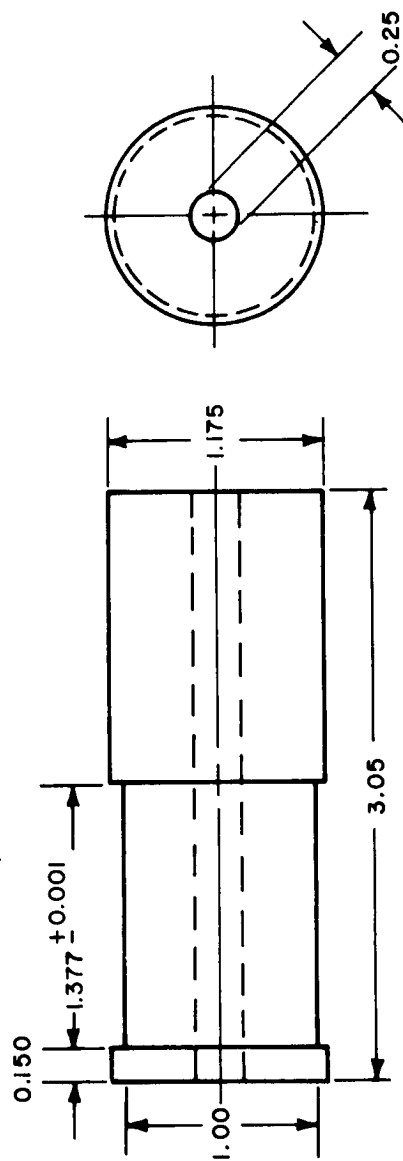
86-9444

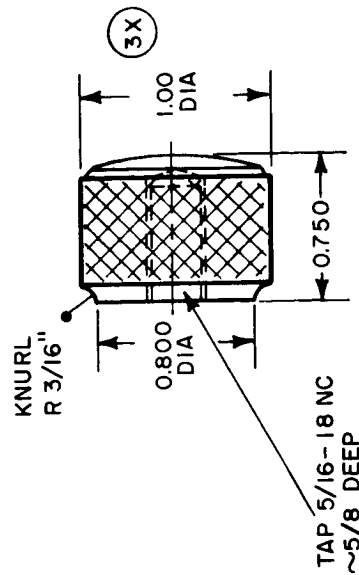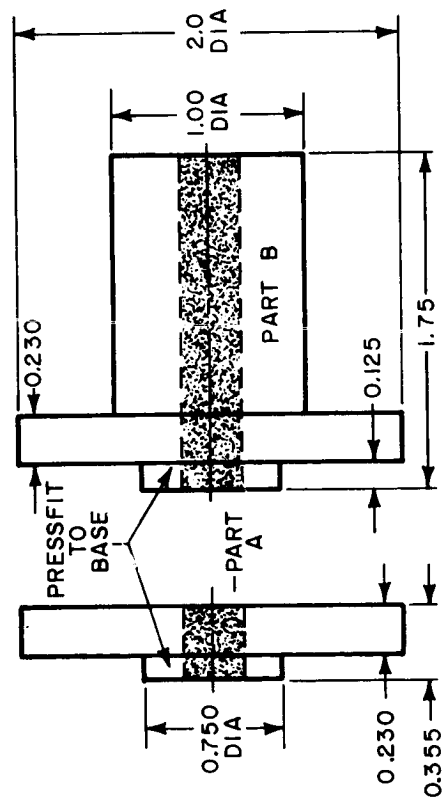Print No. 4 BIMAT PROCESSOR: LEAD-ROLLER-(TWO OF EACH PER UNIT)

-126-

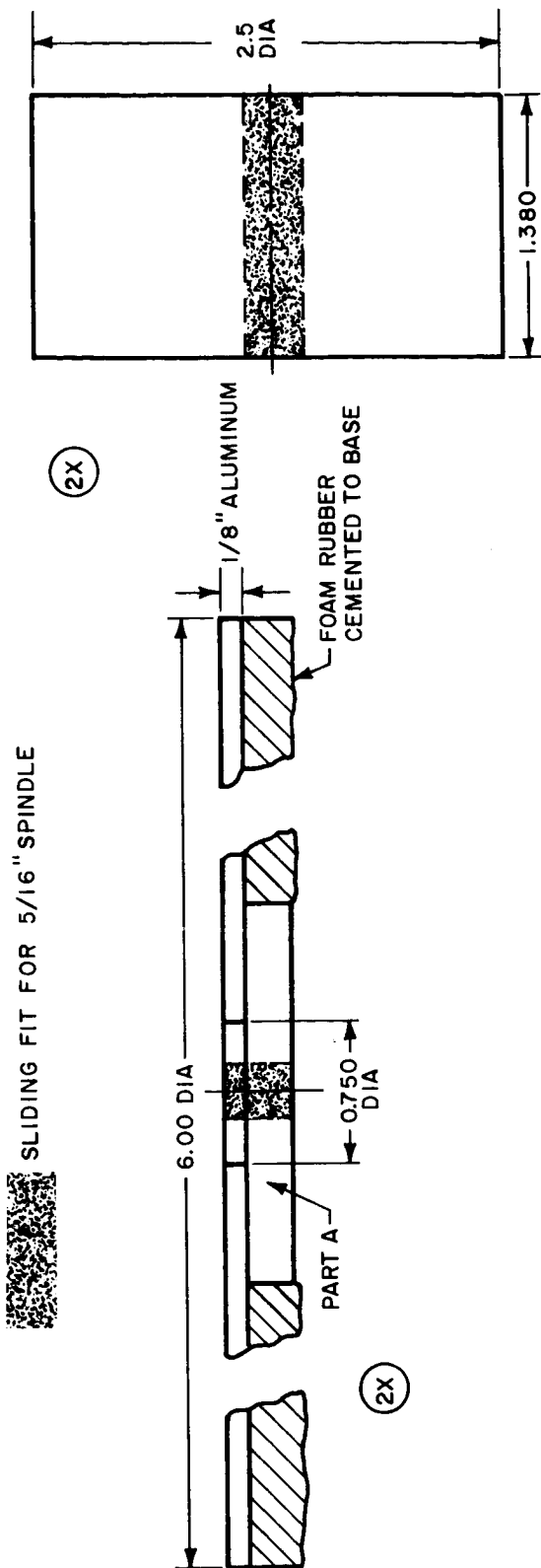BORE 0.375 inch
TO FIT BEARING

10 degrees

R=5/16 inch

2.750

R=9/16

2X

COUNTERBORE
FOR 4-40 CAPSCREW
TRANSFER FROM
PRESSURE PLATE

2.750

TAP 3-48

1/8 inch BORE

PRESSFIT 1/8 inch
STEEL PIN 1/2 inch LONG

0.625

MATERIAL: ALUMINUM
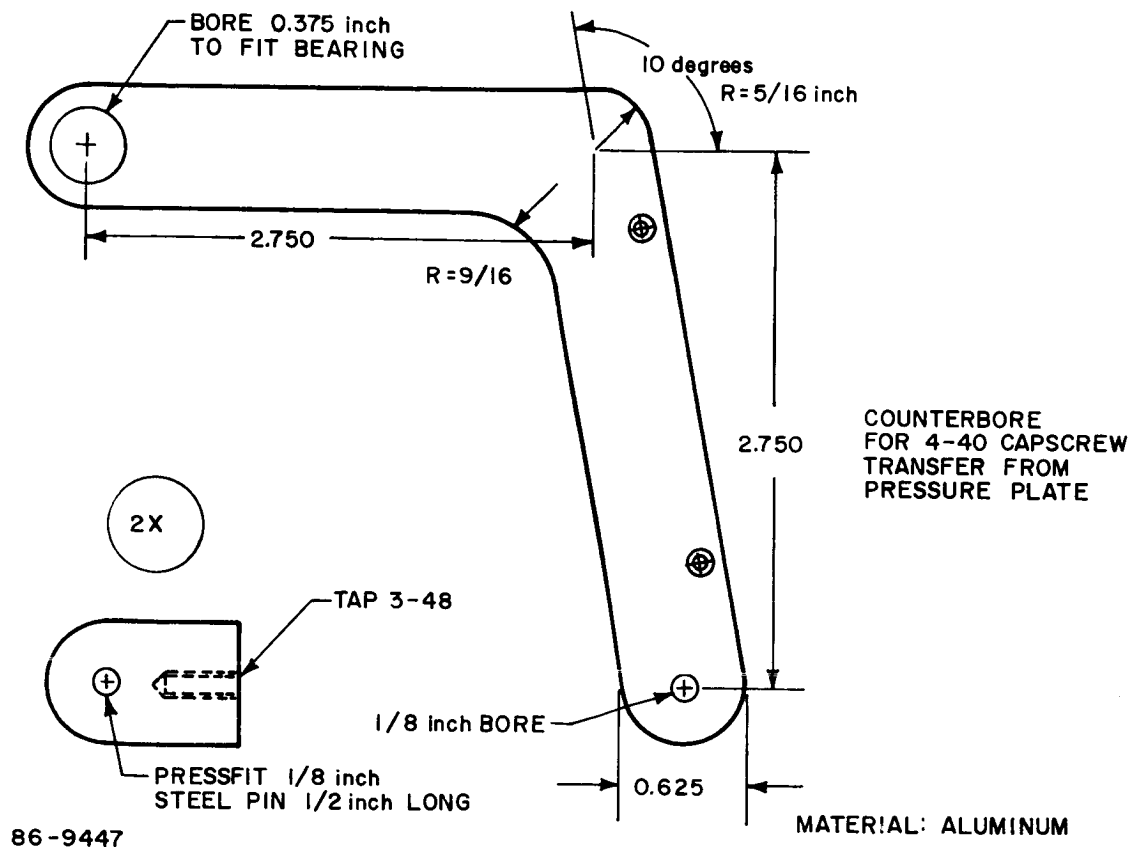
86-9447

Print No. 5 BIMAT PROCESSOR: PRESSURE ARMS (TWO PER UNIT)

DRILL 5/32" 1/2 DEEP

3/16" DRILL DEPTH TO AVOID
0.250 BALL FROM SLIDING

0.375

0.500

1.5615

0.75

0.375

3.123

2.50

0.25

4 1/4"

7/16

PRESSFIT
5/32" BORE

THRU HOLE FOR
10-32 SCREW
SPRING STEEL

1/4" STEEL

1/4" STEEL ROD

5/16"

8-32 3/8"LONG

86-9446

Print No. 6 BIMAT PROCESSOR: HANDLE, PRESSURE PLATE, SPRING

-128-

2.5 DIA

1.380

2x

1/8" ALUMINUM

FOAM RUBBER
CEMENTED TO BASE

SLIDING FIT FOR 5/16" SPINDLE

6.00 DIA

0.750 DIA

PART A

2x

3x

1.00 DIA

0.750

KNURL R 3/16"

0.800 DIA

TAP 5/16-18 NC
~5/8 DEEP
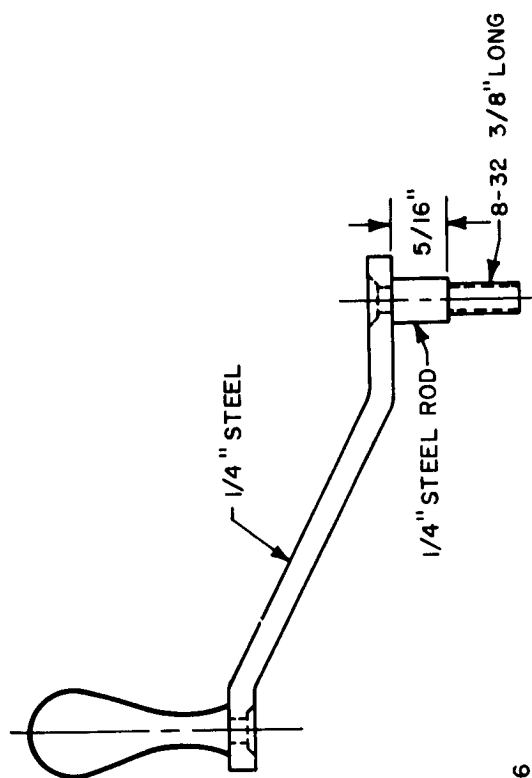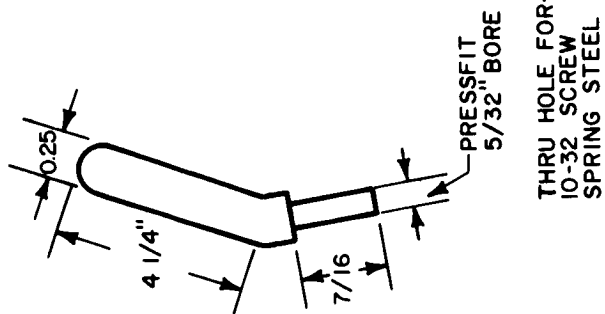
MATERIAL : ALUMINUM
FOAM RUBBER 1/4"

2.0 DIA

1.00 DIA

0.230

PART B

PRESSFIT
TO BASE

PART A

0.125

1.75

0.750 DIA

0.230

0.355

86-9447

Print No. 7 BIMAT PROCESSOR: BIMAT SUPPLY WHEEL, SPACER AND KNOBS
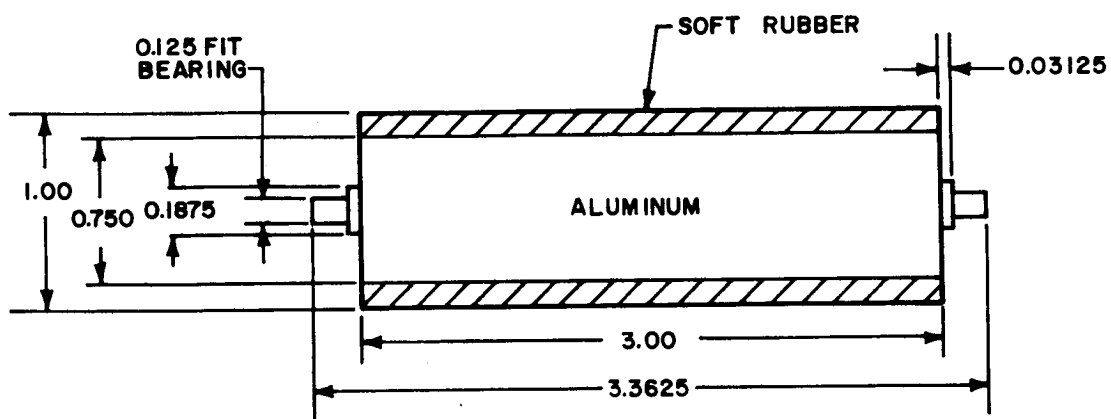
-129-

SLIDING FIT FOR 5/16" SPINDLE

3"

1.625

2X

3"

3"

1.656

2X

3"
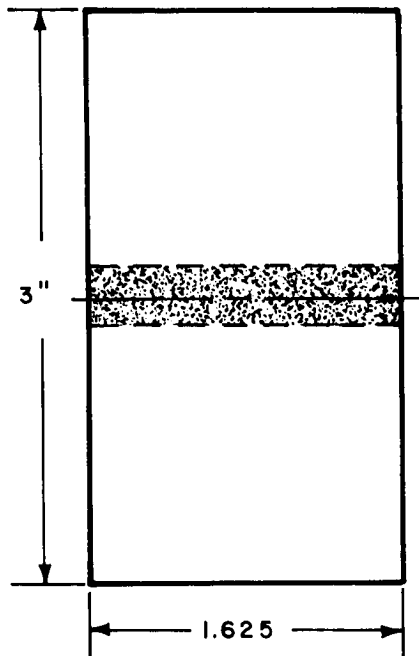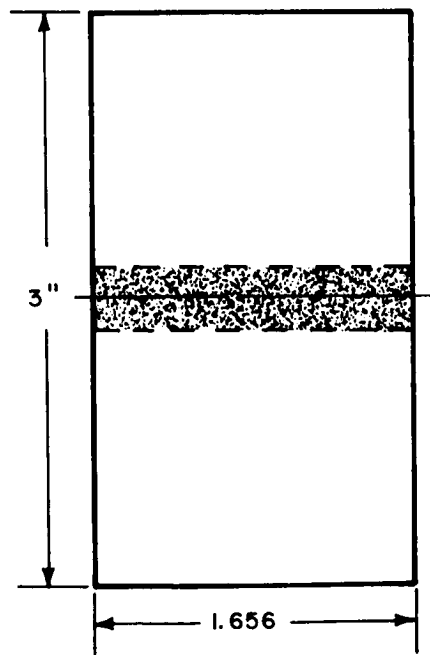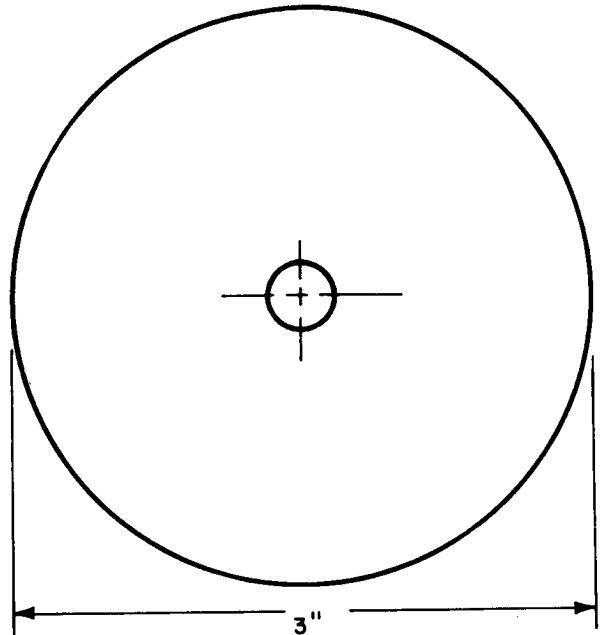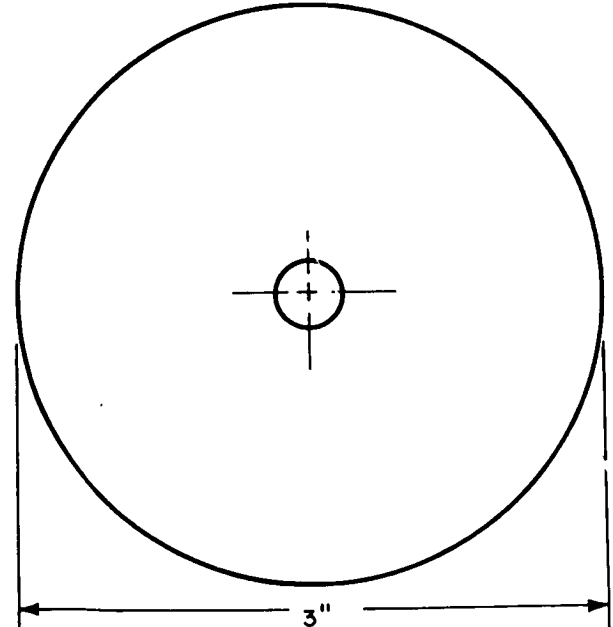
Print No. 8 BIMAT PROCESSOR: FILM AND BIMAT TAKEUP ROLLERS (TO GO ON TAKEUP SPINDLES),
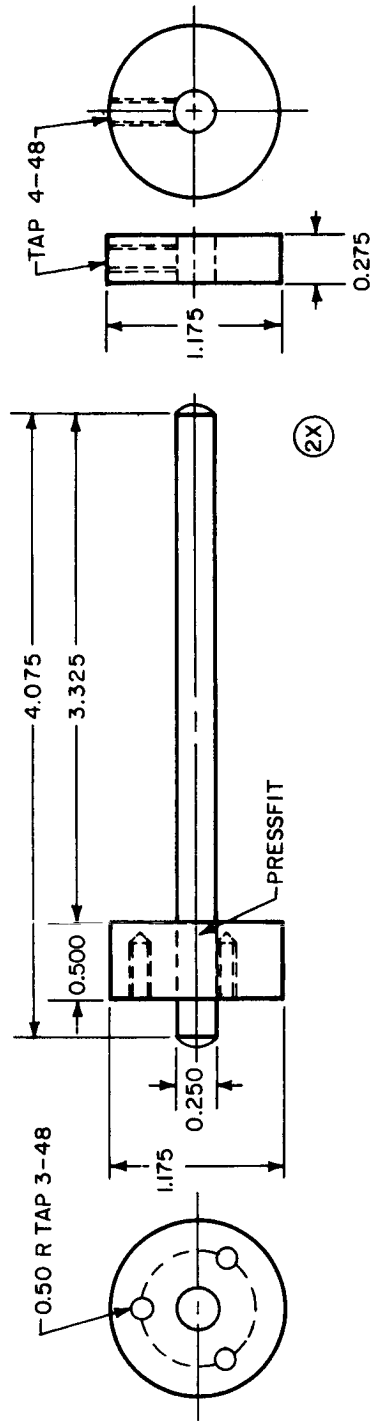MATERIAL: ALUMINUM

0.125 FIT BEARING

SOFT RUBBER

0.03125

1.00

0.750 0.1875

ALUMINUM

3.00

3.3625

86-9451

Print No. 9 BIMAT PROCESSOR: FILM FEED ROLLER

0.50 RADIUS
TAP 3-48

BEARING SIZE
0.500 O.D. 0.250 I.D

2.50

2.00

2.375

RETAINING
RING

0.625

3.0625

2.375

2.50

0.0625

1.00
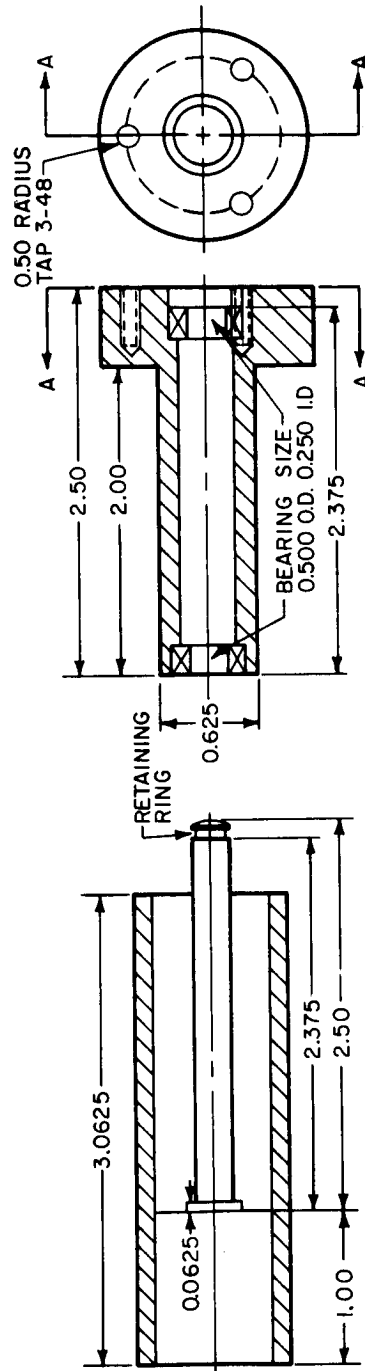
MATERIAL : BASE - ALUMINUM
ROLLER - STAINLESS STEEL

Print No. 10 BIMAT PROCESSOR: PRESSURE ROLLER

TAP 4-48

0.275

1.175

4.075

3.325

0.500

PRESSFIT

0.250

1.175

0.50 R TAP 3-48

(2X)

MATERIAL: DISTRIBUTOR RING –ALUMINUM
ROD – STAINLESS STEEL

Print No. 11 BIMAT PROCESSOR: FILM LEADING ROLLER SUPPORT

FELT
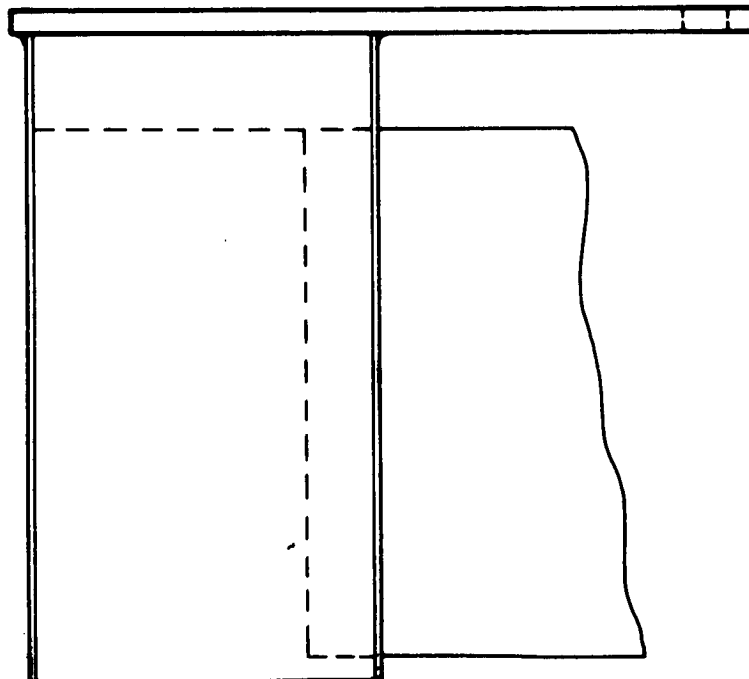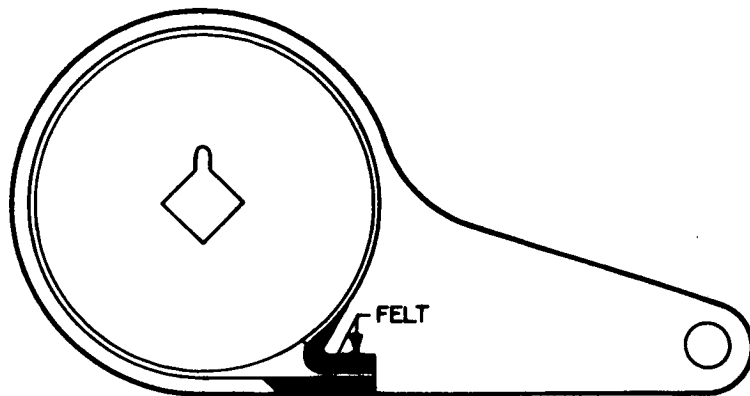
86-9452

Print No. 12 BIMAT PROCESSOR: MAGAZINE HOLDER FOR 35-MM AND 70 < MM FILM MATERIAL: ALUMINUM

DISTRIBUTION

Addressee	No. of Copies
NASA Manned Spacecraft Center 2101 Webster-Seabrook Road Houston, Texas 77058 Attn: Mr. Thomas Lee (+ 1 reproducible) Contract NAS 9-5267	5
NASA Manned Spacecraft Center Technical Information Dissemination Branch/BM6 Management Services Division 2101 Webster-Seabrook Road Houston, Texas 77058 Attn: Miss Retha Shirkey Contract NAS 9-5267	4
NASA Manned Spacecraft Center General Research Procurement Branch/BG721 2101 Webster-Seabrook Road Houston, Texas 77058 Attn: Miss Hilda J. Bolling Contract NAS 9-5267	1
Sandia Corporation Albuquerque, New Mexico Attn: H. E. Hansen, Div. 9311	1
Research Library - Wilmington (+ 1 reproducible)	3
Research Library - Lowell (+ 1 reproducible)	1
Reports Distribution Center - Wilmington	69